This is to certify that the

dissertation entitled

"Fluid Diffusion in Porous Silica"

presented by

Lowell I. McCann

has been accepted towards fulfillment
of the requirements for

Ph.D. degree in Physics

Bragg Golding
Major professor

Date February 10, 1998

FLUID DIFFUSION IN POROUS SILICA

By

Lowell I. McCann

A DISSERTATION

Submitted to
Michigan State University
in partial fulfillment of the requirements
for the degree of

DOCTOR OF PHILOSOPHY

Department of Physics and Astronomy

1998

ABSTRACT

FLUID DIFFUSION IN POROUS SILICA

By

Lowell I. McCann

Fluid motion in porous media has received a great deal of theoretical and experimental attention due to its importance in systems as diverse as ground water aquifers, catalytic processes, and size separation schemes. Often, the motion of interest is the random thermal motion of molecules in a fluid undergoing no net flow. This diffusive motion is particularly important when the size of the pores is nearly the same as the size of the molecules. In this study, fluid diffusion is measured in several varieties of porous silica whose pore structure is determined by the process by which it is made. The samples in this study have porosities (ϕ, the ratio of the pore volume to the total sample volume) that vary from 0.3 to 0.75 and average pore radii that range from approximately 15 to 120 Å.

Determining the effect of the pore structure on the diffusion of a liquid in a porous material is complicated by the chemical interactions between the diffusing molecules and the pore surface. In this study, ions in a hydrophilic fluid are used to block the adsorption of the diffusing dye molecules to the hydroxyl groups covering the silica surface. This technique is unlike typical surface treatments of silica in that it does not permanently alter the pore geometry.

In this work, fluid diffusion is measured with a transient holographic grating technique where interfering laser beams create a periodic refractive index modulation in

the fluid. The diffraction of a third laser off this grating is monitored to determine how quickly the grating relaxes, thereby determining the diffusion coefficient of the molecules in the fluid. Varying the grating periodicity controls the length scale of the diffusion measurement from 1.2 to 100 μm which is much larger than the average pore sizes of the samples. Therefore, over these large scales, we measure "normal" diffusion, where the mean squared displacement of a diffusing particle varies linearly with time.

In one particular type of porous silica, manufactured to create a narrow distribution of pore sizes in each sample, the normalized diffusion coefficient depends upon ϕ as $D/D_o \sim (\phi - \phi_c)^{1.5}$, as ϕ approaches a critical porosity ϕ_c. Here, D_o and D are the diffusion coefficients of the free fluid and the fluid within the porous sample, respectively. This result is compared with predictions of diffusion on a percolating cluster of identical pores as well as with continuum models based on networks with a distribution of pore sizes. While diffusion in these materials might be expected to behave according to a continuum model of porous networks based on the aggregation of spherical particles (the "Swiss-cheese" model), the behavior seen agrees with the prediction for networks whose smallest bonds have a non-singular distribution of conductances. This experiment is unique in that the materials chosen appear to produce a system that is close enough to the percolation threshold to allow a measurement of the percolation exponents. The diffusion coefficient in these samples is also shown to depend on the average pore radius as $D/D_o \sim (R_p - R_c)^{0.49}$, a result which, while unpredicted, is shown to be consistent with a previous study of fluid diffusion in silica.

To my parents.

ACKNOWLEDGMENTS

I would like to thank my advisor, Brage Golding, for the many engaging discussions about this research and for providing the opportunity to carry it out.

I also wish to thank Mike Dubson for all his help with my "other" thesis project, and for sharing with me his boundless enthusiasm for Physics.

I thank my guidance committee members: Norman Birge, Tom Kaplan, Brad Sherrill, and Dan Stump for their efforts to make sure I got it right.

The "shop guys": Tom Palazzolo, Jim Muns, and Tom Hudson all have my gratitude for their frequent help in the design and construction of a number of items over the years. Baokang Bi and Reza Loloee have also been of great assistance on many occasions.

I thank my fellow labmates: Jeeseong Hwang, Mike Jaeger, George Jeffers, Jung-Uk Kim, Evstatin Krastev, Wenhao Wu, Ashraf Yussouff, Qifu Zhu, and particularly Amy Bylsma Engebretson who deserves credit for my sanity after all these years in the basement.

I have also benefited from my interactions with a number of faculty members through the years: Bill Pratt, Phil Duxbury, Peter Schroeder, Carl Foiles, S.D. Mahanti, and Jerry Cowen.

I am grateful to the succession of Julie Stone, Mary Curtis, and Sandy Teague in Physics Stores for their help and pleasantness, even when I asked for something to be rushed.

Finally, a special thank you to Stephanie Holland for taking on the MSU bureaucracy a number of times to fix problems that she never caused, but always solved.

TABLE OF CONTENTS

LIST OF TABLES

LIST OF FIGURES

Chapter 1

INTRODUCTION

Porous materials could be defined as substances that "aren't all there." A solid material is porous if it contains voids which are free of the solid phase and are interconnected to provide a transport path through the material for a liquid or gas. By this definition, most materials found in nature are porous and only a few materials like metals, most crystals, and some plastics are nonporous. Most other solids, including rocks, wood, soil, human skin, bones, and sponges are porous to some degree. The first, and still most common use of porous media is as a filter to prevent objects larger than the pores from being passed.

Porous materials play an important role in many fields and technologies. Among these are oil recovery, groundwater motion, microbial transport, chromatography, and catalysis. In chromatography, flows through porous gels or packings of porous particles are used to separate molecules based on their size. The large surface area of porous materials makes them very useful for chemical reactions which require the catalytic action of a surface. The speed with which reactants are brought into contact with the surface and the products removed determines the overall efficiency of the process. Descriptions of these varied processes require an understanding of the motion of fluids within the narrow passages of the pores. The fluid may flow by the pull of gravity or an external pressure difference, but in small pores, the transport of fluids is dominated by diffusion caused by the random thermal motions of the molecules. It is this motion which is the focus of the present work.

In this study, the diffusion of a large number of probe molecules in porous silicas is examined over length scales which are much larger than the sizes of the pores. Diffusion on these macroscopic scales is different from diffusion on the scale of the pore size and is affected by the average properties of the pore network. The main focus of this work are materials created with a sol-gel process so that the average pore radius and the porosity (the ratio of the pore volume to the total sample volume) are varied from sample to sample in a controlled manner. In disordered porous media like rocks or sintered bead packs, there is a wide distribution of pore sizes. These sol-gel glasses, however, are prepared to have relatively narrow pore size distributions. This distribution of pore sizes, in combination with the finite size of the diffusing molecules, causes the system to approach the percolation threshold as the porosity and the average pore size are reduced. Comparing our experimental results to continuum percolation models that account for pore size distributions, we show that the diffusion is unlike that expected for porous media made from the aggregation of spherical particles ("Swiss-cheese" models), where the distribution of the conductances of the smallest pores contains a singularity as the pores decrease in size. This leads us to believe that the pore structure of the sol-gel glass is unlike that of these spherical particle models.

Another issue addressed in this work is the effect of chemical interactions between the diffusing molecules and the surfaces of the pores. If the interaction is strong, the diffusive behavior of the molecules in the pores is not simply a result of the pore structure. A number of techniques have been used in previous experiments to block the adsorption of the diffusing molecules to the pore walls, but those techniques alter the pore

structure by effectively decreasing the pore size and even blocking off sections of the pore network. In this work a different technique is employed that uses mobile ions attracted to charge sites on the surface to block the adsorption.

The rest of this document is organized as follows. Chapter 2 introduces the topic of diffusion and discusses several theoretical models describing diffusion in porous media. Among the models investigated are percolation models of both discrete and continuum networks. This chapter also contains a review of past fluid diffusion experiments within porous silicas. The holographic technique used to measure diffusion in this work is described in Chapter 3 along with specific details regarding the equipment and the measurements. Methods for characterizing porous materials are presented in Chapter 4, along with the results of such measurements on the materials used in this work. In addition, this chapter describes the structure and surface chemistry of the porous silica samples as well as how that surface interacts with the fluid and the probe molecules that are placed in the pores. Chapter 5 discusses the results of diffusion measurements in specially prepared sol-gel grown glasses and compares the results to the different models of diffusion in porous media. The results of diffusion measurements in other porous silicas made with different processes are shown in Chapter 6 and are compared to the sol-gel glasses. Finally, Chapter 7 summarizes the results of this study and lists potential extensions of the research in the future.

Chapter 2

BACKGROUND

I. Introduction

Much of the interest in the flow of liquids in porous materials began with experiments by H. Darcy in 1856 who studied the flow rate in a column of porous material under the influence of external pressure and gravity.[1] This rate was found to depend upon the viscosity of the liquid and the permeability of the material. Later, many workers tackled the problem of relating the permeability to the physical properties of a material by modeling the structure of its pores.[2] However, this type of forced motion is not the only transport that occurs in fluids. Even for small (or nonexistent) pressure differentials, fluids still move about due to the random thermal motion of the individual molecules. This diffusive motion is responsible for the transport of liquids in small structures where the pressure difference from one side to the other is extremely small. Even in fluids at rest, diffusion produces transport through a liquid.

II. Diffusion and Brownian motion

Diffusive motion in fluids and solids has been widely studied[3] since the discovery of brownian motion[4] and its later description with kinetic theory.[5] In an isotropic system, a single diffusing particle (or walker, if the particle is viewed in the context of a random walk), released at time zero from the origin, will move such that the mean squared displacement from the origin increases linearly with time. This relationship is easily derived beginning with Fick's First Law of Diffusion describing the flux of particles in a concentration gradient:[6]

(2.1) $\vec{J} = -D\nabla c(\vec{r},t)$

where $\vec{J}$ is the particle flux through one cm^2 in one second, D is the diffusion coefficient in cm^2/s, and $c(\vec{r},t)$ is the number of particles in one cm^3 at position $\vec{r}$ and time t. Combining this with the equation of continuity:

(2.2) $$\frac{dc}{dt} = -\nabla \bullet \vec{J},$$

we find:

(2.3) $$\frac{dc}{dt} = D\nabla^2 c(\vec{r},t),$$

assuming that D is not a function of position (or a function of the particle concentration). Solving this diffusion equation in one dimension by separation of variables, we find the general solution to be:

(2.4) $$c(x,t) = \int_{-\infty}^{\infty} C(\gamma)\exp(-\gamma^2 Dt)\exp(i\gamma x)d\gamma,$$

where $C(\gamma)$ is the Fourier transform of the initial concentration c(x,0). If we take c(x,0) to be a delta function to describe a particle released from position x' at time zero, then

(2.5) $C(\gamma) = (1/2\pi)$

This produces the one dimensional probability distribution for finding a single diffusing particle at position x and time t that was released from x = 0 at t = 0:

(2.6) $$c(x,t) = \frac{1}{2\sqrt{\pi Dt}} e^{-x^2/4Dt}.$$

With this distribution, we can determine the mean squared displacement (MSD) traveled by the diffusing particle in a time t. Because motion in all directions is equally

probable, the mean displacement (the first moment of the distribution) is zero, so the MSD is the best measure of the distance traveled by the particle. Therefore, the MSD in one dimension is:

$$(2.7) \quad \langle x^2 \rangle = \int_{-\infty}^{\infty} x^2 c(x,t)dx = 2Dt\,.$$

In three dimensions,

$$(2.8) \quad \langle r^2 \rangle = 6Dt.$$

This result shows that classical diffusive behavior (i.e. Fickian diffusion) is characterized by a MSD that is linear in time. It should be noted that in certain situations[7] the random motion of a molecule may not obey Fick's Law. This so-called anomalous diffusion is characterized by $\langle r^2 \rangle \sim t^{\delta}$ where $\delta < 1$ for "subdiffusion" and $\delta > 1$ for "superdiffusion". This can occur in situations such as the short-time motion on the percolating cluster of a network of bonds[8] or in fluids undergoing turbulent mixing.[9]

The solid phase of a porous material restricts the motion of molecules in a fluid and causes a reduction in the effective diffusion coefficient from that found in the free fluid. This effective diffusion coefficient accounts for the boundary conditions imposed on the random walking particle by the pore walls. This effect is seen by imagining the motion of a random walking molecule that starts its walk inside a pore (Figure 2.1). Initially, it moves about free from interactions with the pore walls and will appear to diffuse at the same rate as if it were in the bulk fluid. This changes once the walker begins to interact with the pore walls. If the pore is isolated (i.e. there is no outlet from the pore), the particle can never leave and therefore the measured effective diffusion coefficient must drop to zero as time increases. If the pore is not isolated, the particle

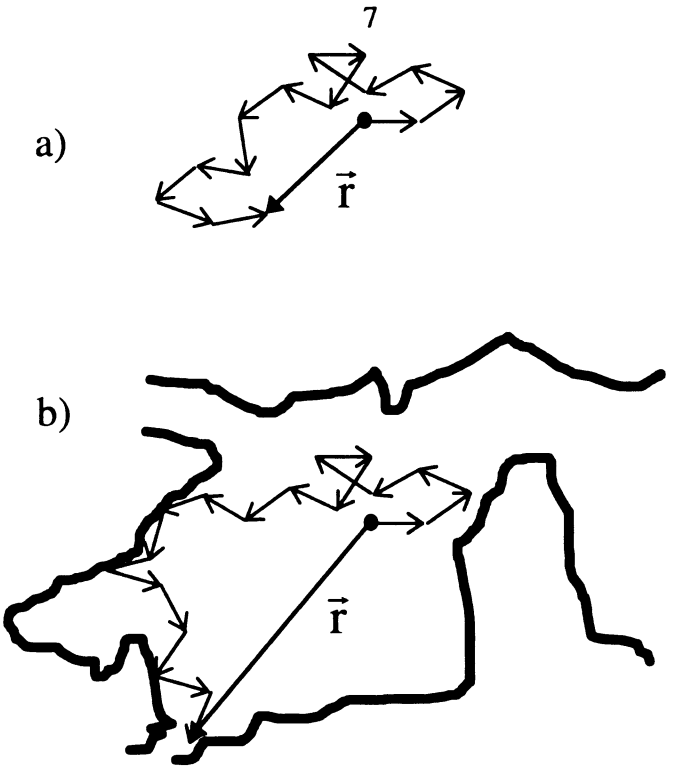

Figure 2.1: Schematic path of a random walker in (a) an unbounded fluid and (b) in a fluid within a pore.

will eventually find its way through an opening and into another pore. In this case, the particle will continue to diffuse through the porous material, but at a slower rate than it would in the free fluid.

These situations are illustrated in Figure 2.2 where the MSD of a particle is plotted as a function of time for several different environments. At short times the MSD increases linearly in time with a slope proportional to D_o, the diffusion coefficient for a molecule in the unconstrained liquid. For longer times, the behavior depends upon the particle's environment. The dashed line illustrates diffusion in a single isolated pore, where the MSD approaches a constant value related to the size of the pore. The slope in

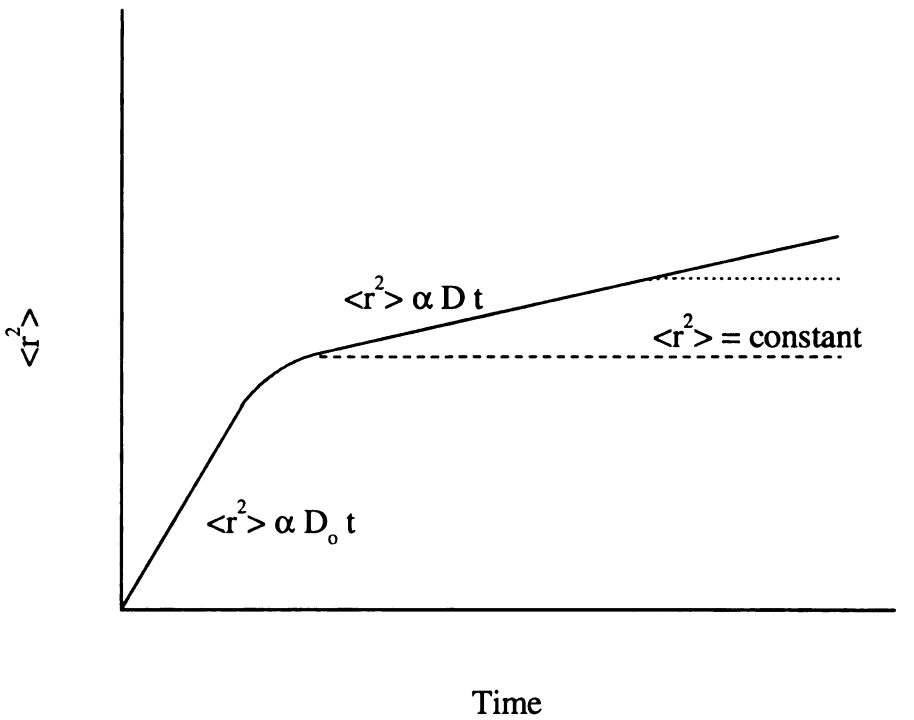

Figure 2.2: The mean squared displacement (MSD) of a random walker over time in three environments. Solid line: in an infinite cluster of pores, dotted line: in a finite size cluster containing many pores, dashed line: in an isolated pore.

this region is zero and there is no diffusive motion. The solid line shows the behavior in pores that are well connected to each other and diffusion is allowed, but at a slower rate than in the free fluid ($D < D_o$). The dotted line shows an intermediate case where the particle is in a cluster of pores that is isolated from the rest of the porous network. Here, the first two linear regions correspond to intrapore and interpore diffusion, respectively,

and the level of the constant region indicates the size of the cluster the particle is trapped in.

These simple pictures demonstrate that the measured value of the diffusion coefficient depends crucially on the environment where diffusion is occurring and the time scale over which it is measured. For most technologically important situations (groundwater motion and chromatography, for example) the diffusive motion of interest occurs over distances large compared to the pores in the system. Therefore, the long-time diffusion coefficient is of most interest in these situations.

Finally, it is important to note that the geometry of the porous media is not the only characteristic that affects the diffusive motion of a fluid. As mentioned earlier, porous materials are used in catalysis due to their large surface areas and the chemical properties of the pore walls. Any chemical interaction between the walls and the fluid will modify the molecular motion through the pores. Separating the geometric effects of the pore sizes and shapes from the chemical effects of the surface is crucial for any comparison to a model of the transport processes.

III. Theoretical models of diffusion in porous media

III a. Bundled tube model

There are two common and distinct methods for modeling porous materials: bundled tube models and network models.[10] In bundled tube models, the porous medium is viewed as a collection of nonintersecting capillary tubes whose diameter does not vary along the length of each tube though it may differ from tube to tube. Hydrodynamic models are a subset of these models and are concerned with the propagation of solute

molecules through channels of nearly the same size as the molecules,[11] but with lengths much larger than the diameter. The models are based on the assumption that the solute molecule of interest is several times larger than the solvent molecules that surround it. In this regime ($r_p >\sim r_H >> r_{solvent}$, where r_p is the radius of the channel, r_H is the radius of the solute molecule, and $r_{solvent}$ is the radius of the solvent molecule), the force on a single solute molecule may be described by the hydrodynamic drag of the solvent on a similarly shaped particle. For a spherical particle in an unconstrained fluid, this leads to an expression for the diffusion coefficient given by the Stokes-Einstein equation:

(2.9) $D_{SE} = k_B T/(6\pi\eta r_H)$,

where k_B is the Boltzmann constant, T is the temperature, η is the solvent viscosity, r_H is the effective solute radius (sometimes called the hydrodynamic radius), and D_{SE} is the diffusion coefficient in a dilute solution. Placing the solute in a narrow pore (Figure 2.3), the ratio of D, the diffusion coefficient in the confined fluid, to D_{SE} may be calculated over portions of the range $0 < r_H/r_p < 1$ by considering the forces on the solute as the

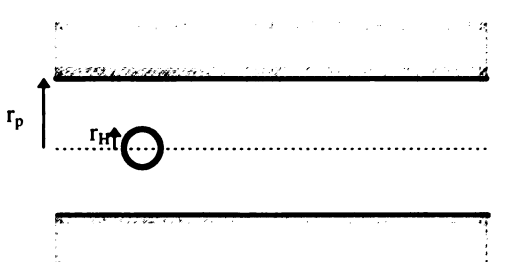

Figure 2.3: The tube geometry used in bundled tube models of porous media. r_p is the pore radius and r_H is the hydrodynamic radius of the solute molecule. The solute molecule is constrained to move along the tube axis in this picture.

solvent passes down the channel with a given velocity. The diffusive motion is recovered by setting the solvent velocity to zero once the solution is found.

The most commonly used solution is that of the Renkin equation:

$$(2.10)\quad \frac{D}{D_{SE}} = \left(1-\frac{r_H}{r_p}\right)^2\left(1-2.1044\frac{r_H}{r_p}+2.089\left(\frac{r_H}{r_p}\right)^3-0.948\left(\frac{r_H}{r_p}\right)^5\right)$$

which is valid for $0 \le \frac{r_H}{r_p} < 0.4$ and assumes the solute particle is centered on the tube axis. Regardless of the solution found in different regimes of this model,[12] one feature is always present:

$$(2.11)\quad \frac{D}{D_{SE}} \to \left(1-\frac{r_H}{r_p}\right)^n \text{ as } \frac{r_H}{r_p} \to 1,$$

with $n > 1$. This produces a gradual decrease in D/D_{SE} as $\frac{r_H}{r_p} \to 1$ compared to the sharp decrease seen if $n < 1$. As we will see later (Chapter 5), this is not the behavior found in the disordered media examined in this work. The inapplicability of hydrodynamic models to disordered porous media arises from the two oversimplifications assumed in the model. First, is the assumption that $r_H >> r_{solvent}$. Frequently, $r_p >\sim r_H \sim r_{solvent}$ for small solute molecules, and so the hydrodynamic drag is not a realistic model of the force acting on the solute. Second, and most important, is the description of the porous medium as a collection of long, straight, independent channels. Disordered porous materials are characterized by highly interconnected pores that are typically very irregular in shape. For these reasons, it is difficult to view bundled tube models as valid descriptions of disordered materials.

III b. Discrete network models

A more realistic model of disordered porous materials views the pore space as a connected network[13] where each bond in the network can be viewed as a pore. Each bond can then be assigned a conductivity that is related to the size and shape of a corresponding pore and is independent of all other pores. Just as in a real material, these bonds are connected at nodes to form the full network. This level of detail makes it quite complicated to solve for any transport property exactly and so, at least initially, we will restrict the bonds to be identical.

Networks like these display percolation behavior.[14] If bonds are randomly removed from an initially complete network (e.g. a cubic lattice, where the bonds connect nearest neighbor sites), eventually a bond is removed which severs the last path connecting one side of the network to the other (Figure 2.4). The fraction (p) of the original number of bonds that remain at this critical point defines the percolation threshold, p_c. A lattice filled with bonds such that $p < p_c$ is disconnected, while for $p > p_c$ there is at least one sample-spanning path. This phenomenon is well known in systems such as resistor networks and metal/insulator composites where an increase in the fractional volume of metal can change the system from insulating to conducting.[15] In porous media, the porosity ϕ (the ratio of the pore volume to the total volume), is often viewed as being equivalent to p in a bond network. We should note that percolation is not a true critical phenomenon because it does not involve a dynamic process.

One method for analyzing these complex networks is the effective medium approximation (EMA).[16] Originally developed to calculate the dielectric constant of an

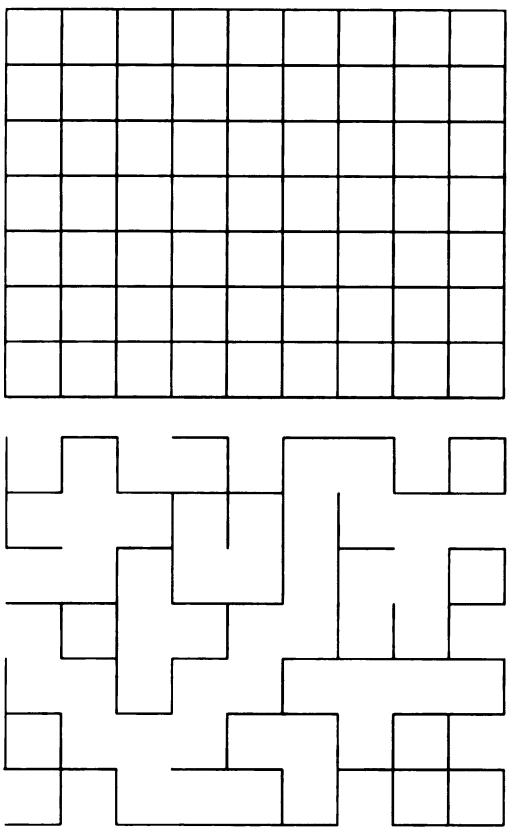

Figure 2.4: A two dimensional bond network. Top: at p = 1, bottom: at p = 0.37. An infinite square lattice has a percolation threshold of $p_c = 0.5$.

insulator with metal inclusions, EMA looks at a single bond and calculates the effect of all the other bonds in the network on it. The rest of the network is divided into two regions, the nearby bonds whose effect must be determined explicitly, and the distant bonds which are replaced by a continuous effective field. Kirkpatrick[17] applied EMA to a network of conducting bonds to make the first quantitative prediction of a percolation threshold in a resistor network. EMA was used because it was the only analytical theory capable of producing the necessary critical behavior. However, it tends to overestimate the real value of the threshold. Extensions to three dimensions have shown that EMA

becomes even less accurate than for 2-dimensional nets. Several modifications to EMA[18] have been made which improve the behavior near p_c and make useful quantitative predictions possible. However, EMA models require an accurate knowledge of the distribution of pore sizes (the distribution of the conductances of the individual bonds) and of the connectivity of the network (how many bonds meet at each node) in order to predict properties such as the total conductivity of the network. For disordered porous media, this information is not typically well known, limiting the effectiveness of EMA.

A network near the percolation threshold behaves as a system near a critical point and therefore its properties in that region behave as power laws of the occupation probability p (recall that p is the ratio of the number of completed (occupied) bonds to the total number of possible bonds). For example, near p_c it is found that:

(2.12) $P \propto (p - p_c)^{\beta}$, $\xi \propto (p - p_c)^{-\nu}$, and $\sigma \propto (p - p_c)^{\mu}$

where P is the fraction of all possible bonds that are occupied and connected to the sample-spanning cluster, ξ is the correlation length of the system (proportional to the average cluster radius when $p < p_c$, and to the distance between locations on the network that are connected by more than one path, when $p > p_c$), and σ is the electrical conductivity of a percolating network of resistive bonds. Critical exponents like β (= 0.41) and ν (= 0.88), which depend on the connectivity of the network, can be found through simulations, experiments, and scaling arguments and depend only upon the dimensionality of the system, not the details of the network structure. This is one of the strengths of percolation theory, it is a general statistical description with wide applicability. However, not all percolation exponents behave in this universal fashion.

Specifically, transport exponents like μ ($\cong 2$ for a simple uniform bond network), and exponents of elastic properties do depend on the details of the network model, as we will see later.

Before discussing the percolation predictions for diffusion, it is important to note a few aspects of conduction on a percolating network. Because conduction requires a continuous path across the network, it can only occur on the sample spanning cluster (also referred to as the infinite or the percolating cluster). Any bonds which are part of isolated clusters cannot contribute. The spanning cluster can be viewed as having two

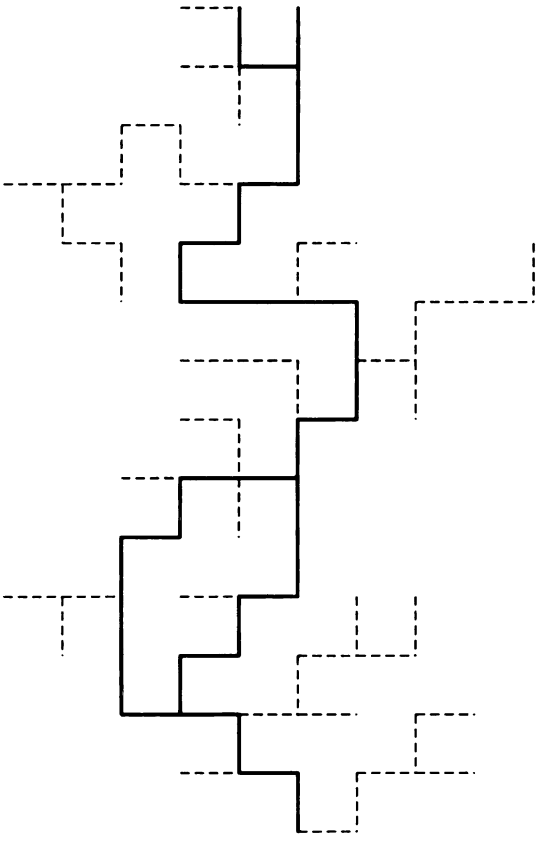

Figure 2.5: A schematic of the percolating cluster (also called infinite or sample-spanning cluster). The solid lines are the bonds making up the backbone of the cluster. The dashed lines are the side branches.

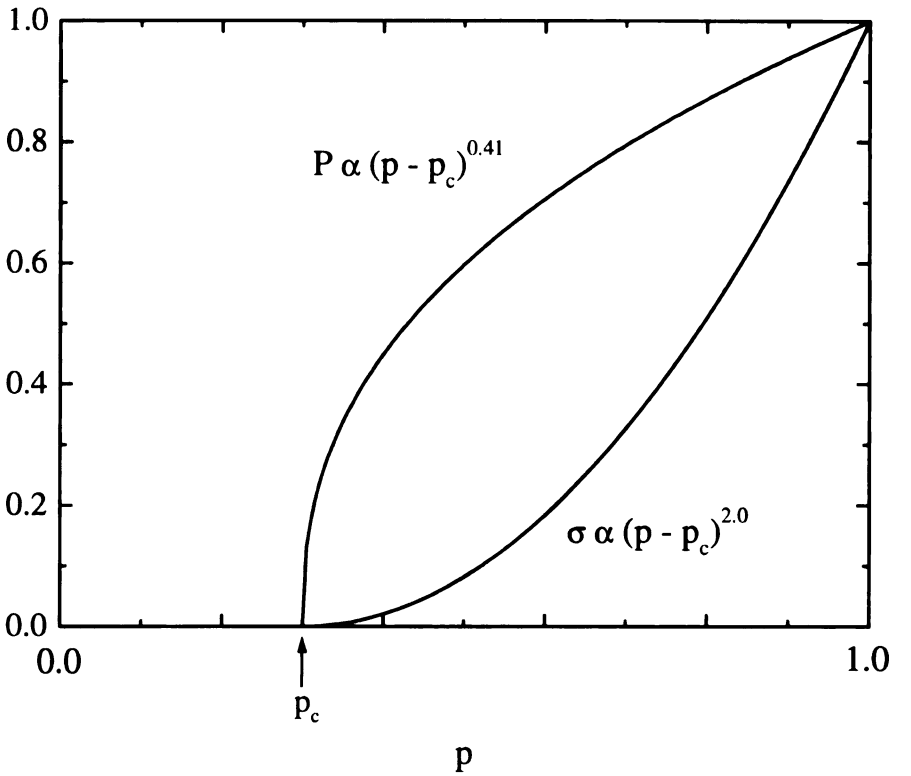

Figure 2.6: The functional dependence of the percolation probability P, and the conductivity σ of a three dimensional network near p_c.

components: a backbone and side branches (Figure 2.5). The backbone is made up of those bonds that actually carry current, while the side branches (which are connected to the backbone but lead nowhere) do not. This is the reason for the difference in the percolation exponents of P and σ (β = 0.41 and μ = 2.0, respectively, in three dimensions). P measures the number of total bonds in the spanning cluster while σ

depends only on the number of bonds in the backbone. Figure 2.6 illustrates the behavior of P and σ near the threshold.

A direct method for analyzing the properties of a fluid in a porous material is through the use of computer simulations. A model of the pore structure is developed (where the pore network is viewed as a network of bonds, with each pore corresponding to an occupied bond, and the solid corresponding to the missing bonds) and random walkers are released to explore the environment just as a diffusing molecule does. This idea, first proposed by de Gennes,[19] has been used extensively to determine the transport properties of percolation networks both near and far from the threshold, as well as to model the signals produced in pulsed field gradient spin echo NMR diffusion experiments.[20] These simulations have provided an excellent means of examining the properties of idealized networks.

Earlier in the chapter, it was shown that the diffusion coefficient measured in a porous material depends upon the length scale that the measurement is made on. For the same reason, a diffusion measurement on a network will also depend upon whether the network is above or below the percolation threshold. If a random walker is released onto the network and allowed to move along the occupied bonds, the MSD for very long times will be:

$$\langle r^2 \rangle \propto D(p)\, t, \text{ for } p_c < p \leq 1, \text{ and large } t$$

$$\langle r^2 \rangle \propto \text{constant, for } p < p_c, \text{ and large } t \tag{2.13}$$

$$\langle r^2 \rangle \propto t^n, \text{ for } p = p_c, \text{ and large } t$$

Therefore, above p_c, normal diffusion occurs (although the diffusion coefficient may be reduced from its value at p = 1 when $p_c < p < 1$). Below p_c, the walker is confined to a finite size cluster of bonds, and won't diffuse any farther than some asymptotic distance related to the average size of that cluster. Right at p_c, these two regimes connect and produce "anomalous" diffusion where $n \neq 1$. To find n, we first must determine the behavior of $\langle r^2 \rangle$ below p_c. The following discussion closely follows the derivation found in Stauffer and Aharony.[21]

Here, the network is viewed as a collection of sites rather than bonds such that a walker can move to a nearest neighbor site only if that site is "occupied." Viewing the lattice as a collection of sites rather than bonds changes only the predictions of the percolation threshold--not the values of the exponents.[22] If a "blind" walker (a walker that cannot tell if a neighboring site is occupied or not) is placed at site i on the lattice, where each site has z neighbors, the probability (P_i) that the walker is at site i evolves with time as:

$$(2.14)\quad P_i(t+1) - P_i(t) = \sum_j [\gamma_{ji} P_j(t) - \gamma_{ij} P_i(t)] = \frac{dP_i}{dt},$$

where γ_{ij} is the probability per unit time of hopping from i to j (= 0 if site j is missing, = 1/z if site j is occupied). Looking only at a single finite cluster containing s occupied sites, and for very long times so that the walker can visit each site many times, P_i will reach an asymptotic value and $\frac{dP_i}{dt} = 0$. Equation 2.14 then implies that all sites are equally probable, meaning that $P_i(t \to \infty) = \frac{1}{s}$. Therefore, the asymptotic distance that a

diffuser can reach on this finite cluster will simply be the average distance between two points in the cluster, R_s, the average cluster radius. For $p < p_c$, all the clusters are finite, so a walker placed at random on the network has a probability of $n_s s$ of being on a cluster of size s, where n_s is the number of clusters of size s per lattice site. Therefore, the MSD is

(2.15) $\langle r^2 \rangle (t = \infty, p < p_c) = \sum_s n_s s R_s^2$.

If $n_s \propto s^{-\tau} e^{-cs}$, $c \propto |p - p_c|^{\frac{1}{\chi}}$, and $R_s \propto s^{\chi\nu}$, where $\chi = \frac{1}{\beta + \gamma}$ and $\tau = 2 + \frac{\beta}{\beta + \gamma}$ it is easily shown that

(2.16) $\langle r^2 \rangle (t = \infty, p < p_c) \propto (p_c - p)^{\beta - 2\nu}$.

Having determined the MSD below p_c, we now turn to its behavior above p_c. We know that in this range $\langle r^2 \rangle \propto D(p)t$, and that D(p) decreases to zero as p approaches p_c, but have not determined how D(p) varies with p. Einstein[23] showed that the diffusion coefficient of a particle is proportional to its mobility, defined as the ratio of its velocity to the applied force. For a conduction electron, the mobility is simply the current divided by the applied voltage, which is the conductivity. The diffusion coefficient is then proportional to the conductivity[24] and therefore,

(2.17) $D \propto \sigma \propto (p - p_c)^{\mu}$ and,

(2.18) $\langle r^2 \rangle (t = \infty, p > p_c) \propto (p - p_c)^{\mu} t$.

[It may be tempting to say that $D \propto \kappa$, the permeability of a fluid flowing through a channel, but it is an incorrect comparison. Because the forced flow of a fluid is

restricted by the boundary condition that the velocity is zero at the walls, a molecule at the center of a channel travels faster than one near the walls (Hagen-Poiseuille flow). A diffusing molecule, however, behaves more like a conduction electron whose mean free path is essentially the same anywhere in a resistive wire.]

To reconcile these two results (Equations 2.16 and 2.18) at $p = p_c$, we can introduce a scaling function that depends on both t and $p - p_c$:

$$(2.19)\quad \sqrt{\langle r^2 \rangle} \propto t^k \rho[(p - p_c)t^x] = t^k \rho[z].$$

For large t and $p > p_c$, this function must behave as Eq. 2.18, therefore:

$$(2.20)\quad \sqrt{\langle r^2 \rangle} \propto t^k [(p - p_c)t^x]^{\frac{\mu}{2}} \propto (p - p_c)^{\frac{\mu}{2}} t^{k + x\mu/2}$$

with $k = (1/2)(1 - x\mu)$. For large t and $p < p_c$, it must behave as Eq 2.16, so that

$$(2.21)\quad \rho[z \to \infty] \propto (-z)^{-\frac{k}{x}}$$

this makes $\sqrt{\langle r^2 \rangle}$ independent of t and implies that $k = (x/2)(2\nu - \beta)$. Combining these two values for k finds:

$$(2.22)\quad x = \frac{1}{2\nu + \mu - \beta} \text{ and } k = \frac{\nu - \beta/2}{2\nu + \mu - \beta}.$$

Therefore, for long times and at $p = p_c$, Equation 2.19 gives $\sqrt{\langle r^2 \rangle} \propto t^k$ as expected, where $k = 0.2$ in three dimensions.

It is important to realize that the discussion above is concerned with the diffusion of walkers that exist on all the clusters in network. When observed over sufficiently long times, $\langle r^2 \rangle$ is constant on finite clusters and linearly proportional to time on the infinite

cluster, therefore only the walkers on the infinite cluster contribute to the measured diffusion coefficient. In other words, on these time scales, only the fraction of walkers that are on the infinite cluster can influence D. Since P is the fraction of all possible bonds which are occupied and connected to the infinite cluster and p is the probability that any given bond is occupied, P/p is the fraction of all occupied bonds that are part of the spanning cluster. Because the walkers in this analysis are placed on occupied bonds at random, P/p is the fraction of walkers on the spanning cluster. Therefore, because only P/p walkers will contribute to the total diffusivity, we find that

(2.23) $Dt \propto \langle r^2 \rangle \propto (P/p)D't$,

where D is the diffusion coefficient over the entire network and D' is the diffusion coefficient on only the spanning cluster. This leads to:

(2.24) $D' = D\frac{p}{P} \propto D(p - p_c)^{-\beta}$

or,

(2.25) $D' \propto (p - p_c)^{\mu-\beta}$ for long times (and distances $>> \xi$).

As an aside, it has been shown that if walkers are released only on the percolating cluster, but that the region explored is kept so that $\sqrt{\langle r^2 \rangle} << \xi$, the diffusion is anomalous[25] due to the fractal nature of the percolation cluster over short length scales, with $\sqrt{\langle r^2 \rangle} \propto t^{k'}$, where $k' = \frac{\nu}{2\nu + \mu - \beta} = 0.26$. Numerical simulations have verified this behavior for walkers on both the infinite cluster and the whole lattice.[26]

Equations 2.17 and 2.25 show that the diffusion percolation exponent near the threshold depends upon whether the measurement is made over the entire network, or just on the spanning cluster. If the measurement is made on the entire network, the conductivity exponent will be recovered, but if only motion on the spanning cluster is followed, that exponent will be reduced by β. In a porous material that is filled with fluid while it is forming, the fluid will occupy all the pores, both those isolated and those connected to the surface. Porous materials filled with fluid after forming will have fluid only in those pores directly connected to the surface--which are the pores on the sample-spanning cluster (neglecting a tiny volume of dead end pores on the surface). A diffusion measurement made in these two materials should produce D and D', respectively. Until now, no one has experimentally measured this behavior of D' in a fluid system.

III c. Continuum network models

Up to this point we have been discussing percolation models in which every bond in the network is identical and the properties of the network arise solely from the number of occupied bonds. This is not necessarily a realistic model of real porous materials where the pores may vary considerably in size and shape. A more realistic model should consider how the pore network forms. One of these models, the "Swiss-cheese" model, creates a porous material by placing spheres at random into a volume, allowing them to overlap. As more spheres are added or as the spheres grow in size, the volume not occupied by spheres (the pore space) decreases until the percolation threshold is reached. This pore space is highly disordered, with pores whose shapes and sizes vary widely. A

two dimensional representation of the "Swiss-cheese" model is shown in Figure 2.7, where the shaded spheres make up the solid phase of the porous material, and the white space is the pore structure. The black lines indicate the bonds of the discrete network that the pore structure is mapped onto. In a three dimensional model, these discrete bonds are located at the edges of Voronoi polyhedra that are constructed around the centers of the spheres in the same manner as Wigner-Seitz cells are created. If the spheres are large enough to overlap one of these bonds anywhere along its length, that bond is considered to be absent from the discrete network (the dotted lines in Figure 2.7 are examples of

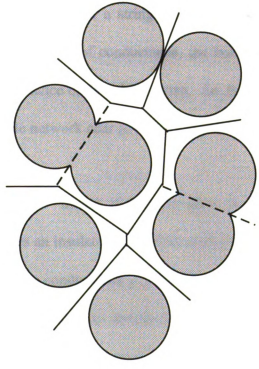

Figure 2.7: Two dimensional Swiss-cheese model. The shaded spheres are the solid phase and the white space are the pores. The solid lines are the open pores and the dotted lines are the closed pores of the corresponding discrete network. (After: S. Feng *et al*, Phys. Rev. B **35**, 197 (1987).).

these missing bonds). Each bond in this network corresponds to a narrowing in the pore structure that has a characteristic width δ. The transport properties (e.g. the conductivity) of each bond will vary with this width, producing a network where each bond is assigned a unique conductance.

The percolation cluster of a network can be viewed as a group of strings that connect to each other at nodes. Each string is made up of several "blobs" connected in series by "links." The blobs are regions of the network where more than one path exists from one side of the blob to the other. The links, on the other hand, are singly connected bonds--meaning that if any of the bonds in a link are broken, the whole string is broken. A bond broken in a blob, however, will not cause the whole string to break. Therefore, the "weakest" bond in the links of a string will determine the overall strength of the string. Looking at this in terms of conductance, the bond with the lowest conductance will determine the conductance of the whole string. So, in the "Swiss cheese" model, the conductivity of the whole network near p_c is determined by the bonds in the links with the smallest conductances.

In the "Swiss cheese" model, if the pore space is considered to be an electrical conductor and the spheres an insulator, a detailed analysis of the pore shapes produces an analytical description of the conductance g (a function of the width δ) of each bond on the network. This leads to a probability density function describing the distribution of the conductances of the smallest bonds (pores):[27]

(2.26) $P(g) \propto g^{-1/3}, \text{as } g \to 0,$

where g is the conductivity of an individual bond. The difference between this model and the networks discussed in the previous section is this distribution, because here each bond is given a different "strength," whereas all the bonds are identical in normal bond percolation. It is found that the transport properties (such as the conductivity, the permeability, or the elastic properties) of lattices with these distributions have different percolation exponents than networks where every occupied bond is identical.[28] However, the exponents for properties that are determined solely by the connectivity of the network (e.g. ν and β), are unchanged.

A general continuum model of this type can be defined on a random, discrete network such that:

(2.27) $P(g) \propto g^{-\alpha}$, as $g \to 0$

where P(g) is the distribution of the transport strengths g of the smallest bonds of the network, and g is related to the "width" of the bond δ, through:

(2.28) $g = \delta^{y+1}$.

Therefore, in this model, the distribution of conductances is singular as $g \to 0$.

If y and α are related by

(2.29) $y = \frac{\alpha}{1-\alpha}$,

then the probability distribution of δ behaves as:

(2.30) $P(\delta) \to$ constant, as $\delta \to 0$.

As the shapes of the pores in the network change, the values of y and α change. This will alter the transport properties of the system, but not the pore size distribution, which remains constant for small pores.

Feng *et al.*[29] use both a scaling analysis of the structure of the percolating cluster and a variational analysis of the conductance of the whole network to derive the upper and lower bounds of the transport percolation exponents for this distribution of conductances. For the conductivity exponent, $\bar{\mu}$, in this network, these bounds are:

(2.31) $\max(\mu_1 + y, \mu) \leq \bar{\mu} \leq \mu + y$, when $y > 0$ (or $0 < \alpha \leq 1$)

$\bar{\mu} = \mu$, when $y \leq 0$ (or $\alpha \leq 0$)

where μ is the conductivity exponent found for networks of identical bonds and

(2.32) $\mu_1 \equiv 1 + (d-2)\nu$.

Here, d is the dimensionality of the network, and ν (= 0.88 for d = 3) is the percolation exponent for the correlation length ξ. Therefore, for the three dimensional Swiss-cheese model, where α = 1/3 and y = 1/2,

(2.33) $2.38 \leq \bar{\mu}_{\text{swisscheese}} \leq 2.5$.

Feng *et al.* argue that these bounds are valid even if there are correlations in the occupation probabilities of the bonds, but that statistical correlations in the distribution of strengths among occupied bonds will make these bounds inapplicable.

These predictions have been borne out in both numerical[30] and experimental[31] studies, but mostly in two dimensions. Feng *et al.* also show that this model predicts a permeability exponent that is near values typically found in rocks, but they point out that the measurements are made in the region where

$$(2.34)\quad \frac{(\phi - \phi_c)}{\phi_c} > 1,$$

which is outside of the region where these asymptotic exponents should be found.

Therefore, we see that depending upon the characteristics of the porous material and the location of the fluid that is diffusing, there are several different predictions for the diffusive behavior near the percolation threshold. If the measurement is made in a fluid trapped within all the pores, the diffusion coefficient should vanish as a power law with an exponent μ. If the measurement is made in the pores of the percolating cluster, this exponent will be reduced to $\mu - \beta$. However, the value of μ depends upon the geometry of the pore structure as seen in the discussion of the Swiss Cheese model, giving at least four possible values for the diffusion exponent. A measurement of this exponent might provide information about the structure of the pore network.

IV. Previous studies of diffusion in porous glass

IV a. Techniques

Before the mid 1970's, studies of diffusion in microporous glasses were difficult to carry out in part because of the very slow diffusion that occurs in pores of molecular size. Long times were required to measure diffusion over macroscopic distances in standard diffusion cells, where a porous material is placed between two chambers of solvent, with a solute added to one chamber. The concentration of that solute is then monitored in the other chamber over time to measure the diffusion through the material. Most importantly, for slow diffusion, any cracks in the material, or leaks around it, will overwhelm the signal due to true diffusion through the pores.

Some of the first systematic studies of diffusion in microporous glasses were made by Satterfield[32] and Colton.[33] In their experiments, porous glass beads were soaked in a solvent containing a known amount of solute, then transferred to a container of the pure solvent. The solute concentration in the solvent was then monitored to determine the rate at which the solute escaped from the pores. These measurements were of unsteady state diffusion, as the driving concentration gradient was continuously changing as molecules left the beads. They compared their results to hydrodynamic models and found some agreement with some solutes if an arbitrary "tortuosity" parameter, X, was included to relate D/D_o to r_H/r_p,

$$\frac{D}{D_o} = \frac{1}{X} f\left(r_H / r_p\right). \tag{2.35}$$

Here, $f(r_H/r_p)$ is the result of a hydrodynamic model (like the Renkin Equation, Equation 2.10) of a sphere diffusing down a straight tube.

The last two decades has seen a dramatic increase in the number of techniques available for the study of diffusion inside porous materials. Techniques such as pulsed field gradient spin echo nuclear magnetic resonance (PFGSE), dynamic light scattering (DLS), forced Rayleigh scattering (FRS), and fluorescence recovery after photobleaching (FRAP) all emerged to allow the study of fluid diffusion in the interior of a porous material without the need for any overall concentration gradient. By measuring over relatively small length scales, the measurement of extremely slow diffusion became possible on a reasonable graduate student time scale. Some of these methods are also capable of measuring diffusion in a directional manner to determine if any anisotropy exists in the fluid movement.

PFGSE is a variation of standard spin-echo NMR.[34,35] In a typical spin-echo experiment, a uniform magnetic field in the $\hat{z}$ direction causes the protons of the hydrogen nuclei to precess about the z axis with frequency ω_0, which depends upon the magnitude of the field. A radio-frequency pulse applied along the y axis forces the precessing "spin packets" into the x-y plane where they precess at different rates. After a time τ, a second, longer, RF pulse is applied which essentially reverses the precessional motion of the spin packets. If all the packets maintain their phase coherence, they will all reconverge at a time τ after the second pulse, producing the spin-echo signal.

In PFGSE, an additional inhomogeneous magnetic field is applied for a time δ in the $\hat{z}$ direction, with a magnitude g*z. This field is applied twice, once after the first RF pulse, and then again (a time Δ later) after the second RF pulse (Figure 2.8). Because the

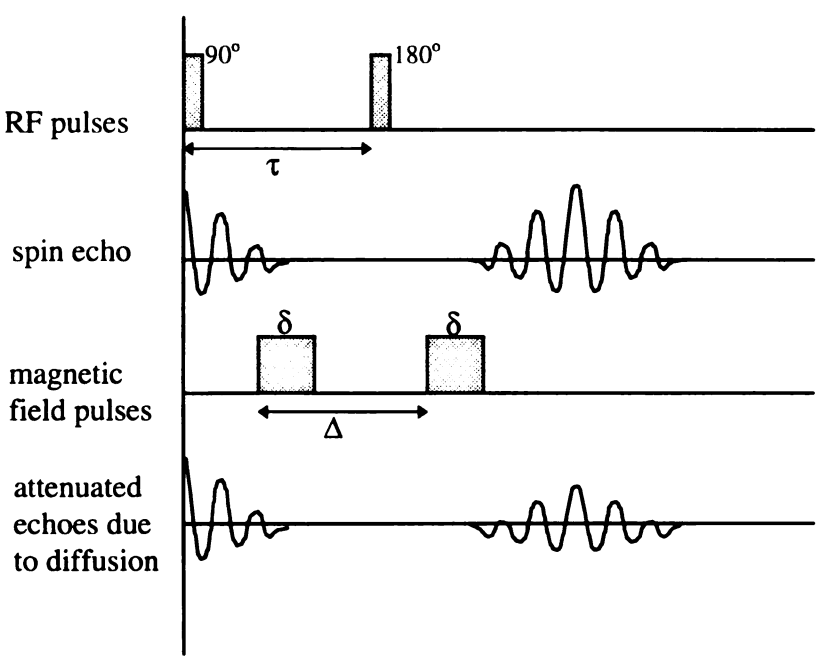

Figure 2.8: Pulsed field gradient spin echo NMR pulse sequence. (After: A. Mitzithras *et al*, J. Mol. Liq. **54**, 273 (1992).).

resonant frequency of the protons depends upon the magnetic field, this additional field will increase ω_o while it is applied. The second pulse (after the precession has been reversed) corrects for the effect of the first pulse. However, if a proton has moved along the z axis during the time Δ between the two field gradient pulses, it will experience a different magnetic field during the second pulse than it did during the first pulse. In this case, the resonant frequency of that proton during the two pulses will be different, and the second pulse will not correct for the first one. Therefore, the amplitude of the spin-echo will be reduced. For motion due to diffusion along the z axis, this decrease in the spin-echo amplitude will be:

(2.36) $\Psi = e^{-\gamma^2\delta^2 g^2 D\Delta}$,

where γ is the gyromagnetic ratio for the proton, and D is the diffusion coefficient along the z axis.

PFGSE experiments typically measure diffusion over times of a few milliseconds which corresponds to length scales of a few microns. It is not easily used to measure diffusion over large length scales. When using PFGSE to measure diffusion in a porous material, magnetic impurities on the pore walls will interact with the diffusing particles, and destroy the phase coherence. This relaxation of the magnetism is a significant consideration in these experiments, and can lead to misinterpretations of the diffusion coefficient.[36]

Dynamic Light Scattering measures diffusion by simply measuring the temporal correlation of fluctuations in light scattered from molecules in a liquid.[37] A laser beam of wavevector $\vec{K}_o$ is incident on the sample (placed at the origin of the coordinate system,

see Figure 2.9), and the scattered light collected at position $\vec{R}$ at an angle of θ from $\vec{K}_o$. The electric field of this scattered light can then be written as:

$$(2.37)\quad \vec{E}_{scattered}(\vec{R},t) = -\frac{\omega_o^2 n^2}{c^2 R} E_o e^{i(\vec{K}_s \cdot \vec{R} - \omega_o t)} \alpha(\vec{K},t'),$$

where ω_o is the frequency of the incident light, n is the index of refraction of the surrounding medium, $\vec{K}_s$ is the wavevector of the scattered light, $\alpha(\vec{K},t')$ is the polarizability of the scattering region, and $\vec{K} = \vec{K}_o - \vec{K}_s$. If the frequency of the scattered light is the same as the incident light, then $|\vec{K}| = 2|\vec{K}_o|\sin\left(\frac{\theta}{2}\right)$. Equation 2.37 shows that the fluctuations of the scattered light arise from fluctuations of the polarizability in the scattering volume which in turn arise from the motion of molecules in the solvent.

The autocorrelation function of the intensity of the scattered light is measured:

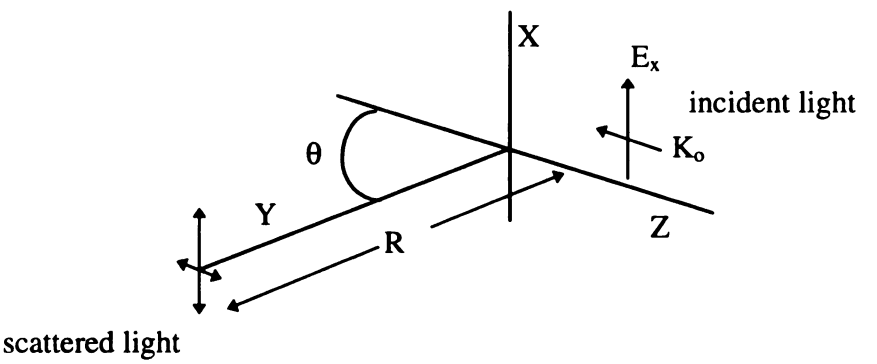

Figure 2.9: Dynamic Light Scattering experimental geometry. (After: K.S. Schmitz, *Dynamic Light Scattering by Macromolecules* (Academic Press, New York, 1990).).

$$(2.38)\quad \langle I(0)I(t)\rangle = \lim_{T\to\infty}\frac{1}{T}\int_{-T/2}^{T/2} I(t')I(t'+t)dt' = \langle I(0)\rangle^2 + Q_e^{\,2}\left\langle \left|\vec{E}^*(0)\cdot\vec{E}(t)\right|\left|\vec{E}^*(t)\cdot\vec{E}(0)\right|\right\rangle,$$

where Q_e is a constant. For a normal diffusion process, this can be shown to be:

$$(2.39)\quad \frac{\langle I(0)I(t)\rangle}{\langle I(0)\rangle^2} = 1 + A\left(e^{-DK^2t}\right)^2,$$

where D is the diffusion coefficient, and A is a constant. Therefore, to determine D, the decay of the correlation function is measured and fit to an exponential. Typically, however, the measurement is made at several values of K to verify that D is independent of K. For scattering at optical wavelengths, K ranges from approximately 5×10^4 to 4×10^5 cm^{-1}, which corresponds to a range of length scales from about 0.1 μm to 1 μm.

FRS (discussed in detail in Chapter 3) measures diffusion by monitoring the decay of a sinusoidal modulation of the optical properties in a fluid. Two coherent laser beams cross each other in the liquid, creating a sinusoidal interference pattern to excite a tracer molecule, giving rise to a corresponding modulation in the optical properties in the fluid (e.g. the index of refraction). The diffraction of a third laser beam off this modulation is used to monitor its creation and decay as the two exciting lasers are turned on and off. The decay rate of the modulation is shown to be:

$$(2.40)\quad \frac{1}{\tau} = Dq^2 + \frac{1}{\tau_I},$$

where D is the diffusion coefficient, q is the wavevector of the sinusoidal modulation, and τ_I is the intrinsic lifetime of the excitation. Therefore, D and τ_I are determined by measuring the decay rate at several values of q (which is set by the angle between the two

exciting beams). q ranges from approximately 630 to 5 x 10^4 cm^{-1}, corresponding to a length scale of about 100 μm down to 1 μm.

FRAP is very closely related to FRS, as it also uses interfering lasers to create a modulated pattern in the fluid, as illustrated in Figure 2.10.[38] In FRAP, however, it is a pattern of fluorescent dye. A fluorescent dye is dissolved in the fluid, and the interference pattern is turned on at a very high intensity for a short time. This pulse of light bleaches the dye in the bright bands of the interference pattern. (When dye is bleached, it no longer fluoresces.) At the end of this pulse, the intensity of the interference pattern is reduced to a level which will cause the dye to fluoresce, but not bleach it, and the pattern itself is slightly oscillated by modulating the phase of one of the two interfering beams. The intensity of the in-phase fluorescent emission from the sample is monitored over time

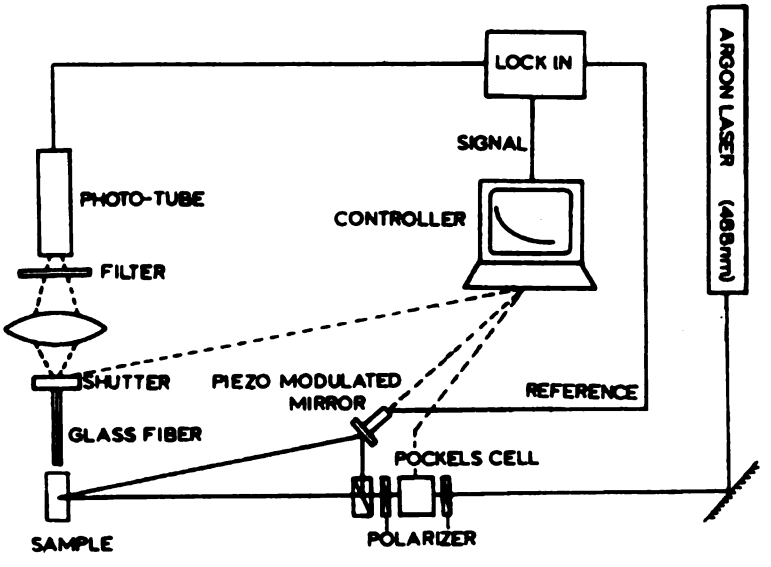

Figure 2.10: Fluorescence recovery after photobleaching experimental setup. (From: A. van Blaaderen *et al*, J. Chem. Phys. **96**, 4591 (1992).).

using phase sensitive detection.[39] As the unbleached dye diffuses into the regions that had been bleached with the initial pulse, the signal increases until the concentration becomes spatially uniform. The rate of this fluorescence recovery is:

$$(2.41)\quad \frac{1}{\tau} = Dq^2,$$

where D and q are the same as in a FRS experiment. The length scales involved in FRAP are the same as FRS. The advantages of FRAP over FRS are that the bleaching is permanent, so there is no intrinsic lifetime of the excitation, and the sample does not have to be transparent. FRS needs transparent media because it relies on the diffraction of the probe beam, and any scattering in the sample will affect the diffracted signal. However, because the bleaching is permanent in FRAP, the signal level decreases with every pulse, making signal averaging difficult, while the finite lifetime in an FRS experiment allows an experiment to be repeated many times without having to change the fluid.

IV b. Experiments

One well-characterized commercial porous glass (Vycor 7930) has been used in fluid diffusion studies on several occasions. Vycor is a borosilicate glass which is heat treated to phase separate it into boron rich and boron poor regions. It is then placed in an acid bath to selectively etch the boron rich regions--leaving behind a tortuous network of pores of highly uniform size (pore radius of ~ 25 Å).[40] Dozier *et al.* [41] used FRS to measure the diffusion of azobenzene in alcohol-toluene mixtures inside the pores of Vycor. Diffusion in glasses is affected by two main things: the geometry of the pore network and the adsorption of the diffusing molecules to the pore surface. Dozier *et al.*

were interested in determining only the effect of the pore network structure on diffusion, and so chemically blocked the adsorption of azobenzene to the walls.

The Vycor was first soaked in methanol so that it would attach to the binding sites (hydroxyl groups) on the surface, and not allow the azobenzene to adsorb when it was added to the fluid. However, with this treatment they found FRS signals that were independent of the grating wavevector, q, indicating that the azobenzene was not diffusing (Figure 2.11). Their second attempt was to derivatize the glass with 1-propanol in order to replace the hydroxyl groups. This was done by boiling the Vycor in 1-propanol for 24 hours. With this treatment, they found normal diffusive behavior (an FRS decay rate that was proportional to q^2, see Figure 2.12) with a normalized diffusion

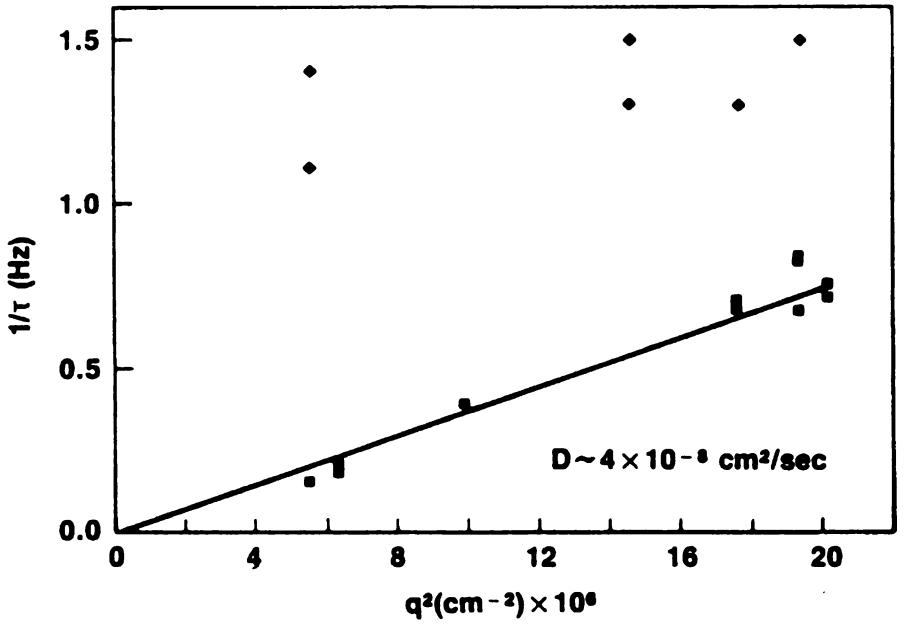

Figure 2.11: FRS decay rate for azobenzene in methanol/toluene within Vycor. The squares (diamonds) are data from locations that do (do not) behave as $1/\tau \propto q^2$. (From: W.D. Dozier *et al*, Phys. Rev. Lett. **56**, 197 (1986).).

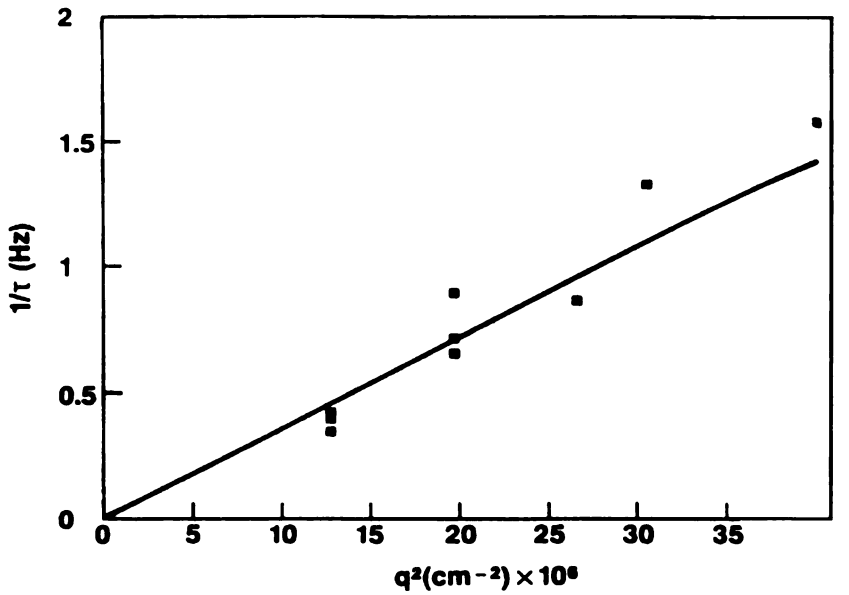

Figure 2.12: FRS decay rate for azobenzene in 1-propanol/toluene within Vycor. (From: W.D. Dozier *et al*, Phys. Rev. Lett. **56**, 197 (1986).).

coefficient (D/D_o) on the order of 0.01-0.03 for two different solvents. However, even in their treated sample, they have a small number of quite scattered data points. In Figure 2.12, the slope of the fitted line is forced to be lower than the slope of the data because the line (fitted with Equation 2.40) cannot intercept the y axis below the origin. This leads to considerable uncertainty in their conclusions.

They compared their result with two separate models of diffusion in porous materials. One was the bundled-tube model from which they calculated a value of the "tortuosity", T, of the pore network:

(2.42) $D/D_o = \phi/T$,

where $\phi = 0.28$ is the porosity of their Vycor sample. However, as they pointed out, this tortuosity parameter is not well defined and does not provide any true measurement of the geometry of the pore network.[42]

At the time, the pore network of Vycor was suspected to be fractal in nature, so a model relating the estimated fractal dimension and the diffusion coefficient was compared to their measured result for D/D_o. However, in a later publication they noted that the pore network in Vycor had been shown to not be fractal, and therefore this comparison was inappropriate.[43] Finally, they found an order of magnitude difference between their measured value of D/D_o and that calculated from the Renkin equation (Eq 2.10). That is not surprising, however, since the Renkin equation is based on a model of a single straight tube, and the pores in Vycor do not resemble straight tubes. Because only one glass was examined in this study, any conclusions drawn about the dependence of D/D_o on the porosity or pore size is, at best, speculative.

At the University of Massachusetts, Guo *et al.*[44], made DLS measurements of polystyrene diffusing in the same Vycor glass. Again, adsorption of the diffusers to the surface was a concern, so the hydroxyl groups on the surface of the silica were reacted with hexamethyl disilazane to prevent hydrogen bonding of the polystyrenes. For four polystyrenes, ranging in molecular weight from 2500 to 13,000, they found D/D_o to range from 0.1 to 0.01 (see Figure 2.13, where the normalized diffusion is plotted versus $\lambda_H = r_H/r_p$, the ratio of the polystyrene hydrodynamic radius (r_H) to the pore radius in the Vycor glass). These values are the same or greater than what Dozier *et al.* found for the diffusion of the much smaller azobenzene molecule. Guo *et al.* attributed this difference

to possible residual unreacted hydroxyl groups in the earlier experiment, which would also result in a reduced diffusion coefficient in the pores. The authors also stated that they briefly examined the diffusion of azobenzene in the Vycor glass that had been treated with hexamethyldisilazane, and found that the diffusion was occurring faster than they could measure. This is very surprising, because the diffusion coefficient of azobenzene and Methyl Red in solvents such as methanol/toluene, 1-propanol/toluene, benzene, ethanol, and 2-propanol is in the range of 1 x 10^{-6} to 1 x 10^{-5} cm^2/s, which is easily measurable.[45] It is hard to explain how azobenzene in Vycor could diffuse faster than that.

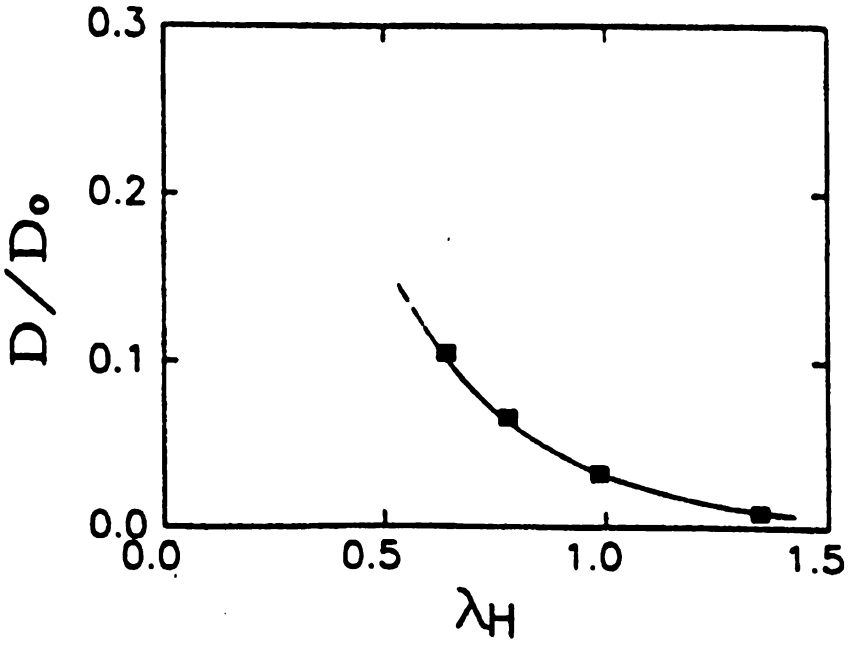

Figure 2.13: Normalized diffusion coefficient, D/D_o, of polystyrene in Vycor. The x-axis is the ratio of the polymer hydrodynamic radius (r_H) to the average pore radius (r_p) of the glass. Shown are data for polystyrenes of four different molecular weights. (From: Y. Guo *et al*, Phys. Rev. B **50**, 3400 (1994).).

One drawback to the surface treatments used in both these experiments is their modification of the pore structure.[46] The replacement of relatively small hydroxyl groups with larger molecules in small channels, or at a small opening to another pore, can close off portions of the pore network to the fluid. By restricting the fluid to the largest pores in this way, the apparent diffusivity in the material will increase. *Neither of these studies examined the dependence of the diffusion on the pore size of the glass.*

In an extensive series of DLS experiments,[47] the group at the University of Massachusetts examined the behavior of polystyrene diffusion in acid-etched glasses similar to Vycor as a function of the polymer molecular weight, polymer concentration, and the solvent species. The glasses studied in these experiments had pore radii ranging from 75 to 1866 Å, which are considerably larger than the pores in Vycor. They varied the molecular weight of the polystyrene to change the hydrodynamic radius of the probe molecule and compared their results in each glass to predictions of hydrodynamic models:

$$(2.43)\quad \frac{D}{D_o} = \frac{1}{X} f\left(\kappa \, r_H / r_p\right),$$

where $f(r_H/r_p)$ is one of several hydrodynamic models, such as the Renkin equation, X is the "tortuosity", an extra free parameter to take into account that the pores are connected rather than single, isolated tubes, and κ, another free parameter to account for the fact that the linear polystyrene molecules are not the spheres that hydrodynamic models are derived for.[48] This analysis was able to fit their data for small values of r_H/r_p, but the use of parameters such as the tortuosity makes it difficult to draw any useful conlusions about the pore size dependence of diffusion in these large pore, long molecule systems. In these studies, they only looked at how D/D_o varied with r_H, not with changes in r_p.

Finally, the same group at the University of Massachusetts used FRS to measure polystyrene diffusion in suspensions of silica in polystyrene. As expected, they found that the diffusion coefficient decreased with increasing volume fraction of silica (up to approximately 13% silica by volume), and showed that above 6% silica, where the suspension eventually gels, the behavior deviated from theories of diffusion in suspensions. In these gelling samples, they also tracked the diffusion coefficient over time, and found a 5% reduction in D as the suspension gelled.

One systematic PFGSE study of the pore size dependence of diffusion has been made with cyclohexane diffusing in porous silica powders and beads with pore radii ranging from 245 - 30 Å.[49] Cyclohexane was chosen because it interacts only weakly with the silica surface and therefore is not hindered by chemical bonding. As the pore radius, R_p, of the silica samples decreases, they found that D/D_o spans the range of 0.91 - 0.61. They fit their data to an empirical function (Figure 2.14a)

$$\frac{D}{D_o} = e^{-b(2r_p)^{\varepsilon}} \tag{2.44}$$

(with b = 71.3 and ε = -1.02), which is based on no model and related their result to a model based upon diffusion through stacks of thin membranes to describe 1/b as an "effective permeability." Although their data shows the expected trend of D/D_o decreasing with r_p, their data is limited to relatively large values of D/D_o, and they make no statement about how D/D_o approaches zero. Also, they found no systematic dependence of the diffusion on the limited range of porosities of their samples (Figure 2.14b).

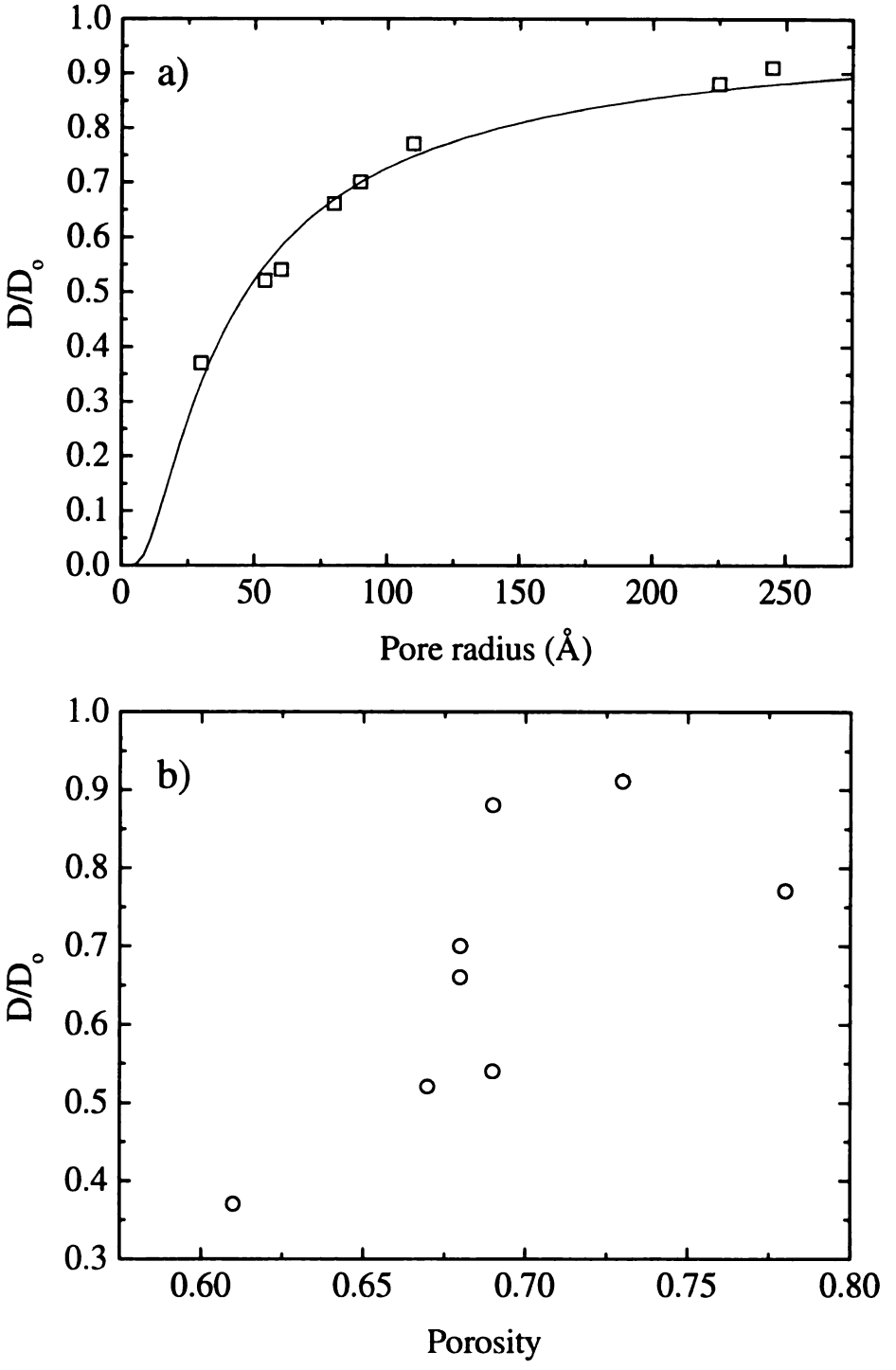

Figure 2.14: Normalized diffusion coefficient of cyclohexane in sol-gel grown silica as a function of (a) the pore radius and (b) the porosity. (Data from: A. Mitzithras *et al*, J. Mol. Liq. **54**, 273 (1992).).

In other studies: PFGSE experiments by Kärger[50] examined the temperature dependence of diffusion of several solvents in porous glasses although they did not draw a conclusion as to the dependence of diffusion on the pore size or structure. Later, D'Orazio[51] used PFGSE to study the diffusion in partially filled pores of single silica glass and found the behavior to be described by a variation of Archie's Law.[52] And, in a FRAP experiment, where the length scale of the diffusion measurement is easily controlled, Messager[53] saw the crossover from intrapore (free fluid-like) diffusion to interpore (hindered) diffusion in large porosity fumed silica gels.

V. Conclusions

With these past experiments as a base, the work described in this thesis was initiated to examine the behavior of diffusion in porous glasses as a function of both their porosity and average pore radius and use the results to distinguish between the models that attempt to describe this behavior.

References

[1] H. Darcy, *Les fontaines publiques de la ville de Dijon*, (Dalmont, Paris, 1856); A. E. Scheidegger, *The Physics of flow through porous media*, 3rd ed., (University of Toronto Press, Toronto, 1974).

[2] A.E. Scheidegger, ibid., p. 140.

[3] W. Jost, *Diffusion in Solids, Liquids, Gases* (Academic Press, New York, 1960).

[4] R. Brown, Phil. Mag. (4) **1828**, 161.

[5] A. Einstein, Ann. D. Phys. **17**, 549 (1905); A. Einstein, *Investigations on the Theory of the Brownian Movement*, edited by R. Fürth, translated by A.D. Cowper (Dover, New York 1956).

[6] W. Jost, ibid., p.7.

[7] M.A. Knackstedt, B.W. Ninham, and M. Monduzzi, Phys. Rev. Lett. **75**, 653 (1995); A. Ott et al, Phys. Rev. Lett. **65**, 2201 (1990); M. Sahimi, Rev. Mod. Phys. **65**, 1393 (1993).

[8] D. Stauffer and A. Aharony, *Introduction to Percolation Theory*, (Taylor and Francis, London, 1994).

[9] T.H. Soloman, E.R. Weeks, and H.L. Swinney, Phys. Rev. Lett **71**, 3975 (1993).

[10] F.A.L. Dullien, *Porous Media: Fluid Transport and Pore Structure* (Academic Press, New York, 1979), p. 42.

[11] W.M. Deen, Amer. Inst. Chem. Eng. J. **33**, 1409 (1987).

[12] W.M. Deen, Amer. Inst. Chem. Eng. J. **33**, 1409 (1987).

[13] Dullien, ibid., p. 44.

[14] D. Stauffer and A. Aharony, *Introduction to Percolation Theory*, (Taylor and Francis, London, 1994); S.R. Broadbent and J.M. Hammersley, Proc. Camb. Phil. Soc. **53**, 629 (1957).

[15] B.I. Shklovskii and A.L. Efros, *Electronic Properties of Doped Semiconductors* (Springer-Verlag, Berlin, 1984); *Electrical Transport and Optical Properties of Inhomogeneous Media*, edited by J.C. Garland and D.B. Tanner (AIP Press, New York, 1978).

[16] M. Sahimi, *Applications of Percolation Theory* (Taylor and Francis, London, 1994); R. Landauer in *Electrical Transport and Optical Properties of Inhomogeneous Media*, edited by J.C. Garland and D.B. Tanner (AIP Press, New York, 1978).

[17] S. Kirkpatrick, Rev. Mod. Phys. **45**, 574 (1973).

[18] M. Sahimi, L.E. Scriven, and H.T. Davis, J. Phys. C. **17**,1941 (1984).

[19] P.G. de Gennes, La Rechereche **7**, 919 (1976).

[20] P.N. Sen *et al*, Phys. Rev. B **49**, 215 (1994); D.J. Bergman *et al*, Phys. Rev. E **51**, 3393 (1995); L.M. Schwartz et al, Physica A 207, **28** (1994);L.M. Schwartz and J.R. Banavar, Phys. Rev. B **39**, 11965 (1989); A. Bhattacharya, S.D. Mahanti, and A. Chakrabarti, Phys. Rev. B **53**, 11495 (1996); M. Sahimi and V.L. Jue, Phys. Rev. Lett. **62**, 629 (1989); P. Argyrakis and R. Kopelman, Phys. Rev. B **29**, 511 (1984).

[21] D. Stauffer and A. Aharony, ibid., Chapter 6.

[22] D. Stauffer and A. Aharony, ibid, p. 17.

[23] A. Einstein, *Investigations on the Theory of the Brownian Movement*, edited by R. Fürth, translated by A.D. Cowper (Dover, New York 1956).

[24] P.G. de Gennes, La Rechereche **7**, 919 (1976).

[25] Y. Gefen, A. Arahony, and S. Alexander, Phys. Rev. Lett. **50**, 77 (1983).

[26] D. Ben Avraham and S. Havlin, J. Phys. A **15**, L691 (1982); R.B. Pandey *et al*, J. Stat. Phys. **34**, 427 (1984).

[27] S. Feng, B.I. Halperin, and P.N. Sen, Phys. Rev. B **35**, 197 (1987)

[28] P.M. Kogut and J.P. Straley, J. Phys. C **12**, 2151 (1979); A. Ben-Mizrahi and D.J. Bergman, J. Phys. C **14**, 909 (1981); J.P. Straley, J. Phys. C **15**, 2333 (1982); J.P. Straley, J. Phys. C **15**, 2343 (1982); J. Petersen *et al*, Phys. Rev. B **39**, 893 (1989).

[29] S. Feng, B.I. Halperin, and P.N. Sen, ibid.

[30] P.N. Sen, J.N. Roberts, and B.I. Halperin, Phys. Rev. B **32**, 3306 (1985); J.N. Roberts and L.M. Schwartz, Phys. Rev. B **31**, 5990 (1985).

[31] C.J. Lobb and M.G. Forrester, Phys. Rev. B **35**, 1899 (1987);L. Benguigui, Phys. Rev. B **34**, 8176 (1986).

[32] C.N. Satterfield, C.K. Colton, and W.H. Pitcher, Jr., Amer. Inst. Chem. Eng. J. **19**, 628 (1973).
[33] C.K. Colton, C.N. Satterfield, and C.-J. Lai, Amer. Inst. Chem. Eng. J. **21**, 289 (1975).

[34] J. Kärger, in *Access in Nanoporous Materials*, edited by T.J. Pinnavaia and M.F. Thorpe (Plenum Press, NY, 1995), p. 175.

[35] W.B. Mims, in *Electron Paramagnetic Resonance*, edited by S. Geschwind (Plenum Press, NY, 1972), p. 263.

[36] A. Bhattacharya, S.D. Mahanti, and A. Chakrabarti, Phys. Rev. B **53**, 11495 (1996); P.N. Sen *et al*, Phys. Rev. B **49**, 215 (1994); P.P. Mitra and P.N. Sen, Phys. Rev. B **45**, 143 (1992).

[37] K.S. Schmitz, *An Introduction to Dynamic Light Scattering by Macromolecules* (Academic Press, Boston, 1990).

[38] D. Axelrod *et al*, Biophys. J. **16**, 1055 (1976).

[39] D. Chatenay *et al*, Phys. Rev. Lett. **54**, 2253 (1985); A. Imhof *et al*, J. Chem. Phys. **100**, 2170 (1994); A. van Blaaderen *et al*, J. Chem. Phys. **96**, 4591 (1992).

[40] P. Levitz *et al*, J. Chem. Phys. **95**, 6151 (1991).

[41] W.D. Dozier, J.M. Drake, and J. Klafter, Phys. Rev. Lett. **56**, 197 (1986).

[42] F.A.L. Dullien, *Porous Media: Fluid Transport and Pore Structure* (Academic, New York, 1979).

[43] J.M. Drake and J. Klafter, Phys. Today, May, 1990, p. 46.

[44] Y. Guo, K.H. Langley, and F.E. Karasz, Phys. Rev. B **50**, 3400 (1994).

[45] M. Terzima, K. Okamoto, and N. Hirota, J. Phys. Chem. **97**, 5188 (1993).

[46] J.M. Drake and J. Klafter, ibid.

[47] Y. Guo, K.H. Langley, and F.E. Karasz, Macromolecules **23**, 2022 (1990); I. Teraoka *et al*, Macromolecules **29**, 37 (1996); Z. Zhou *et al*, Macromolecules **27**, 7402 (1994); I. Teraoka, K.H. Langley, and F.E. Karasz, Macromolecules **26**, 287 (1993); Z. Zhou *et al*, Macromolecules **27**, 1759 (1994).

[48] M.T. Bishop, K.H. Langley, and F.E. Karasz, Macromolecules **22**, 1220 (1989).

[49] A.Mitzithras, F.M. Coveney, and J.H. Strange, J. Mol. Liq. **54**, 273 (1992).

[50] J. Kärger *et al*, J. Amer. Chem. Soc. **66**, 69 (1983); K. Fukuda *et al*, J. Phys. Soc. Jpn. **58**, 1662 (1989).

[51] F. D'Orazio *et al*, Phys. Rev. B **42**, 9810 (1990).

[52] G.E. Archie, AIME Trans. **146**, 54 (1942).

[53] R. Messager *et al*, Europhys. Lett. **10**, 61 (1989).

Chapter 3

EXPERIMENTAL TECHNIQUES

I. Introduction and background

The measurement of diffusion in fluids can be accomplished in many ways, up to and including the direct measurement of the position of individual particles. To make an accurate measurement of the diffusivity, it is necessary to measure the motion of large numbers of particles in order to determine the average behavior. Also, to find the long-time diffusion in porous materials, it is necessary to measure on length scales that are large compared to the pore size, but small enough to measure slow diffusion on reasonable time scales. Forced Rayleigh scattering satisfies these requirements in addition to providing a means of measuring diffusion over a known and variable length scale. This technique was first applied to the measurement of thermal diffusion within ruby and glycerol.[1] Since that time it has been extended[2] to measure the diffusion of fluids, polymers, and electrons in a variety of media.[3]

The first application of forced Rayleigh scattering (FRS) to mass diffusion was performed by Hervet *et al*,[4] who advanced the technique with the addition of photochromic tracer molecules. They also made use of the directional nature of FRS measurements to verify the anisotropic diffusion in the nematic phase of a liquid crystal. Numerous studies of diffusion in polymers with FRS have made significant advances in the study of the glass transition in those systems.[5] As discussed in Chapter 2, FRS has also been used in diffusion studies within Vycor porous glass.

II. Forced Rayleigh scattering theory

FRS is a four-wave mixing holographic measurement. Two coherent laser beams are interfered in the medium under study to produce a periodic excitation of the optical properties of the medium. This modulation, in effect a diffraction grating, can then be used to diffract another beam to monitor the strength of the excitation.

Figure 3.1 shows a schematic representation of the interference region of the two excitation beams of vacuum wavelength λ_{ex} that intersect at an angle of θ within the sample. The fringe pattern formed by the interference of these two TEM_{00} beams (illustrated in Figure 3.2) has a wavevector ($\vec{q}$) determined by the momentum matching

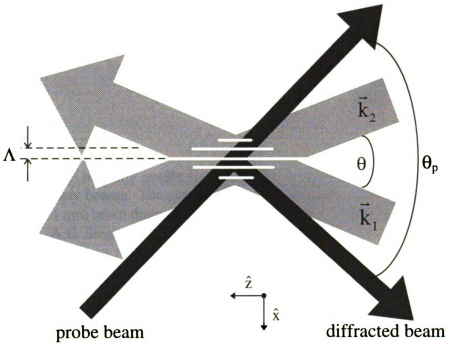

Figure 3.1: Schematic drawing of the interference region of a forced Rayleigh scattering experiment.

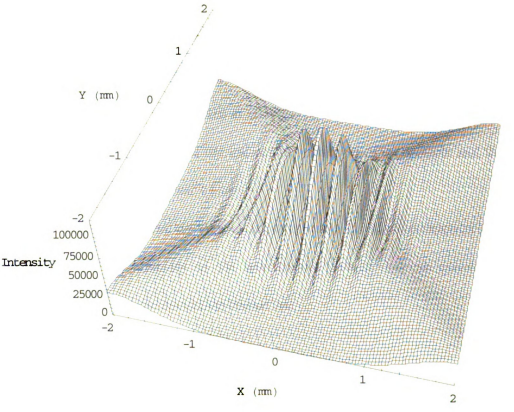

Figure 3.2: Intensity profile in the interference region of two crossed TEM00 laser beams. The parameters for this Mathematica calculation are: 4 mm beam diameter, $\lambda = 488$ nm, and $\theta = 0.0005$ rad. (After: A.E. Siegman, J. Opt. Soc. Am. **67**, 545 (1977).).

condition: $\vec{q} = \vec{k}_1 - \vec{k}_2$. The corresponding grating wavelength is then simply:

(3.1) $\Lambda = \lambda_{ex}/(2 \sin(\theta/2))$,

where $q = 2\pi/\Lambda$. For light of a visible wavelength, Λ can vary from ~1 - 100 μm. Equation 3.1 is valid for beams interfering in vacuum or for beams that have passed into the sample, providing that they are incident at an angle of $\theta/2$ to the normal of the sample face. If this condition is not met, then the indices of refraction of the sample and the air must be taken into account using Snell's Law.

If the two excitation beams are viewed as plane waves (a valid assumption if $\Lambda <<$ beam diameters), then the intensity of the interference pattern may be calculated as follows. The wavevectors of the excitation beams are:

(3.2) $\vec{k}_1 = \hat{z}k_z - \hat{x}k_x$, and $\vec{k}_2 = \hat{z}k_z + \hat{x}k_x$,

and therefore

(3.3) $\vec{q} = \pm \hat{x}q = \pm \hat{x}2k_x$.

The amplitude of the electric field in the interference region is then:

(3.4) $\vec{E}_o = \vec{E}_1 e^{ik_x x} + \vec{E}_2 e^{-ik_x x}$

with a corresponding intensity of

(3.5) $$I = \frac{n}{2}\varepsilon_o c \vec{E}_o \cdot \vec{E}_o^* = \frac{n}{2}\varepsilon_o c\left[\left|\vec{E}_1\right|^2 + \left|\vec{E}_2\right|^2 + 2\vec{E}_1 \cdot \vec{E}_2^* \cos(2k_x x)\right]$$

or,

(3.6) $I = I_1 + I_2 + 2\Delta I \cos(2k_x x)$

where $\Delta I = \frac{n}{2}\varepsilon_o c \vec{E}_1 \cdot \vec{E}_2^*$. If $\vec{E}_1 = \vec{E}_2 \| \hat{y}$ (s-polarized beams), then

(3.7) $I = 2I_1(1 + \cos(qx))$.

This shows that the intensity varies sinusoidally in the interference region with an amplitude that varies from zero to four times the intensity of the individual beams. If the polarizations of the two beams are not both s-polarized, then the interference pattern is no longer described by Equation 3.7. If the beams are polarized perpendicular to each other, there will be no interference pattern.

If the excitation beams interact with the material in the interference region, a periodic excitation will form in that region. This excitation may be thermal, electronic, a concentration fluctuation, or any other property the light may directly or indirectly couple to. These material changes, which only occur in the bright fringes of the interference pattern, produce a corresponding spatial modulation of the index of refraction: a diffraction grating. The magnitude of this modulation may be as large as $\Delta n = 10^{-3}$, but changes on the order of 10^{-12} are detectable.

A third laser beam, the probe, is incident on the interference region at the Bragg angle calculated from Equation 3.1,

(3.8) $\theta_p = 2\sin^{-1}(\lambda_{probe}/(2\Lambda))$,

where λ_{probe} is the wavelength of the probe beam. If the index of refraction is modulated at λ_{probe}, part of the probe will be diffracted at an angle of θ_p from the incident beam. The intensity of the diffracted beam can then be used to measure the contrast of the grating.

The strength of the grating is usually measured by the diffraction efficiency,

(3.9) $\eta \equiv \frac{P_{diffracted}}{P_o}$,

where P_o and $P_{diffracted}$ are the powers of the incident and diffracted probe beams. For holographic volume gratings such as those created in FRS, η may be written as:

$$(3.10)\quad \eta = e^{\frac{-Kz}{\cos(\theta_p/2)}}\left(\sin^2\left(\frac{\pi\Delta n z}{\lambda_p\cos(\theta_p/2)}\right)+\sinh^2\left(\frac{\Delta K z}{4\cos(\theta_p/2)}\right)\right),$$

where K is the absorption coefficient at the probe wavelength λ_p, ΔK is the modulation of K, Δn is the modulation of the index of refraction, z is the thickness of the grating, and $\theta_p/2$ is the angle the probe makes to the grating.[6] If λ_p is chosen so that K = 0, then Δn can be determined from:

$$(3.11)\quad \Delta n = \frac{\lambda_p \cos(\theta_p/2)}{\pi z}\sin^{-1}\left(\sqrt{\eta}\right).$$

As an example, one of the weakest gratings produced in this study had P_o = 2.0 mW and $P_{diffracted} \approx$ 5.5 nW in a 3 mm thick sample at $\theta_p/2 = 7.83^\circ$. This implies an efficiency of $\eta = 2.8 \times 10^{-6}$ and $\Delta n = 1.1 \times 10^{-7}$. This analysis is not necessary to the study of diffusion using FRS, but it can be useful to understand the strength of the transient grating formed.

If the grating is thin (z is small, producing a grating that is more two dimensional than three dimensional) all orders of the diffraction pattern will be found, not just the order satisfying the Bragg condition. Thick gratings are advantageous because all the diffracted light is concentrated into one diffraction spot and therefore produces a larger signal.

For mass diffusion measurements in fluids, a tracer molecule is added to the liquid. The tracer molecule changes its optical properties when it absorbs light from the excitation beams. This excitation must have a lifetime long enough to allow the molecule

to diffuse a significant fraction of the grating wavelength before it decays. Because this diffusion time in liquids is quite long compared to typical electronic excitations, the tracer molecules used generally have metastable conformational states with lifetimes on the order of seconds. Therefore, when the excitation beams are removed, the periodic material excitation will decay through two processes: the intrinsic lifetime of the molecule, and its diffusion through the fluid. If the molecule does not diffuse, the transient diffraction grating will decay with a rate independent of the grating wavelength, Λ. If diffusion is occurring, molecules that had been excited in the bright fringes will move into regions that had not been excited. This motion will cause the grating to decay with a rate that is dependent on both the diffusion coefficient and the grating wavelength. Therefore, the diffusion coefficient may be extracted by monitoring the time dependence of the diffracted beam intensity.

The concentration of the species excited by a FRS measurement can described by the following 1-dimensional differential equation (when $\Lambda <<$ the width of the excitation beams):

$$(3.12)\quad \frac{\partial c_e(x,t)}{\partial t} = D\nabla^2 c_e(x,t) - \frac{c_e(x,t)}{\tau_1} + \alpha I(x,t)c_g(x,t) - \beta I(x,t)c_e(x,t)$$

where $c_e(x,t)$ ($c_g(x,t)$) is the concentration of the excited (ground state) species, D is the diffusion coefficient, τ_1 is the lifetime of the excited species, I(x,t) is the intensity distribution of the excitation pattern, and α (β) describes the rate at which the ground (excited) state is converted to the excited (ground) state by the incident light of the

excitation beams. This can be simplified if we assume $c_e(x,t) << c_g(x,t) \cong c(x,t)$, the initial concentration of the ground state molecule, and that $\beta << \alpha$. Then,

$$(3.13)\quad \frac{\partial c_e(x,t)}{\partial t} = D\nabla^2 c_e(x,t) - \frac{c_e(x,t)}{\tau_1} + \alpha I(x,t)c(x,t)$$

where, the intensity of the interference pattern for an excitation pulse that begins at t = 0 and ends at t = T is, from Equation 3.7:

$$(3.14)\quad I(x,t) = I_o\,(1 + \cos(qx))\,(H(t) - H(t-T)),$$

given that H(t-T) = 0 for t < T, and 1 for t > T.

After the excitation pulse (when I(x,t) = 0), the solution is:

$$(3.15)\quad c_e(x,t) = W\,e^{-t/\tau}\cos(qx)$$

where,

$$(3.16)\quad 1/\tau = Dq^2 + 1/\tau_1.$$

Therefore, the overall decay of the concentration pattern depends upon both the intrinsic lifetime of the excitation (τ_1) and the decay rate due to diffusion (Dq^2).

Due to the direct relationship between the concentration modulation and the amplitude of the diffracted beam ($\Delta n = \frac{dn}{dc}\Delta c$ and $\eta \propto \Delta n$ for small Δn), the amplitude of the diffracted beam decays at the same rate as the amplitude of the concentration grating. However, since the intensity of the beam is measured rather than its amplitude, the measured time dependence of the diffracted beam is:[7]

$$(3.17)\quad I_{diffracted}(t) = (Ae^{-t/\tau} + B)^2 + C^2,$$

where A is the amplitude of the diffracted electric field, B is the amplitude of light scattered from imperfections in the sample but remaining coherent with the diffracted beam, and C is the amplitude of the incoherently scattered background light.

The decay rate of the transient grating ($1/\tau$) is measured over a range of grating spacings ($2\pi/q$) and the resulting data fit with a function of the form of Equation (3.16) to extract both the diffusion coefficient and the lifetime of the excited state. A decay rate that does not depend quadratically on the grating wavector, indicates that anomalous diffusion is occurring. This is true because the statement $1/\tau \propto q^2$ is equivalent to the result found earlier for a random walker: $\langle r^2 \rangle \propto t$. Therefore, FRS may also be used to determine if classical diffusion is occurring on a length scale given by Λ.

In general, however, the situation is more complicated than the decay of a single grating. Because the excited state is formed from the ground state, the creation of a periodic concentration profile of excited molecules requires that there is a corresponding modulation of the ground state as well (Figure 3.3). In this case, there will be two decay rates, one for each grating. These will be: $1/\tau_e = D_e q^2 + 1/\tau_{le}$ and $1/\tau_g = D_g q^2 + 1/\tau_{lg}$. The intensity of the diffracted signal becomes:

$$(3.18)\quad I_{diffracted}(t) = (A_1 e^{-t/\tau e} + A_2 e^{-t/\tau g} + B)^2 + C^2$$

which can lead to a variety of non-monotonic decay curves depending upon the values of A_1, A_2, D_e, D_g, τ_{le}, and τ_{lg}.[8] If the excited state decays directly back to the ground state and not to a third state, relaxing molecules will reduce the modulation of both the excited state grating and the ground state grating. Therefore $\tau_{le} = \tau_{lg}$. If both species also diffuse at the same rate ($D_e = D_g$), then the time dependence of the diffracted beam will again

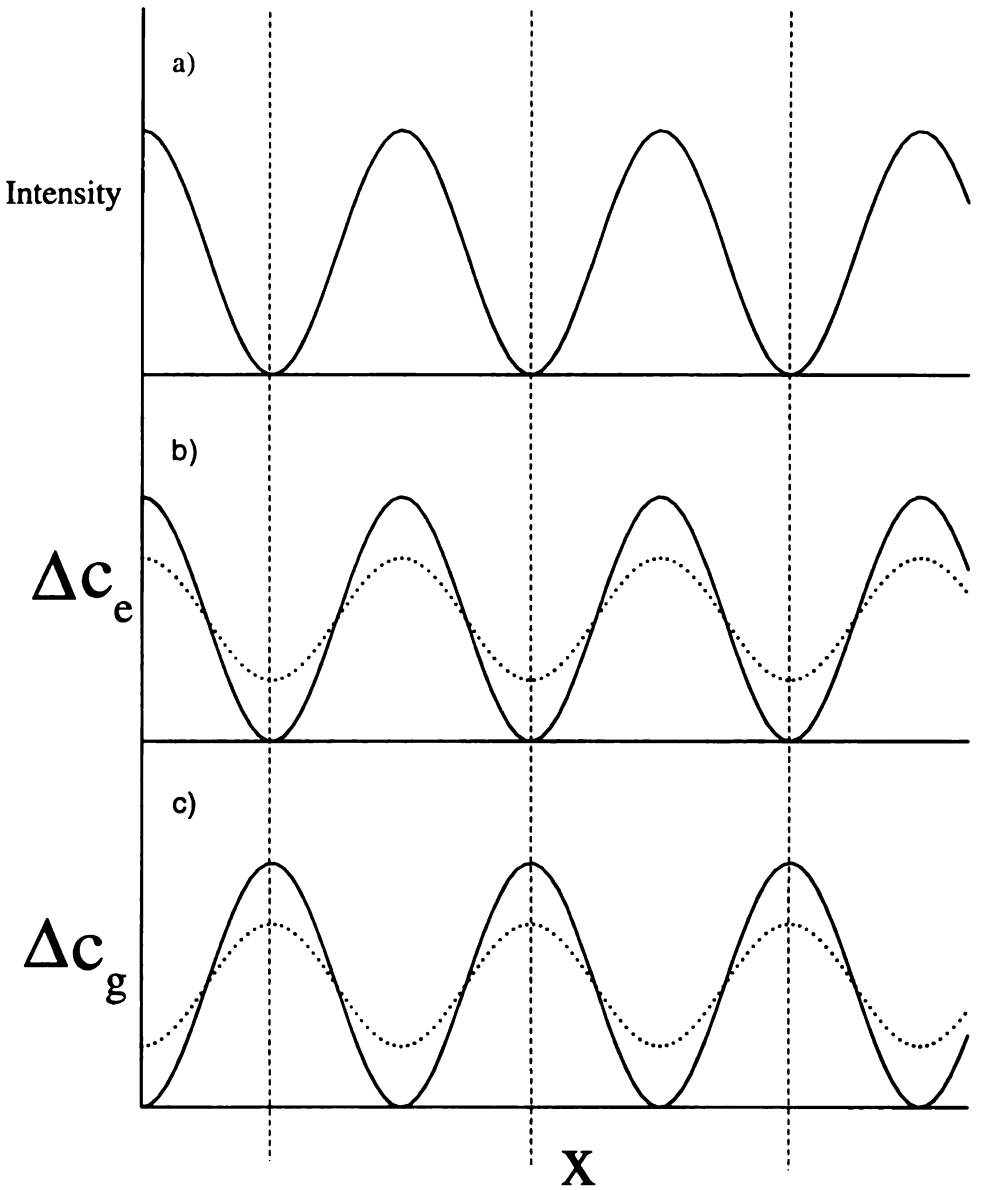

Figure 3.3: (a) Sinusoidal intensity profile of the interference pattern. (b) Corresponding profile of the change in concentration of the excited state species. (c) Profile of the change in concentration of the ground state species. The dotted lines illustrate the profiles after the interference pattern is removed and the concentration grating is decaying through diffusion.

be described by a single exponential, just as in the case of a single grating. If $D_e \neq D_g$ (for example, if one species is more attracted to binding sites on the walls of a pore), then the time dependence will no longer decay as a single exponential.[9] Because the analysis of such signals is difficult to interpret unambiguously,[10] usually only data that exhibit single exponential behavior are considered reliable. However, there are instances where the source of the nonexponential decay is well understood and where the non-exponential signals are sufficiently distinctive to allow analysis with Equation 3.18.

III. Experimental setup

The experimental setup used in most of the FRS experiments in this work is shown in Figure 3.4. The excitation laser is a Coherent Innova I-400-15 Ar^+ laser operating at 488 nm with an internal cavity etalon to produce a coherence length of at least several meters (when operated in ModeTrack mode to lase in only one cavity mode). The laser typically operates at 3.5 - 4.1 W of output power, corresponding to a tube current of 32.8 A. The diameter of the vertically polarized beam at the output of the laser is 2 mm, but widens to 3 mm by time it reaches the sample cell. The beam is attenuated by a sampling optic which reduces the power to ~100 mW. This is reduced further with a partially aluminized variable attenuator down to the final power of ~20 mW. The beam next passes into an assembly of optics making up the ferroelectric liquid crystal shutter. A vertically oriented Glan-laser polarizer first "cleans up" the polarization of the beam. The polarization is then rotated by a quartz half-wave waveplate, folowed by a rotation to either vertical or horizontal polarization by the Displaytech (PV 050 AC) liquid crystal rotator, which acts as a half-wave waveplate where the rotation depends upon the voltage

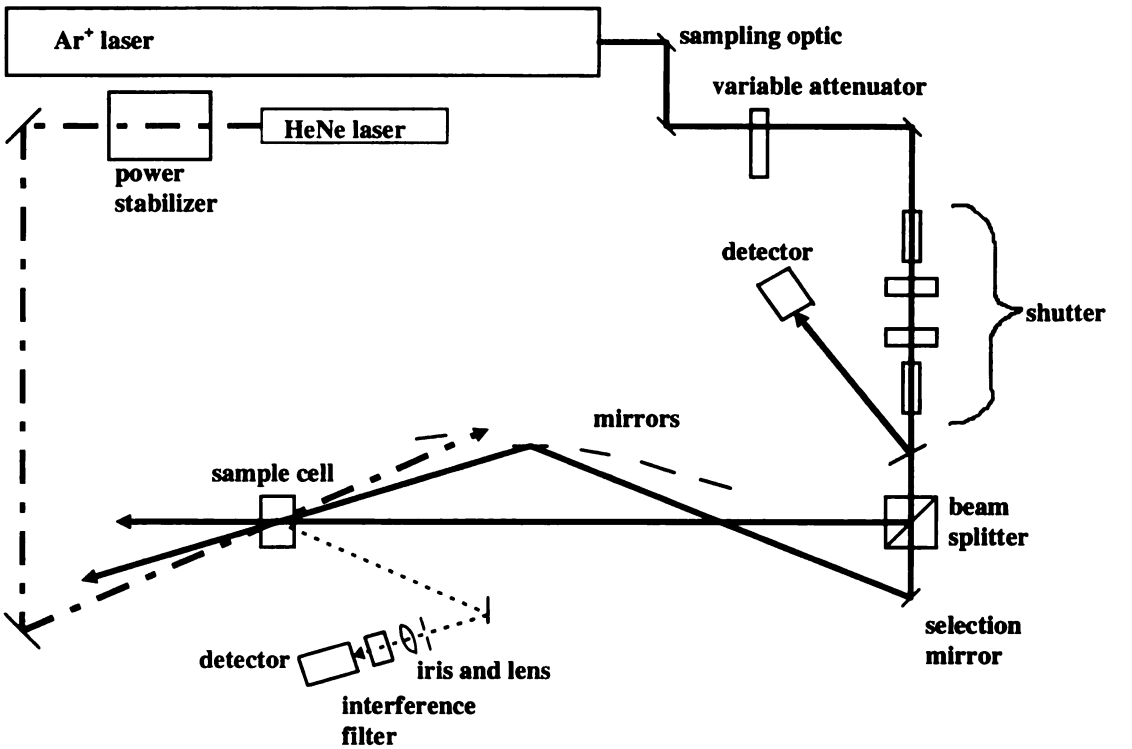

Figure 3.4: Experimental setup for the FRS measurements in this study. The distance between the beam splitter and the sample cell is 2.3 m.

applied across the liquid crystal. Finally, the beam exits through another Glan-laser polarizer which is oriented to pass only vertically polarized light. Depending upon the voltage applied to the bi-stable liquid crystal element, the excitation beam either passes through this final polarizer or is extinguished. This shutter has an extinction ratio of at least 1000:1 (the ratio of the power transmitted in the "open" state to that transmitted in the "closed" state) but is typically 5000 - 10000:1 with proper alignment and temperature stability. The advantage of this shutter over a mechanical shutter is its response speed. A mechanical shutter can open and close in 2-3 ms while the liquid crystal can switch state (90% open - 10% open) in 35 μs with much less variability from shot to shot.

The excitation beam next encounters a beam sampling optic which sends a portion of the beam to a photodiode used to trigger the oscilloscope that acquires the signal. The remaining beam is split by a cube beamsplitter--half is sent directly to the sample cell (excitation beam 1), and half is passed to the selection mirror (excitation beam 2). By rotating the selection mirror, beam 2 can be sent to one of the prealigned mirrors which direct it to intersect beam 1 inside the sample cell. The plane formed by the two intersecting excitation beams defines the direction of the interference pattern. Therefore, if the fringes of the interference pattern are to be vertical, the plane of the excitation beams must be parallel to the table surface.

As mentioned earlier, for the periodicity of the grating to be calculated simply, the normal vector to the sample cell face must bisect the angle between the excitation beams. So, to select the grating spacing, Λ, only the selection mirror and the sample cell need be rotated. To determine θ_{exc} and Λ, the distance between the excitation beams is measured at a known distance from the intersection point. For example, at the smallest grating wavelength, Λ = 1.225 μm, $\tan(\theta_{exc}) = \frac{16.7\text{cm}}{39.4\text{cm}}$, where the uncertainty in Λ is $\pm 2.0\%$ (from the uncertainty in the measured distances).

The probe beam is generated by a Uniphase 1137P 7 mW, linearly polarized HeNe laser. The beam power is controlled and stabilized externally by a Cambridge Research and Instrumentation power stabilizer to produce a beam of typically 2.0 - 3.0 mW that is stable to better than 0.5% over a period of several hours. The angle of incidence of the probe on the sample cell is changed by translating and rotating its own selection mirror. The approximate angle and location of the mirror is known by

calculating the Bragg angle from Λ, but is determined precisely by maximizing the intensity of the diffracted beam. The part of the beam transmitted through the cell is stopped in a beam block, while the diffracted portion is directed to the detector by a mirror. The probe beam is 2 mm in diameter when it is incident on the sample cell.

The detector assembly consists of an iris diaphragm, a lens, a 632.9 nm bandpass interference filter (with a 2.6 nm bandwidth, Oriel part number 52730), and a photodiode. The iris and the filter serve to block out all but the diffracted beam, while the lens is used to direct the light onto the photodiode so that the active area of the diode is filled (but not overfilled) by the beam. The peak transmittance of the interference filter is 50%, meaning that half the light at the center of the passed band is transmitted. The angular alignment of this filter is a significant source of error in the measurement of the absolute power of the diffracted beam because the transmittance of the interference filter is dependent on the angle of incidence of the beam. For a misalignment of 5 degrees, the central wavelength of this 2.6 nm bandwidth filter will shift by 0.3%, which can cause up to a 50% change in the transmitted intensity.[11] However, because FRS diffusion measurements only depend upon the rate of change of the diffracted signal and not its absolute magnitude, this effect is only important when trying to make a quantitative measurement of the diffraction efficiency. The detector is a Centronic OSD15-5T silicon photodiode with a 3.8 mm x 3.8 mm active area and a native response time of ~12 ns. The photocurrent produced by the diode flows through a 11.1 kΩ resistance to produce the measured voltage. The response of this detector is measured to be 4.1 V/mW at 633

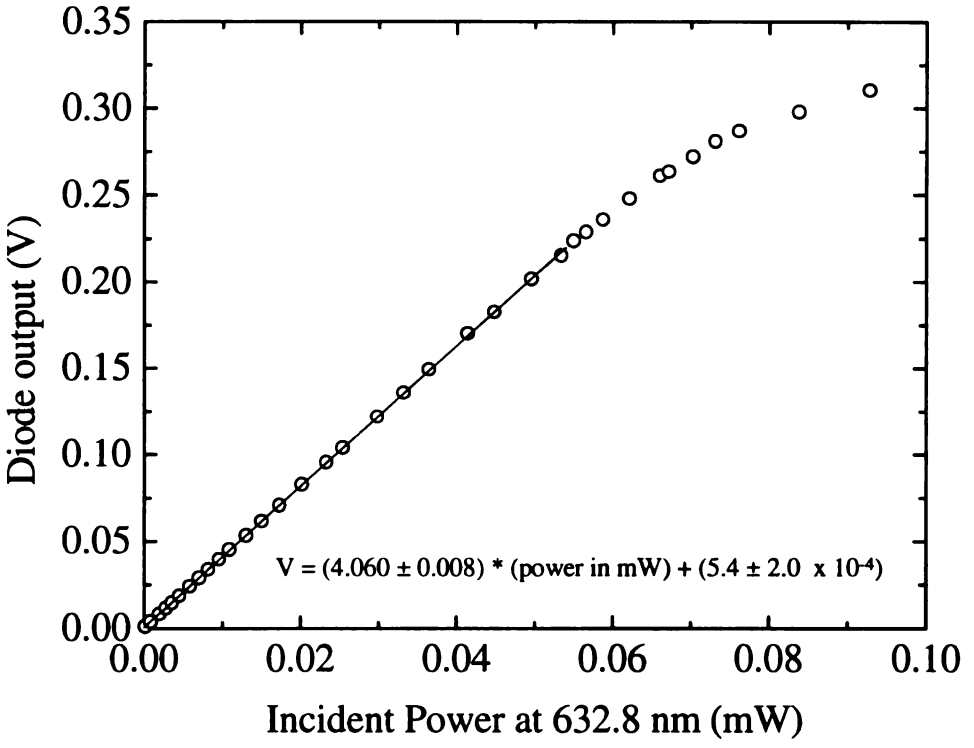

Figure 3.5: Response of the photodetector to 632.8 nm light. Power measured with Newport 1825-C meter and 818-SL detector.

nm (Figure 3.5). The linear response region of this detector extends to ~50 μW, while the diffracted signals in this experiment range from ~5 nW to ~ 2μW.

The sample cell (Figure 3.6) is a homemade copper cell designed for 27 mm outer diameter optical windows (Edmund Scientific #A2199). The sample and fluid are placed between two windows separated by a Viton o-ring whose thickness is chosen to be slightly larger than the sample. The glass windows are then pressed together in the copper cell--compressing the o-ring until the windows touch both sides of the sample and hold it in place. This is done so that no fluid is between the sample and the window

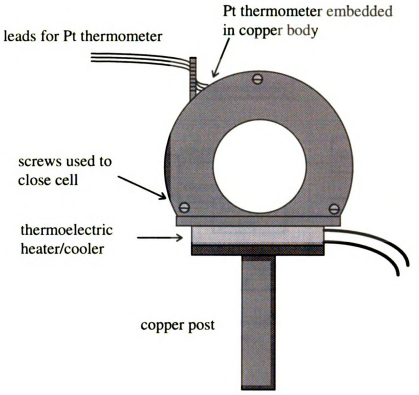

Figure 3.6: Schematic drawing of the sample cell holder. The body and post are made of copper separated by a thermoelectric heater/cooler used to control the temperature of the cell. When in use, the opening (which reveals the glass windows and the sample) is mostly covered with thin copper shim stock to reduce heat loss from the window faces. The heater is 1 inch square, and the opening in the cell body is 0.9 inches in diameter.

which could provide an additional diffusion signal. Soldered between the top of the cell (containing the windows and the sample) and the supporting post is a Melcor (CP1.0-71-06TT) thermoelectric heater/cooler used to control the temperature of the cell between 10 - 50 °C. An Omega Pt thermometer (#W2103) embedded in the top copper piece allows an Omega CN76000 temperature controller to maintain the temperature within ± 0.2°C.

Figure 3.7 is a schematic of the electronics used to control the experiment and acquire the data. The signal from the detector is amplified by a Stanford Research

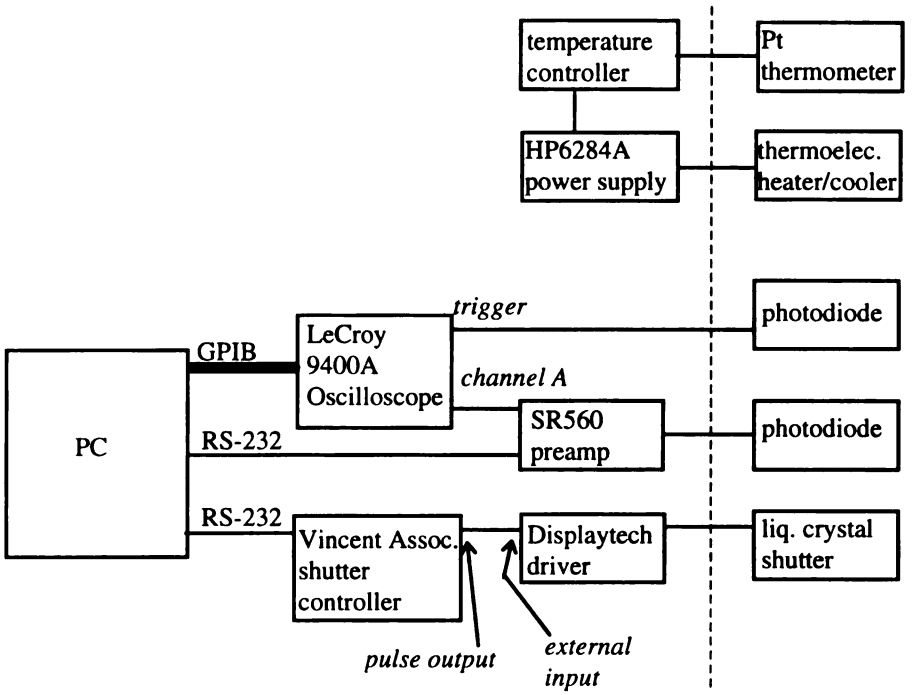

Figure 3.7: Schematic of the electronics used to control and monitor the FRS measurements. The dotted line separates equipment that is on the optical table (right hand side) from equipment on the overhead shelf. Italics indicates the name of the connection on the equipment.

Systems low noise preamplifier before being collected with a digital oscilloscope. The oscilloscope allowed many shots to be averaged together to improve the signal to noise ratio of the decay signal before it was transferred to the PC for storage and analysis. Except for the temperature controller and some of the features of the shutter controller, the entire experiment is controlled through a PC. (The control program and the file structure of the data files are shown in Appendix B)

IV. Detailed data acquisition procedure

After the sample has been loaded into the sample cell along with the fluid, and the lasers turned on and allowed to warm up for at least 20 minutes, the excitation beams are

aligned to intersect in the fluid next to the sample in the sample cell. The distance from the table top to each of the two excitation beams is measured to ensure that the beams are parallel to the table top, and at the same height. The excitation beams are aligned to overlap in the sample cell (there is enough scattering and fluorescence from the liquid to see the beam locations as they pass through the cell) by rotating the selection mirror that directs beam 2. The sample cell is then rotated so that the reflection of beam 1 off the front face retraces the path that beam 2 follows, and vice versa. This guarantees that the normal vector of the sample cell face bisects the angle between the excitation beams so that equation (3.1) may be used. The angle between beams 1 and 2 (θ) is determined by measuring the distance between the beams (x) at a known distance (y) along beam 1 from the point of intersection in the sample. The angle is then found from $\tan(\theta) = x/y$, and the grating spacing Λ is found from equation (3.1). The power in each beam is then measured just in front of the sample cell. This power is typically 6 - 7 mW in each beam, producing an intensity of ~ 8 mW/mm^2 at the peaks of the interference pattern (from $P = \frac{\pi w^2 I_o}{2}$ and Equation 3.7, where P is the power in a TEM_{00} beam, w is its radius, and I_o is the maximum intensity in the center of the beam).

The HeNe probe beam is set at the same height off the tabletop as the excitation beams, and aligned at approximately the Bragg angle by knowing Λ and λ_{probe}, and using equation (3.8). The final alignment is achieved with small adjustments to the mirror to maximize the power in the diffracted beam.

The detector assembly is then aligned so that the diffracted beam is sent to the photodiode through the iris diaphragm, lens, and interference filter.

Once the optics are all aligned, the delay between pulses of the excitation beams is adjusted to be longer than the time required for the grating to relax, and at least as long as the lifetime of the dye molecule. Normally, the delay is 10 to 20 seconds. The duration of the pulses is 20 ms to reduce heating of the liquid by the excitation beams. Next, the gain of the preamplifier is chosen to provide the maximum amplification without overloading it. This gain ranges from 5000 to 50,000 depending on the power in the diffracted beam. The appropriate timebase, vertical scale, and trigger time of the oscilloscope are then adjusted so the entire diffracted signal (before, during, and after the excitation pulse) is captured on the screen. Finally, the oscilloscope is allowed to average a number of these events (anywhere from 10 to 200 or more), to improve the signal to noise ratio. When the acquisition is stopped, the data is saved for later analysis.[12]

The next step is to measure the diffracted signal from within the sample. Therefore, the sample cell is translated so that the beams will intersect within it, rather than the fluid next to it. The excitation beams are then checked to verify that they overlap within the sample, the probe beam alignment is adjusted, if necessary, to maximize the diffracted signal, and the detector assembly realigned. The electronics are adjusted as before, and the diffracted signal from the sample is measured. Once this is complete, the angle between the excitation beams is changed and the process is repeated.

References

[1] H. Eichler, G. Salje, and H. Stahl, J. Appl. Phys. **44**, 5383 (1973).

[2] H.J. Eichler, P. Günter, and D.W. Pohl, *Laser-Induced Dynamic Gratings* (Springer-Verlag, Berlin, 1986).

[3] M.Terazima, K. Okamoto, and N. Hirota, J. Phys. Chem. **97**, 5188 (1993); J.A. Wesson *et al*, Macromolecules **17**, 782 (1984);T.P. Lodge, J.A. Lee, and T.S. Frick, J. Polym. Sci. B **28**, 2607 (1990).

[4] H. Hervet, W. Urbach, and F. Rondelez, J. Chem. Phys. **68**, 2725 (1978).

[5] D. Ehlich and H. Sillescu, Macromolecules **23**, 1600 (1990).

[6] H. Kogelnick, Bell Sys. Tech. J. **48**, 2909 (1969); H.J. Eichler, P. Günter, and D.W. Pohl, ibid., p. 104.

[7] L. Leger, H. Hervet, and F. Rondelez, Macromolecules **14**, 1732 (1981).

[8] H. Sillescu and D. Ehlich, in *Lasers in Polymer Science and Technology: Applications*, edited by Fouassier and Rabek (CRC Press, 1990).

[9] J.L. Xia and C.H. Wang, J. Chem. Phys. **88**, 5211 (1988); J.A. Wesson *et al*, Macromolecules **17**, 782 (1984).

[10] S. Park *et al*, J. Phys. Chem. **95**, 7121 (1991); D.R. Spiegel, M.B. Sprinkle, and T. Chang, J. Chem. Phys. **104**, 4920 (1996), S. Park, H. Yu, and T. Chang, Macromolecules **26**, 3086 (1993).

[11] For light at an angle of incidence of θ, this filter's center wavelength is $\lambda_\theta = \lambda_o\sqrt{1-0.690\sin^2(\theta)}$, where λ_o= 632.9 nm, the center wavelength at normal incidence. Oriel Corporation, Optics and Filters Catalog, p. 2-31 to 2-37.

[12] Microcal Origin v. 4.1 is used to fit the data. The nonlinear least squares curve fitting routine uses the Levenberg-Marquardt algorithm to find the fit that produces the smallest χ^2 value.

Chapter 4

MATERIALS

I. Introduction

Finding porous materials is not difficult. More materials absorb liquids or gases than are impervious to them. Everything from wood, biological cells, plastics, concrete, stone, ceramics, and even some forms of metals are porous. The transport of fluids through each of these materials is crucial to their formation, their technological usefulness, or (in the case of living porous materials) their existence. Restricting our focus to materials that are manufactured for their porous nature, we still find a tremendous variety of forms: sintered metals, disordered porous glasses, crystalline media like zeolites,[1] layered materials,[2] and self-assembled materials.[3] These manufactured materials are of great interest to the catalysis and separation (sieving) community where the ability to design a material for specific processes is crucial.

II. Porous silica

II a. Types of porous silica

This work focuses on fluid diffusion in porous silica, chosen partly because it is transparent to visible light, and partly because of the wide range of ways that exist to prepare it. The first commercial porous glass was Vycor 7930,[4] a borosilicate glass that is heat treated to phase separate it into two interpenetrating boron-rich and silica-rich networks. The boron rich phase is then dissolved in acid, leaving behind a silica rich porous glass with a very narrow pore size distribution (20 - 30 Å pore radius). Glasses may also be produced through the gelation of colloidal silica sols[5] or aggregates of flame-

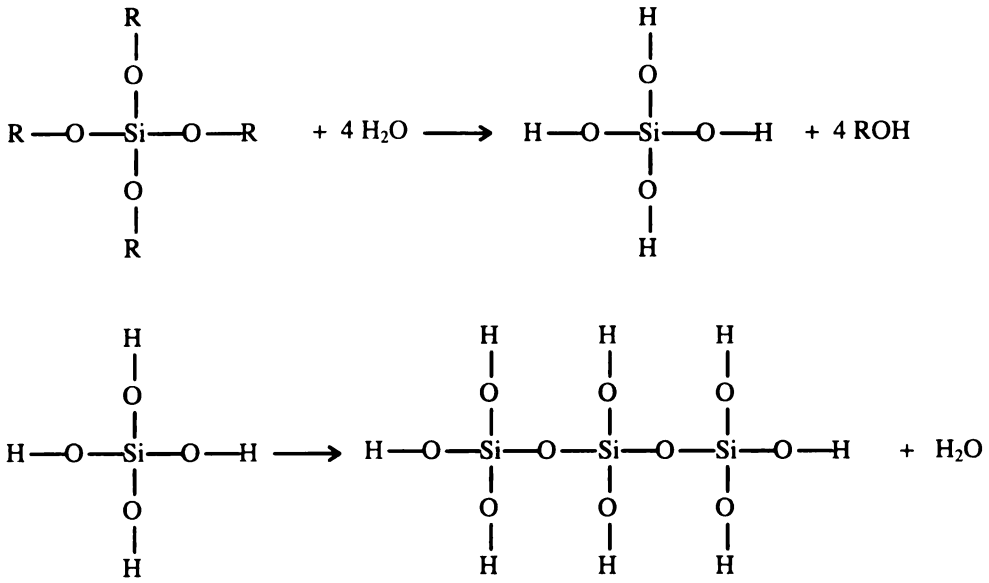

Figure 4.1: The sol-gel process showing TEOS reacting with water to form silanol, which then reacts to form the silica network.

hydrolyzed silica.[6] The most common way of making porous silica today is through the polymerization of hydrolyzed metal alkoxides such as tetraethylorthosilicate (TEOS) in an alcohol/water mixture. This sol-gel process is shown in Figure 4.1: the TEOS reacts with water to produce silanol and an organic alcohol (here, ethanol). The silanol molecules react with each other, releasing water and producing a network of silica. The network formed is not a regular lattice as the bonds form during random interactions between molecules. This network is said to have gelled once the network spans the entire body of the container (therefore, the gel point is a percolation threshold[7]). In practice, this point is defined as the moment when tilting the sample produces no flow.

The water and alcohol evolved in the gelling process must be removed from the network in order for the pore structure to be accessed. This drying step is the most critical phase of the process. As the liquid/vapor interface progresses into the porous

material, the surface tension on the meniscus produces large stresses on the network.[8] These stresses, which are greatest in small pores, can easily crack the gel. There are several ways to produce uncracked dried gels:[9] dry the gel under tightly controlled pressure and humidity to produce highly porous materials such as aerogel,[10] add a surfactant to lower the surface energy at the drying interface, remove the small pores, dry the gel under very high humidity (to increase the gelling time and allow the network to respond to the stresses), or produce highly homogeneous gels that allow the stress to be balanced over the entire network. Once the network is successfully dried, it may be heated to remove the remaining adsorbed water, to modify the surface chemistry, or to reduce the porosity.

II b. The effect of heat on silica

The surface of silica in air is covered by one or more layers of adsorbed water (water hydrogen bonded to the hydroxyl groups on the surface). As silica is heated, the surface passes through several regimes of dehydration (Table 4.1, Figure 4.2) eventually reaching a hydrophobic state and, if heated further, shrinking to become fully dense silica.

Table 4.1: Character of the silica surface as a function of the temperature.

Temperature (C)	surface character
< 170	hydrated: bound water and hydroxyl groups
170 - 400	reversible dehydration: no more water, vicinal groups begin condensing
400 - 800	irreversible dehydration: shrinkage closes off pores
> 800	only isolated hydroxyl groups exist--hydrophobic surface
> 850	isolated hydroxyl groups react--closing network
1000 - 1700	densification

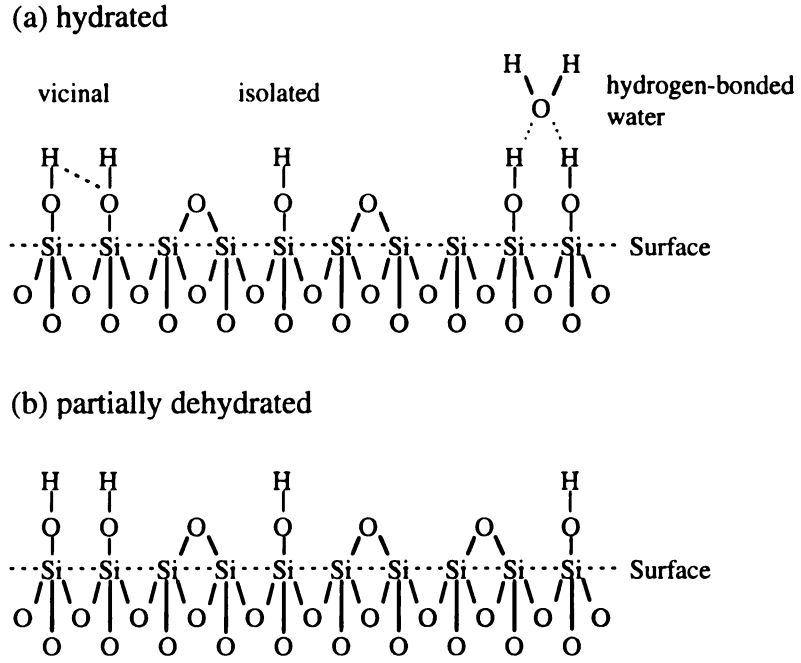

Figure 4.2: Schematic of the (a) hydrated and (b) dehydrated silica surface, showing the types of hyroxyl groups and bound water that can form. (After R.K. Iler, *The Chemistry of Silica* (John Wiley and Sons, New York, 1979) and K.K. Unger, *Porous Silica* (Elsevier, Amsterdam, 1979).).

Figure 4.2a schematically shows the surface structures on a hydrated silica surface: vicinal hydroxyl groups, isolated hydroxyl groups, and hydrogen bonded water. As the temperature is raised above 170°C, the adsorbed water is removed and vicinal hydroxyl groups begin condensing to form siloxane and water. Up to ~400°C, the dehydration is fully reversible and exposure to water will produce a hydrated surface equivalent to the original surface. Above ~400°C, shrinking of the network begins to close off pores. By ~800°C only isolated hydroxyl groups exist on the surface, and at ~850°C the motion of silicon atoms at the surface is significant enough to allow isolated hydroxyl groups to

react and begin densifying the network. The silica will fully densify (i.e. lose its porosity and reach the density of fused silica, 2.2 g/cm^3) at temperatures greater than 1000°C.[11]

This heating process to transform a wet silica gel into a fully dense silica at relatively low temperatures is a significant advance in the manufacture of preformed silica objects.[12] Previously, very pure fused silica could only be produced in a high temperature (> 1600°C) process. With sol-gel processes, glass can be made in pre-shaped molds (which significantly reduces the time required for grinding and polishing)--but only if the optic survives the drying step without cracking. Another difficulty in glass formation is the transformation of silica to a crystalline form before it fully densifies. It is found that the presence of alkali ions in the network promotes this crystallization at temperatures as low as 700°C. Lithium causes quartz to form, while sodium produces cristobalite.[13] This is a concern in the production of glasses from charge-stabilized colloids where alkali counter ions from the suspension are incorporated into the network upon gelation, and means that the creation of a hydrophobic amorphous silica surface through heat treatment is impossible to achieve.

III. Characterization of porous silica

III a. Properties of porous silica

Understanding the pore structure in porous materials is crucial to understanding the transport processes that take place within them. Therefore, the determination of the pore structure is of great importance, although it is a task that has proven very difficult to accurately accomplish. A number of techniques are employed to characterize the structure--each with its own strengths and weaknesses.

The properties of interest of a porous material are the surface area, pore volume, average pore size, pore size distribution, and connectivity. The surface area of a porous material is all the surface that is accessible from the exterior, including the surface area of the pores. A large surface area is advantageous for catalysts, because the chemical reactions take place on the surface and a larger surface area allows more reactions to occur simultaneously. The pore volume is the volume of the material not occupied by the rigid network. The porosity (the ratio of the pore volume to the total sample volume) is the characteristic most often reported as it is easily measured by either comparing the weight of the material with empty pores to the weight with the pores full of a liquid of known density or by measuring the volume of liquid displaced by the addition of the material. Note that with these measurements, isolated pores are not detected. The porosity characterizes how much of the material is empty and how much is solid. The pore size distribution is, as the name implies, the distribution of the pore sizes throughout the material. The distribution is defined by the amount of the pore volume that results from pores of a given size. Therefore, a narrow pore distribution implies that most of the available pore volume occurs in pores of nearly the same size. The connectivity of the pore network is the average number of passages that lead out of one pore to a neighboring pores (e.g. a perfect cubic pore network would have a connectivity of 6). The connectivity is perhaps the most difficult of all the parameters to determine[14] as it cannot easily be probed externally.

III b. Common techniques for characterizing porous materials:

The most straightforward technique for determining these properties[15] is to repeatedly make cross sections of the material. After each slice the amount of the exposed area that is solid and the amount that is empty is measured. This has several obvious disadvantages including the destruction of the sample and the large amount of time it takes to make the measurement. Nevertheless, variations of this technique are used--particularly for materials with nanometer-sized features, where the sample is thinned down for measurement in a transmission electron microscope.

A very powerful technique that has been applied to the analysis of the structure of porous rocks[16] is that of X-ray microtomography, where (just like in medical CT scans) a three dimensional image of the sample interior is built up by analyzing the absorption of X-rays as they pass through a sheet of the sample. While it is a useful nondestructive technique, it is limited to a resolution of about 1 micron and requires the use of synchrotron X-ray sources.

Small angle X-ray scattering (SAXS) and small angle neutron scattering (SANS) have been used successfully to determine average properties of porous materials[17] such as the correlation length of the network, which can be related to the average pore size. Structural properties on the order of a few Angstroms to about 2000 Å may be probed with these techniques, and they have been useful in the determination of the fractal nature of some porous networks. However, SAXS can make no determination of the pore volume or surface area of a sample.

Nuclear magnetic resonance imaging (MRI) can also be used to image the internal pore structure of a porous material[18] as well as measure the motion of fluids within the pores.[19] MRI is limited in spatial resolution to fractions of a millimeter and so is (like X-ray tomography) not useful in the characterization of microporous materials.

One of the oldest techniques for the determination of the pore size distribution is mercury intrusion.[20] Because mercury does not wet the pore walls, it must be forced into the pores with externally applied pressure. At 1 atmosphere, mercury will fill pores connected to the surface if their pore radius is greater than 7 μm. Filling pores of 100 Å and 20 Å radius requires pressures of 700 atm. and 3500 atm., respectively.[21] The measurement is very simple: a known quantity of mercury is brought into contact with the surface of the material and the pressure increased to fill the pores. As the pores fill, the amount of mercury removed from the "bath" at each pressure step is measured to determine the uptake curve. In order to relate this to the pore size, a model of the pore structure must be assumed.[22] Normally, a bundled tube model is used, where the diameter of each tube is constant along its length, but each tube may have a different diameter. This is the largest source of error in the determination of the pore size distribution--if the pores do not have a constant diameter, a large pore in the interior will fill only after the smaller pores between it and the surface do. This means that the amount of mercury taken up at a given pressure does not correspond to the total volume occupied by pores of only one size. Therefore, the measured distribution really gives information about only the smallest pores that the mercury passes through, as they are the limiting connections. Mercury intrusion works best for large pore samples, but is capable of

measuring distributions below 40 Å. This technique has two main drawbacks: the use of a toxic liquid (that may remain in the pores after the measurement), and the use of high pressure which may destroy the network of pores.

III c. Nitrogen adsorption

By far the most common method for determining the internal structure of a porous material is the isotherm analysis of the adsorption of a gas, typically nitrogen.[23] This condensation technique is capable of determining the pore volume, specific surface area (surface area per gram of adsorbent), and pore size distribution of a material without subjecting it to high pressures or contaminating it. It does not, however, produce a microscopic image of the pores and its conclusions about the pore distribution are affected by the model used to represent the pore shape. Therefore, while these measurements are highly useful in providing an understanding of the pore structure, they are not without serious ambiguities.

Nitrogen adsorption measurements are made by placing the sample (the adsorbent) into a cell of known volume that is cooled to the temperature of liquid nitrogen.[24] Attached to this cell through a valve is another chamber of known volume (the dosing volume) in which the pressure is monitored. After evacuating both chambers, and closing off the sample cell, the dosing volume is filled with a known quantity of nitrogen gas. The valve between the chambers is then opened, allowing the gas to condense inside the pores of the sample. The amount that condenses is determined from the change in the pressure after the system has equilibrated. This cycle is repeated until the saturation pressure (p_o) has been reached and all the pores are filled. The procedure is

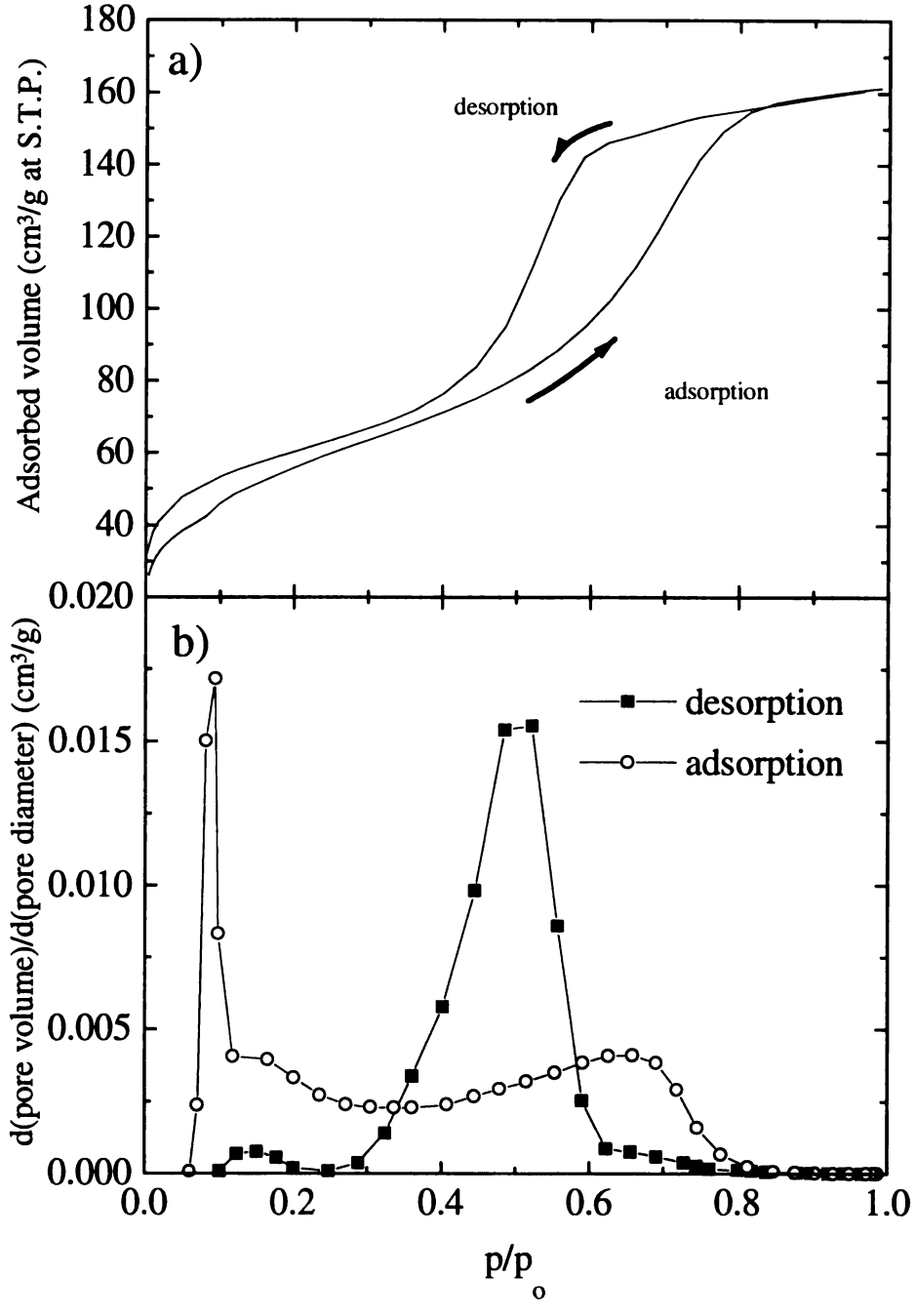

Figure 4.3: (a) Nitrogen adsorption and desorption isotherms for Vycor porous glass. (b) The pore size distributions calculated from (a).

then reversed to measure the amount desorbed as the pressure is reduced (Figure 4.3a).

Once the isotherms (the total amount of gas condensed in the sample at each pressure step) are measured, they are analyzed to determine the surface area, pore volume, and pore distribution. The surface area is typically determined through a method first described by Brunauer, Emmett, and Teller:[25] the BET model. The BET surface area is found from the amount of gas adsorbed on the surface after the first monolayer has formed and before any pores are completely filled. The model assumes that all the adsorption sites are equivalent (that no one site is favored), that no interaction exists between molecules adsorbed in the same layer (i.e. an adsorbed molecule interacts only with the molecules directly below it and directly above it), and that an infinite number of layers will exist on the surface when $p = p_o$. These are significant assumptions that are generally violated in any adsorption experiment. The result of the model is the BET equation relating the mass of the adsorbed gas to the relative pressure:

$$\frac{p}{x(p_o - p)} = \frac{1}{x_m c} + \frac{c-1}{x_m c}\frac{p}{p_o}, \qquad (4.1)$$

where p is the pressure of the gas, p_o is the saturation vapor pressure, x is the ratio of the mass of adsorbed gas at p to the total mass of the adsorbent, x_m is the ratio of the mass of one monolayer of adsorbed gas to the mass of the adsorbent, and c is a constant. Therefore, if the isotherm data are plotted as $\frac{p}{x(p_o - p)}$ vs. $\frac{p}{p_o}$, a straight line should be found and x_m and c can then be determined from the slope (s) and intercept (i) of that line through the relations: $x_m = 1/(s+i)$ and $c=(s+i)/i$. This linear region in the adsorption isotherm is typically in the range $0.05 < p/p_o < 0.35$ for silica. The specific surface area

(S, the surface area per gram of adsorbent) of the sample is then determined from the mass adsorbed in the first monolayer by:

$$(4.2) \quad S = \frac{x_m}{M} N_A A_m,$$

where M is the molecular weight of the adsorbate, N_A is Avogadro's number, and A_m is the area covered by one adsorbate molecule (= 16.2 $Å^2$ for nitrogen).

The pore volume is easily found from nitrogen adsorption because at the saturation pressure, the pores are completely filled with a known mass of liquid nitrogen. However, just as in mercury intrusion experiments, the pore distribution cannot be determined without making a model of the pore structure. At a pressure $p < p_o$, the pores are partly filled by liquid, with nitrogen condensing in the smallest pores first. It can be shown that a capillary pore will fill according to:[26]

$$(4.3) \quad \frac{dv}{dS} = -\frac{V\gamma}{RT\ln(p/p_o)}\cos(\phi)$$

where v is the volume of the capillary, S is the specific surface area of the capillary walls, V is the molar volume of the liquid, g is the surface tension of the liquid, and ϕ is the contact angle between the walls and the liquid. For liquid nitrogen, V = 34.6 cm^3/mole and γ = 8.85 dyne/cm. Because of the difficulty in determining the contact angle in a porous material, the fluid is assumed to wet the pore walls ($\phi = 0^o$).

The relationship describing the pore size at which condensation occurs for a given pressure must arise from a physical model of the pore geometry. Because the true pore geometry is nearly always unknown, the pores are frequently modeled as being perfectly

cylindrical. In that case, the radius of the pore (the Kelvin radius, r_k) where condensation occurs at pressure p is:

$$(4.4) \quad \frac{r_k}{2} = -\frac{V\gamma}{RT\ln(p/p_o)}\cos(\phi).$$

Given this (and correcting for the amount of liquid being adsorbed on the pore walls at the same pressure), the sorption isotherms can be converted into a pore distribution by calculating the amount of liquid nitrogen added to the pores at each pressure step[27]--which is essentially taking the derivative of the isotherm. Figure 4.3b shows the pore distributions produced from the adsorption and desorption isotherms shown in Figure 4.3a.

This procedure is complicated by the hysteresis observed between the adsorption and desorption isotherms in porous media[28] (Figure 4.3a). The hysteresis is a result of pores which vary in size along their length. As p/p_o increases during the adsorption phase, vapor will condense in the narrower sections of the pore first--followed by the wider regions. However, during the desorption, wide areas which are separated from the surface by a narrow region must wait until that narrow region empties (at a lower value of p/p_o) before it can vaporize (similar to the situation in mercury intrusion experiments). This will cause the measured adsorbed volume at a given p/p_o to be larger in the desorption isotherm than the adsorption isotherm. This discrepancy produces two very different calculated pore distributions (Figure 4.3b): a narrow distribution that provides more information about the size of the "flow-limiting" pore necks (desorption), and a broader distribution that some view as a more accurate representation of the true distribution of pores (adsorption).

This hysteresis in the isotherms vividly shows the problems of using a cylindrical pore model in the determination of the pore radius. If the pores were really just straight cylinders, there would be no hysteresis in the isotherms. In reality, very few porous materials have cylindrical pores, and certainly disordered porous materials like porous glasses do not fit the model. For this reason, the pore radii determined from the isotherm analysis cannot be accepted without question. The shape of the hysteresis curves have been used as a way to determine the geometry of the pores,[29] although it is not a direct measure of the pore shape. The Gelsil samples used in this work all have hysteresis curves that classify them as being made of cylindrical pores.

Due to these difficulties, an estimate of the average pore radius is used that is based on the measured surface area and pore volume (two quantities that are relatively well known).[30] This estimate, known as the Wheeler radius or the hydraulic radius, is:

$$(4.5) \quad R_w = 2\frac{V_p}{S_{BET}},$$

where V_p and S_{BET} are the pore volume per gram adsorbent and the BET surface area per gram adsorbent, respectively. This estimate can vary by as much as 20% from the peak value of the pore distribution determined from the isotherms.[31] However, the Wheeler radius is simple to determine, is based on the same assumption of cylindrical pores, and has been found useful in comparing materials of similar compositions.[32] For these reasons, R_w is frequently used to characterize the pore size--particularly in conjunction with isotherm analysis to gauge the width of the distribution, and the possible geometry of the pores.

IV. The manufacture and properties of Gelsil

The main emphasis of this study is focused on fluid diffusion in a set of commercial sol-gel glasses made by GelTech, Inc.[33] These porous glasses are a byproduct of the development of fully densified sol-gel glasses for the manufacture of pre-shaped optical elements.[34] This process requires forming gels that do not crack upon drying or heating. In these materials, this is achieved with the addition of a "drying control chemical additive"[35] which serves as a surfactant to reduce the capillary stresses found at the liquid/vapor interface during drying. One effect of these additives is to produce extremely narrow pore distributions during the gelation phase, which also helps diminish the drying stresses caused by unequal evaporation rates from pores of different sizes. After drying, these porous optics are heated to drive off the bound water and, if the heating is stopped at ~650°C, a porous glass of small (< 100 Å radius) and very uniform pore size is recovered. The drying control additive is chosen to also be easily removed from the glass during the heating process and so not contaminate the end product. Due to their small pores and narrow pore size distribution, these porous glasses (of porosity > 0.4) are optically transparent. If the glass is heated up to 1150°C, it will shrink to fully dense silica. One thing to note is that the porosity of these glasses is much larger than the porosities of a Vycor-like glass of the same pore size. This means that in the sol-gel glasses, the walls of the rigid network are thinner or there are more connections between the pores.

According to the manufacturer, the surfaces of the porous glass (Gelsil) is that of a dehydrated silica surface--siloxane bonds with both vicinal and isolated hydroxyl groups.

Table 4.2: Properties of the Gelsil samples as determined from nitrogen adsorption performed by Geltech, Inc.(GT) and Porous Materials, Inc. (PMI). R_W is the Wheeler average pore radius, R_{PV} and R_{SA} are the median pore radii as determined from the cumulative pore volume and surface area, respectively.

Sample	R_w (GT) (Å)	R_w (PMI) (Å)	R_{PV} (desorp.) (Å)	R_{PV} (adsorp.) (Å)	R_{SA} (desorp.) (Å)	R_{SA} (adsorp.) (Å)	Pore Volume (GT) (cm^3/g)	Pore Volume (PMI) (cm^3/g)	Surface Area (GT) (m^2/g)	Surface Area (PMI) (m^2/g)	Porosity (GT)	Porosity (PMI)
A200	**91.5**	**96.9**	71.9 ± 22.4	69.2 ± 24.6	137.6 ± 36.5	65.3 ± 14.3	1.21	1.19	264.1	245.5	**0.727**	**0.724**
A075	**35.5**	**38.6**	28.0 ± 7.1	27.6 ± 6.9	38.1 ± 12.9	30.0 ± 9.8	0.93	0.87	523.5	449.6	**0.671**	**0.656**
A050	**27.7**	**32.7**	21.7 ± 5.6	21.4 ± 4.7	30.4 ± 10.9	24.2 ± 7.6	0.74	0.82	538.0	501.5	**0.621**	**0.643**
"A075"	**16.4**	**18.4**	17.6 ± 3.8	17.3 ± 3.3	18.5 ± 5.5	16.4 ± 4.4	0.49	0.49	598.9	532.2	**0.519**	**0.518**
A025	**14.0**	**16.5**	17.3 ± 4.6	16.9 ± 3.6	17.7 ± 5.6	15.3 ± 4.0	0.39	0.44	559.7	530.5	**0.463**	**0.491**

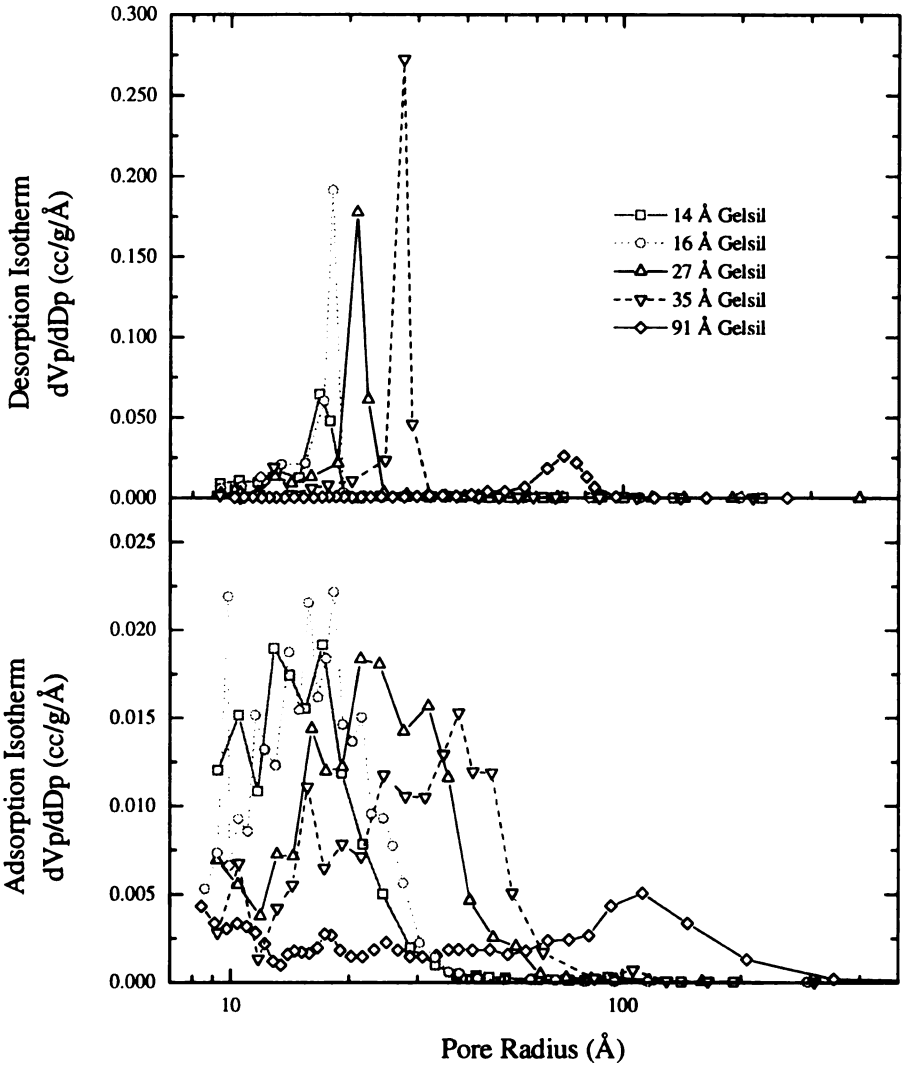

Figure 4.4: Top: Pore size distributions of the Gelsil porous silica samples calculated from the desorption isotherms. Bottom: Pore size distributions of the Gelsil porous silica samples calculated from the adsorption isotherms. Note the discrepancy between the adsorption and desorption distributions, and with the nominal average pore radius.

The pores are characterized by nitrogen adsorption and the average pore radius (calculated by R_w) is reported. By varying the initial concentrations in the sol and changing the temperature treatment, the average pore radius can be varied from ~15 - 100Å. The Gelsil was used as it was received from the manufacturer with no additional heat treatments applied.

To verify the manufacturer's values for the pore size and porosities of these silicas, the samples underwent additional nitrogen adsorption analysis by a third party.[36] Even though the measurements were made approximately nine months after the samples were made and first analyzed, the agreement (Table 4.2) between the results is quite good. Analysis of the adsorption and desorption isotherms (Figure 4.4) confirms the narrow pore distributions claimed by the manufacturer and indicates the pores are roughly cylindrical (based on the shape of the hysteresis curves). As discussed earlier, while these distributions provide some information about the pore size, they are not a true representation of the pore geometry. In order to gain some additional insight into the structure, preliminary analysis with Scanning Electron Microscopy (SEM) and Atomic Force Microscopy (AFM) has been carried out.

It should be noted that the adsorption analysis performed by the manufacturer was carried out on a larger amount of the material than was available for the later analysis. The accuracy of the measurements increase with a larger amount of adsorbent because of the larger total pore volume. This, and the fact that the manufacturer's analysis was carried out shortly before the materials were used in the diffusion studies gives us greater

confidence in those results. The additional analysis was performed to verify the manufacturer's results and gain some knowledge of the pore distribution.

The SEM analysis was carried out by Dr. Baokang Bi on a Hitachi S-4700 microscope on the uncoated Gelsil surface. Figure 4.5 shows a 200 x 200 nm image of the 2.8 nm average pore radius Gelsil glass, while Figure 4.6 shows a 600 x 450 nm image of the 9.1 nm pore radius glass. Here, the bright regions correspond to the protruding silica, and the dark regions to the space between them. Assuming that the pores exist at the boundaries between the particles in these images, the feature sizes in both images are consistent with the pore radii obtained from nitrogen adsorption.

The AFM analysis was performed on a Digital Instruments Dimension 3100 SPM operating in Tapping Mode. Figure 4.7 shows the surfaces of the 1.4, 2.8, and 9.1 nm pore radius samples. All show colloidal structures as seen in the SEM images. It is important to realize that in all probe microscopies, the topographic image obtained is a convolution of the surface features with the shape of the probing tip. Therefore, small lateral features on rough surfaces can appear larger than they actually are.

Both SEM and AFM indicate the colloidal-like growth that is expected in sol-gel glasses[37] where the colloidal gel particles grow first, then combine to form the continuous network of the glass. The pores in these samples may occur in the gaps between the colloidal particles, similar to the "Swiss-cheese" model discussed in Chapter 2. In Chapter 5, we will compare predictions of the Swiss-cheese model to the results of diffusion in these Gelsil samples.

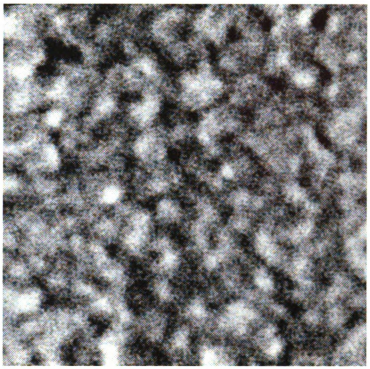

Figure 4.5: SEM image of the uncoated surface of the 28 Å pore radius Gelsil sample. The field of view is 2000 Å x 2000 Å.

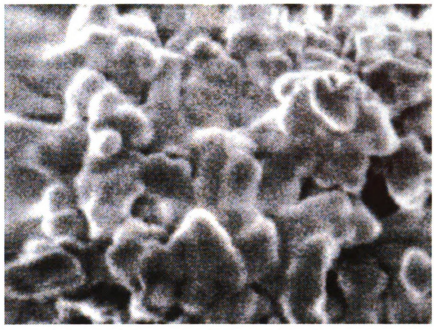

Figure 4.6: SEM image of the uncoated surface of the 91 Å pore radius Gelsil sample. The field of view is 6000 Å x 4500 Å

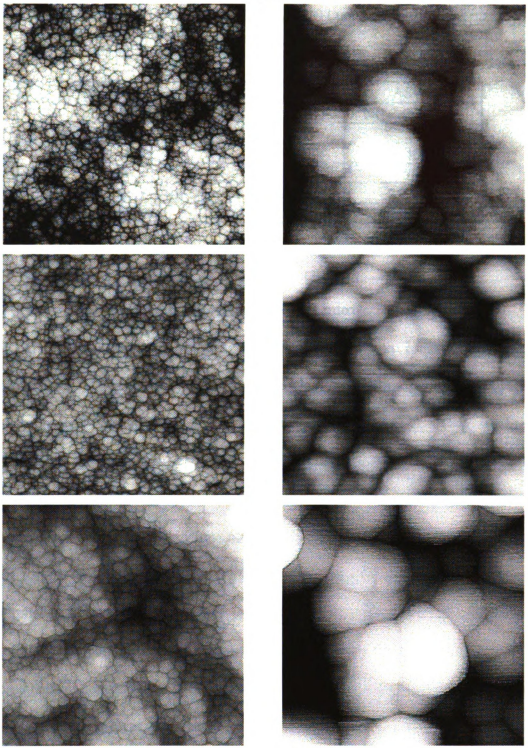

Figure 4.7: AFM topographic images of the surfaces of the 1.4, 2.8, and 9.1 nm pore radius Gelsil samples (top to bottom). The images in the left column and right column are $(1\ \mu m)^2$ and $(200\ nm)^2$, respectively.

Table 4.3: Properties of the HS-40 and AS-40 Ludox colloidal silica suspensions.

	HS-40	AS-40
counter ion	Na^+ (NaOH)	NH_4^+ (NH_4OH)
particle diameter (nm)	12	22
wt% silica	40	40
pH	9.7	9.1
specific surface area (m^2/g)	220	135
gelled with	NaCl	NH_4Cl

V. The manufacture and properties of gelled Ludox

The gelled Ludox samples were made by the author from Ludox AS-40 and HS-40 colloidal silica[38] (Table 4.3). The silica particles are kept in a suspension of high pH water to produce a negative charge on the particle surface, ($Si\text{-}O\text{-}H + O\text{-}H^- \rightarrow Si\text{-}O^- + H_2O$) to cause the spheres to repel when they are close, thereby preventing aggregation and settling. The positively charged counter ions surrounding each particle screen the surface charges and eliminate any long range coulomb interactions between particles. For Ludox to gel, the particles must be allowed to interact with each other. This may be accomplished in several ways: one can reduce the surface charge (by reducing the pH of the solution), increase the concentration of the silica (to force the spheres closer together), increase the salt concentration (Cl^- ions force the positively charged counter ions closer to the surface of the spheres, reducing the length over which the repelling force exists), or increase the temperature (to increase the number of interactions between particles). When the particles interact, the spheres can stick together through hydrogen bonds formed by the surface hydroxyl groups and adsorbed water. This bonding becomes

permanent with the formation of Si-O-Si bonds between particles. Because hydroxyl ions are a catalyst for Si-O-Si bond formation, as well as the cause of the negative surface charge on the spheres, their concentration strongly effects the stability of the particles in the sol. At high pH, the surface charge causes the stability, while at low pH the lack of OH^- ions increases the stability by not causing the formation of Si-O-Si bonds between particles when they do interact. The sol ends up being least stable for a pH in the range of 5-6.

The porous silica samples prepared from Ludox for this study were gelled through the addition of a dissolved salt (NaCl for HS-40, NH_4Cl for AS-40). 5 ml of the appropriate salt solution was added to 20 ml of the colloidal silica while stirring to produce the desired molarity of salt in the final mixture. (The 0.290M NH_4Cl in AS-40 mixture used an addition of 15 ml salt water to 40 ml of AS-40.) The solution was then poured into four polystyrene cuvettes which were sealed with parafilm and a plastic cap and allowed to sit undisturbed until they were gelled. The remaining solution was sealed in a vial to gel as well. One additional HS-40 sample was created by allowing it to gel without any salt being added. It was sealed in a cuvette and sat undisturbed for nearly two years. As expected, the solutions with the largest salt concentration gelled the quickest.

After gelling, the network begins to shrink as additional bonds form, drawing the particles together and expelling water from the pores. Eventually, the gel pulls away from the walls of the cuvette and becomes loose. At this point, it was removed to a plastic sample box for further drying. To provide more thorough drying and perhaps

additional densification, the samples (not including the 0 M HS-40 sample) were heated in air to 600°C or 900°C for six hours, which produced weight losses of 5 - 10%. As discussed earlier, these temperatures will remove water and hydroxyl groups from the silica surface and, for samples heated to 900°C, a surface that is at least partly hydrophobic surface should result. This surface will have a greatly reduced number of hydroxyl groups which should reduce the binding of molecules to the surface. The HS-40 samples, however, cannot be heated above ~700°C due to the presence of sodium in the network. Alkali ions in silica are known to cause crystallization at relatively low temperatures:[39] Li produces quartz while Na produces cristobalite. This crystallization was seen in an HS-40 sample heated to 850°C in air. A Kaiser Optical Systems, Inc. Raman Microscope was used to identify the crystalline cristobalite phase formed in this piece as shown in Figure 4.8.[40] Therefore, these samples were only heated up to 600°C to dehydrate them. The presence of Na in the network is not entirely undesirable, though, because of the ability of the ion to block molecules from adsorbing to the surface of silica (this will be discussed in more detail later).

Nitrogen adsorption was used to characterize the pore size and distribution of these samples.[41] Table 4.4 lists the results of these measurements and Figures 4.9 and 4.10 show the pore size distributions determined from the desorption isotherms. The three AS-40 Ludox samples do not have a very large range of pore radii or porosity. The 0.149 M and 0.088 M samples appear to be nearly identical in terms of their surface area and porosity, which leads to essentially the same Wheeler average pore radius. Their pore size distributions are slightly different (Figure 4.9) and indicate that the 0.149 M

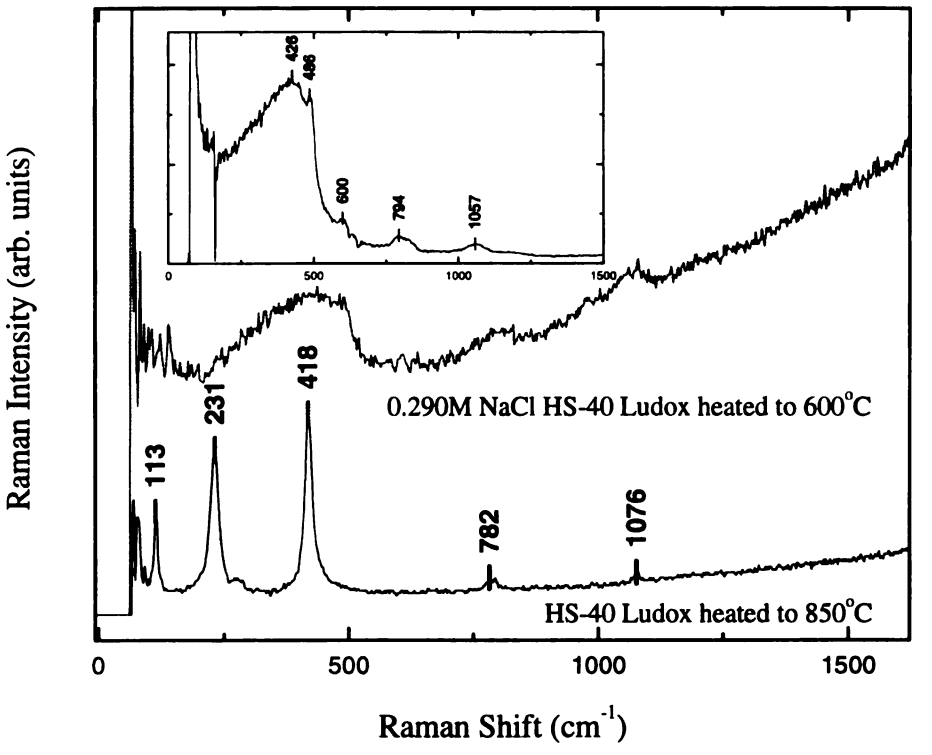

Figure 4.8: Raman spectra of HS-40 Ludox glasses heated to 600 °C (top) and 850 °C (bottom). The top spectra shows the broad Raman lines characteristic of fused silica. The lines labeled in the bottom spectra are lines characteristic of the crystalline silica phase of cristobalite. The spectra are offset and magnified for clarity. Both were acquired using the 633 nm line of a HeNe laser as the excitation. The insert shows the spectra of nonporous amorphous silica.

Table 4.4: Properties of the Ludox porous glasses as determined from nitrogen adsorption.

Sample	approx. gel time	max. temp (°C)	weight loss (%)	R_w (Å)	R_{PV} (desorp.) (Å)	R_{PV} (adsorp.) (Å)	R_{SA} (desorp.) (Å)	R_{SA} (adsorp.) (Å)	Surface Area (m^2/g)	Pore Volume (cm^3/g)	Porosity
0.290M AS-40	15 min	900	N/A	**117.2**	78.8 ± 28.9	144.3 ± 48.9	74.0 ± 23.9	93.4 ± 23.2	55.39	0.3246	**0.4166**
0.149M AS-40	< 17 hrs	900	8.5	**106.2**	66.1 ± 23.8	184.5 ± 41.8	53.8 ± 14.8	84.2 ± 15.5	42.67	0.2265	**0.3326**
0.088M AS-40	13 days	900	10	**103.3**	70.7 ± 20.9	138.6 ± 38.6	66.8 ± 25.1	84.3 ± 15.5	42.18	0.2180	**0.3241**
0.290M HS-40	25 min	600	~7.8	**107.4**	78.0 ± 35.4	171.4 ± 42.1	63.6 ± 25.3	73.7 ± 14.4	77.67	0.4169	**0.4784**
0.149M HS-40	< 14 hrs	600	6.7	**58.0**	124.3 ± 22.8	182.6 ± 26.1	20.3 ± 8.5	20.5 ± 8.2	20.78	0.0603	**0.1171**
0.088M HS-40	6 days	600	5.5	**63.5**	46.7 ± 15.9	71.24 ± 25.4	41.3 ± 11.8	54.4 ± 14.6	134.21	0.4259	**0.4837**
0 M HS-40	weeks	--	--	**47.6**	40.2 ± 10.5	56.3 ± 18.9	39.5 ± 12.3	43.2 ± 13.2	134.41	0.3201	**0.4132**

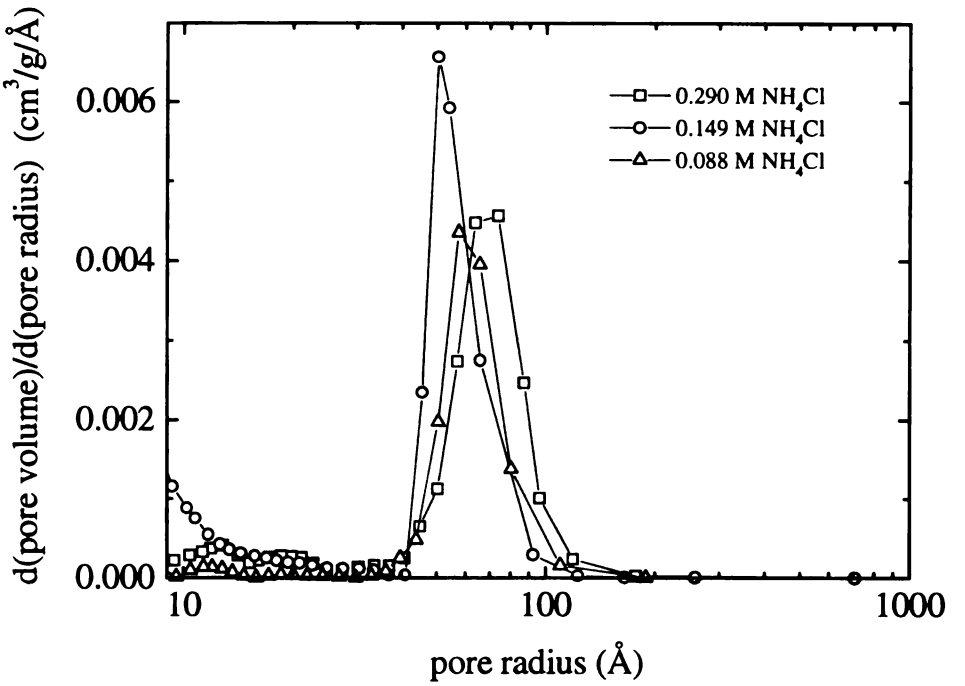

Figure 4.9: Pore size distribution of the AS-40 Ludox glasses calculated from the desorption isotherms.

sample has a smaller median pore radius. The 0.290 M sample, which gelled much faster than the others, has a larger average pore radius and a wider pore distribution. This is expected for a gel that formed quickly and did not have time to create a more compact structure.

Three of the four HS-40 Ludox samples follow the same progression: as the concentration of NaCl was reduced in the 0.290 M, 0.088M, and 0 M samples, the gel time increased, the average pore radius decreased, and the width of the pore size distribution decreased (Figure 4.10). This implies that as the sol is given more time to gel

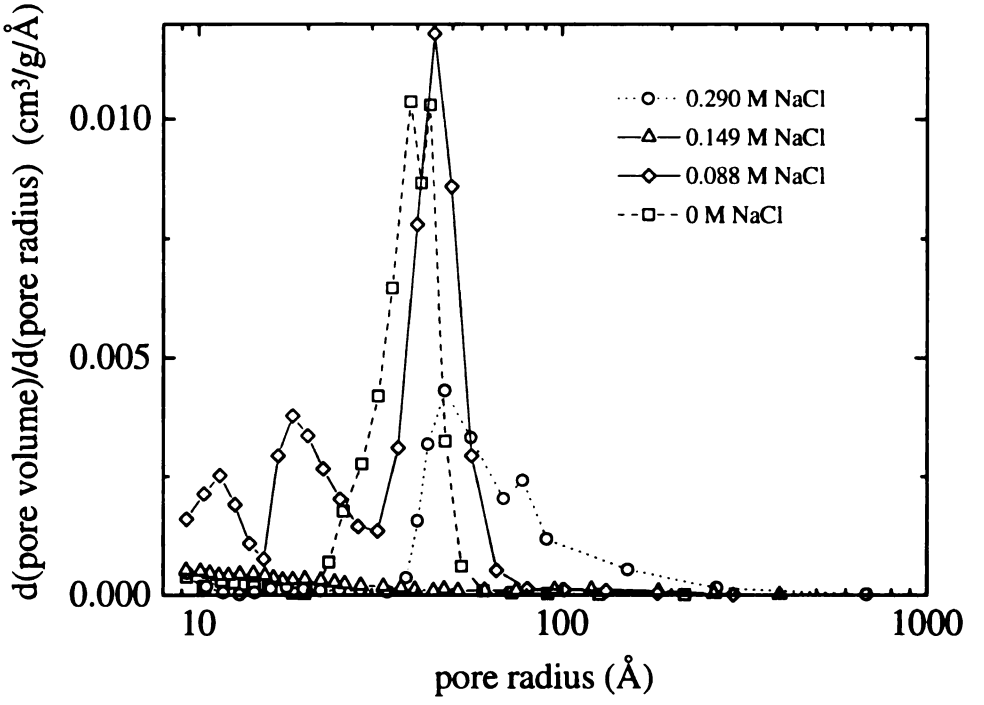

Figure 4.10: Pore size distribution of the HS-40 Ludox glasses calculated from the desorption isotherms.

it does form a more compact and uniform network. The 0.149M sample, on the other hand, is unlike any of the other samples. It has unusually low surface area and pore volume, and has no peak in the pore size distribution. This sample also has a mottled appearance, with some regions appearing whiter than others. This suggests that some regions have been sealed off from the rest of the network--leading to both the mottled appearance and the lowered surface area and pore volume. Fluid diffusion in this sample also does not conform to the other samples.

Comparing these results to the Gelsil results (Table 4.2 and Figure 4.4) we see that these samples are very different. The average pore sizes are quite large, but with porosities that are much less than the sol-gel produced Gelsil. The pore size distributions of the Gelsil glasses are significantly narrower than those of the Ludox, showing that their special preparation does create a porous network with pores of more uniform size.

VI. The manufacture and properties of Vycor

The Vycor 7930 sample was a gift from Corning[42] in the form of a 1/8" diameter rod. Vycor is produced from a borosilicate glass which is carefully heat treated to phase separate the Boron-rich region from the silica-rich regions, and then acid etched to remove the boron-rich phase. The rod was sectioned with a low-speed diamond impregnated saw to produce a section 0.065" thick for the FRS measurements. Another length was removed for nitrogen adsorption analysis. Figure 4.11 shows the pore size distribution for this glass which has an average pore radius of R_w = 24.5 Å and a porosity of 0.359. These values are very similar to the values found for the Vycor used in previous diffusion studies (Chapter 2). This glass is believed[43] to have a pore structure very different from that found in sol-gel produced glasses (as indicated by the difference in the porosities between it and Gelsil with a similar pore size), making it a very good comparison for the results found in the Gelsil glasses.

VII. Characteristics of the fluid and Methyl Red

The fluid used throughout this study was a mixture of 90% (by volume) glycerol ($HOCH_2CH(OH)CH_2OH$) and 10% deionized water. This fluid is transparent to visible light and has an index of refraction (n) at room temperature close to that of silica (~1.46).

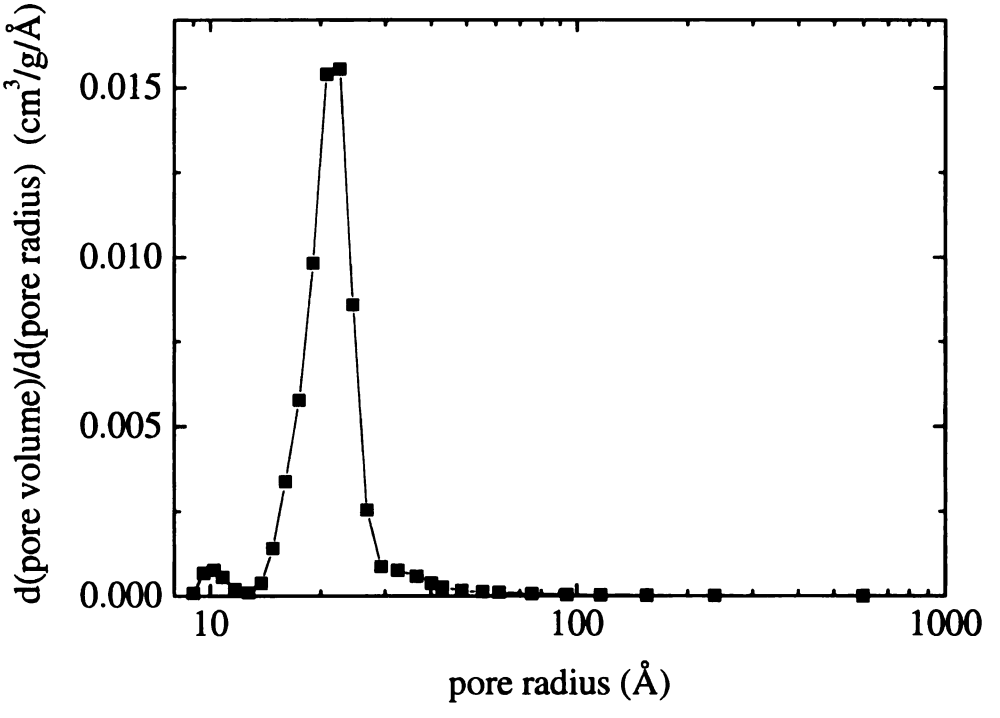

Figure 4.11: Pore size distribution of the Vycor porous glass calculated from the desorption isotherm.

In an optical experiment such as FRS, light scattered by variations in n causes a background signal which must be compensated for in the analysis of the detected signal. By closely matching the refractive index of the sample to the fluid in its pores, this scattered light may be eliminated. A second reason for choosing this fluid is that it mimics the surface of the silica. The tracer molecule added to this fluid is surrounded by -OH groups regardless of whether it is near or far from the pore walls. This means that the tracer molecule does not have a stronger affinity for the walls than the fluid, a situation which does occur if an anhydrous fluid is used.

Sodium hydroxide (NaOH) was added to the fluid for two purposes: to improve the solubility of the tracer dye, and to supply Na^+ ions to help block adsorption of the dye to the silica surface. The two batches of fluid made during this study had concentrations of 0.014M and 0.054M NaOH.

To this mixture of glycerol, water, and NaOH is added the tracer molecule, Methyl Red (2-[4-(dimethylamino)phenyl-azo]benzoic acid). (see Figure 4.12) Methyl Red is an azobenzene-based dye which was first used in an FRS experiment by Hervet *et al.*[44] to study mass diffusion in a liquid crystal and has since become one of the most common tracers in use in these experiments.[45] Methyl Red is a roughly planar molecule with lateral dimensions of ~7 by 15 Å. Commonly used as a pH indicator, the color of Methyl Red changes from red to yellow as the pH changes from 4.4 to 6.0. This color change is the result of a H^+ ion bonding with one of the nitrogen atoms making up the azo bridge between the phenyl rings.[46] (Figure 4.12a) As we will see later, this color change is a useful method of examining the interaction between Methyl Red and the surface of silica.

Like many members of the azobenzene-based family of dyes, Methyl Red is photochromic, meaning that it changes its color when it absorbs light. This color change occurs as the molecule undergoes isomerization--a conformational change of the molecule structure. As light is absorbed and the molecule is lifted to an electronic excited state, half of the double azo bond is broken, allowing the molecule to twist along that axis. When the electronic excitation decays, the azo bond is reformed, and the molecule may be left in the metastable cis configurational state (the cis isomer).[47] (Figure 4.12b)

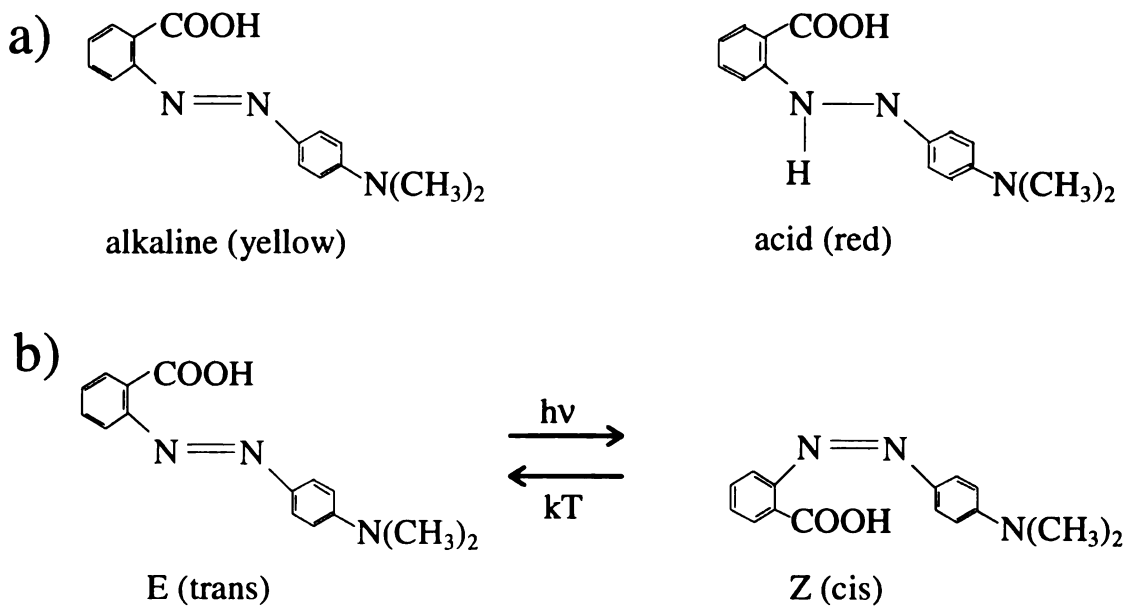

Figure 4.12: Methyl Red molecule used as the tracer molecule in the FRS experiments. The molecule is roughly planar with dimensions ~15 Å x ~ 7 Å. (a) The alkaline and acid forms of Methyl Red, showing hydrogen bonding to the azo bridge. (b) The trans and cis states of Methyl Red. The cis state may be created through absorption of light, and will decay thermally back to the trans state.

The two states of the dye are chemically identical, but differ in their electronic and optical properties.[48] Most important are the optical changes: the absorption bands change and the index of refraction changes. These changes are what make Methyl Red useful for FRS diffusion measurements. If the excitation beams are within the absorption band of the ground (trans) state, the interference pattern will be transferred into an identical pattern of cis state molecules, producing the desired modulation of the refractive index.

Figure 4.13 shows the ground state absorption spectrum (see Appendix A) of Methyl Red in the glycerol/water fluid. It is important to note that in the FRS experiments, the excitation laser (488 nm) lies within the absorption band, while the

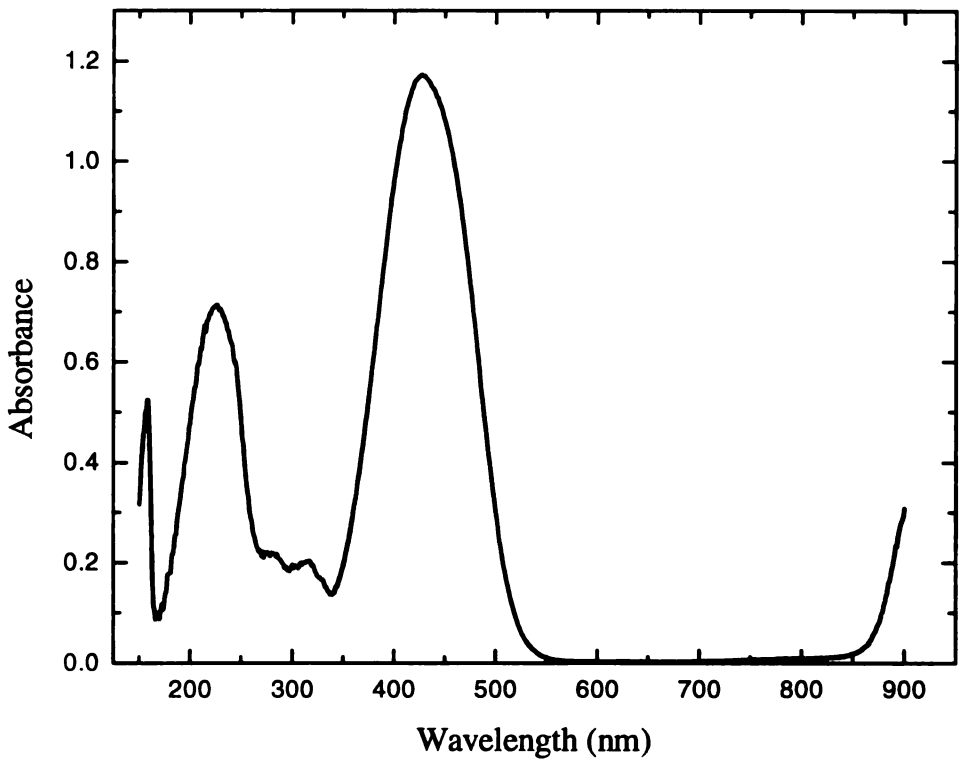

Figure 4.13: The absorption spectrum of Methyl Red in a mixture of 90% glycerol, 10% water, and 0.054 M NaOH.

probe laser (633 nm) lies well outside. When the dye is illuminated with the excitation laser, the absorption bands shift slightly. Figure 4.14 shows the difference in the absorbance between the illuminated fluid and the unilluminated fluid, indicating the difference in the absorbance of the cis and trans states of Methyl Red. We see that the absorption does not change at the probe wavelength. This indicates that the grating probed by the probe laser is an index of refraction grating, not an absorption grating. This is the conclusion reached in other experiments as well.[49]

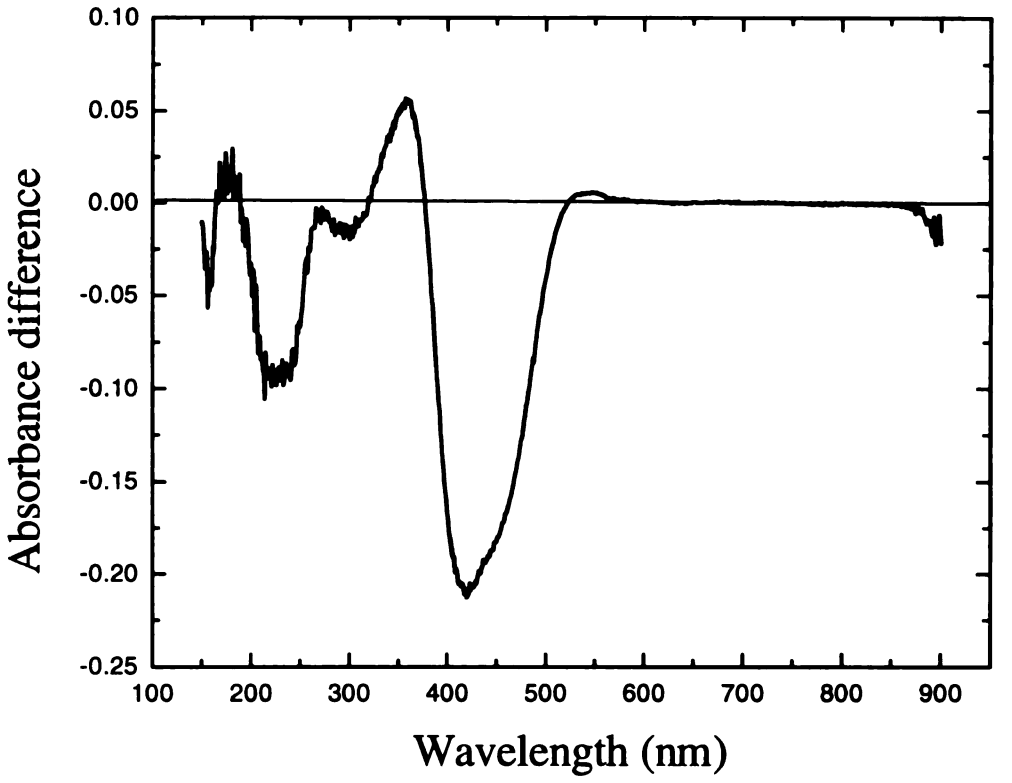

Figure 4.14: The change in the absorbance of Methyl Red when illuminated with 488 nm light. Plotted is the absorbance with the pump beam off subtracted from the absorbance with the pump beam on. A positive value means the absorbance is larger when it is illuminated.

The metastable cis state may relax to the trans state through thermal excitation at room temperature. The lifetime of this process is quite long compared to electronic excitations (on the order of seconds). This is necessary for studies of slow diffusion, because the excitation must exist long enough for the molecules to diffuse far enough to effect the refractive index modulation. The lifetime of cis Methyl Red in water has been shown[50] to depend upon the concentration of the OH^- ion in the solution. To verify this, a

room temperature transient absorption experiment was performed on three solutions of Methyl Red in water with varying concentrations of NaOH. Appendix A discusses the experimental setup used in this and other absorption experiments during this study. Figure 4.15 shows the lifetime of the cis state in 2.6mM Methyl Red in water with 0.006 to 0.14 M NaOH, excited by a 2 s long, 245 mW, 488nm laser pulse. Plotted are the results obtained at three different wavelengths of the absorbed light, which show good agreement over this range. Also shown is the lifetime measurement at 515 nm of the 2.64mM Methyl Red in 90% glycerol, 10% water (0.054 M NaOH) fluid. This result is quite consistent with the data of Methyl Red in water, and with the lifetime obtained from the analysis of FRS signals in this fluid.

Studies of other azobenzene derivatives that were incorporated into sol-gel glasses (incorporated directly into the silica network, not placed in a fluid in the pores), have shown that the lifetime of the cis state is affected in two ways.[51] Molecules that are hydrogen bonded to the surface show an increased lifetime, while molecules that can only reach the cis state in a strained configuration (because of the small volume available to it), show a faster relaxation to the trans state. This suggests that when the Methyl Red molecules in these experiments are placed in small pores and are not bound to the surface, the lifetime should be reduced from its value in the free, unbounded fluid.

VIII. Surface chemistry of silica and its interactions with Methyl Red

As discussed earlier, the hydrated surface of silica is covered with hydroxyl groups and adsorbed water. The surface hydroxyl groups are the sites that provide the acidic and chemically active character of silica.[52] One method for reducing the activity of

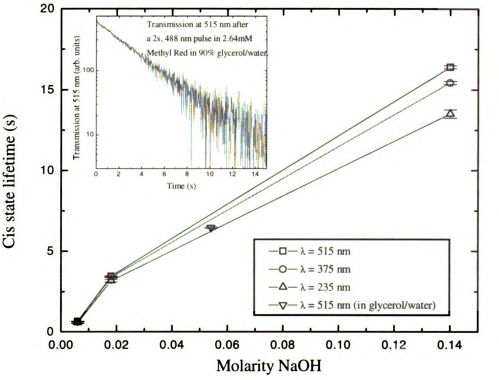

Figure 4.15: The lifetime of the cis Methyl Red molecule in water with different concentrations of NaOH. The "down triangle" point is the lifetime in the 90% glycerol/ 10% water solution used in the FRS measurements. The lifetimes were determined by transient absorption at room temperature. The dye was excited at 488 nm and the transmission of light at three other wavelengths was monitored to determine the decay rate. The inset shows one of these decays on a log scale.

the surface (i.e. reducing the adsorption of molecules from solution onto the surface) is to remove the hydroxyl groups through dehydration. This will produce a hydrophobic surface that has no hydroxyl groups and [53]will not adsorb molecules readily. Placing a completely dehydrated surface into water will not rehydrate it unless the water is at a very high pH (9 or greater), or the temperature is raised significantly above 100°C.

Methyl Red will readily adsorb to the surface hydroxyl groups on silica and in turn become bright red in color.[54] This is expected for this dye as it enters an acidic environment (see the earlier discussion on the pH properties of Methyl Red). The adsorption of Methyl Red has been used to measure the number of active hydroxyl sites on the silica surface, and in one study,[55] it was shown that as the number of hydroxyl sites decreases on a dehydrated silica surface, the adsorption of Methyl Red is reduced. It was also found that the presence of adsorbed water reduces the adsorption of Methyl Red[56] because the water interacts preferentially with the hydroxyl groups,[57] producing a less active surface in an aqueous solution. This demonstrates that the solvent used to carry Methyl Red will determine how strongly it interacts with the surface of the silica. If an anhydrous solvent like toluene or benzene is used, the dye will be preferentially pulled out of solution to adsorb on the surface.

To prevent molecules from adsorbing to the surface, the hydroxyl groups must be either removed or access to them must be blocked. One way to remove them is the aforementioned dehydration of silica. However, this treatment can cause the structure of the silica to change by closing pores. Another common technique is to use esterification--in other words, replace the hydroxyl groups with another chemical group that is not as active. This has been shown to be an effective method to block adsorption of Methyl Red.[58] In fact, it is not necessary to replace every hydroxyl group to produce the desired hydrophobic surface, as a "bushy" molecule can cover nearby hydroxyl groups and thereby block access to them as well.[59] A molecule does not need to be very large to

produce this steric blocking effect, because molecules as small as a methyl group (CH_3) are necessary if all the hydroxyl groups on a silica surface are to be removed.

A variety of chemicals have been used to esterify the surface of silica,[60] but a few are quite common and have also been used in previous studies of diffusion within porous silica: propanol,[61] dimethyldichlorosilane,[62] and hexamethyldisilazane.[63] Figure 4.16a schematically shows the silica surface after reacting with hexamethyldisilazane to leave trimethylsilyl groups on the surface.

There are problems with the use of esterification to stop adsorption on the silica surface. Not all the hydroxyl groups are replaced, and while most of those remaining may be sterically blocked, not all will be. This will allow some adsorption to occur, particularly when an anhydrous solvent is used. More importantly, the addition of these molecules on the surface can dramatically alter the structure of the pores, particularly when the pores are very small. As the surface is covered, the effective pore radius will be reduced, which can cause pores that had been accessible to a diffusing particle through narrow openings to become inaccessible. As an aside, it should be noted that by "removing" small pores the measured diffusion coefficient may actually increase, because the diffusing particles are then allowed to move only in the relatively unrestrictive larger pores. Therefore, the surface treatment used can alter the fluid diffusion in the pores.

A third way of reducing adsorption to hydroxyl sites is well known, but not as commonly used, because it does not produce a permanent hydrophobic surface. For pH > 2, negatively charged Si-O^- sites will attract counterions from the surrounding fluid. Na^+ counterions in an aqueous solution are surrounded by six water molecules which increase

(a) treated with hexamethyldisilazane

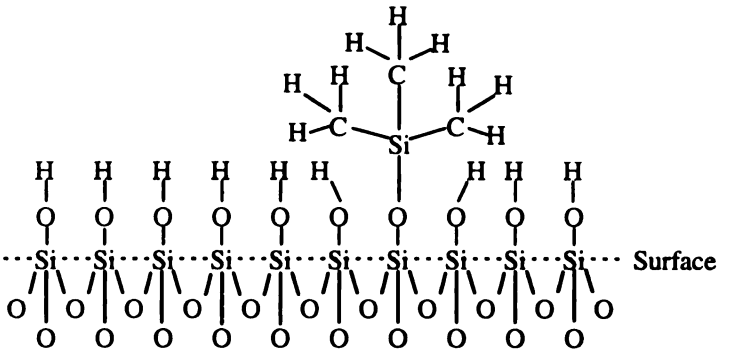

(b) pH above neutrality

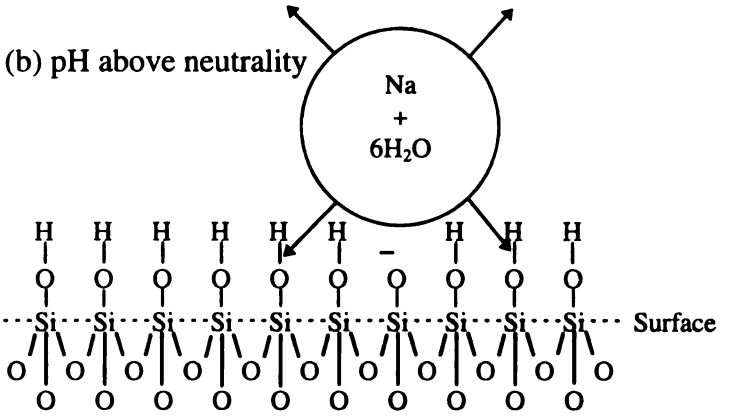

Figure 4.16: (a) Silica surface reacted with hexamethyldisilazane to place trimethylsilyl groups on the surface. (b) Silica surface with a Na^+ counterion (and its entourage of water molecules) above a charge site on the surface.

the effective size of the ion. While the ion is not physically bound to the charge site on the surface, it will remain very close to it and shield it from other molecules in the solution. Due to the size of the water "cloud" surrounding it, neighboring hydroxyl sites are also covered (Figure 4.16b).[64] The effect of the counterion is the same as the attached molecule on an esterified surface, except for two key features: the surface is not

hydrophobic and the sodium ion is still mobile. This means that the pore structure is left unchanged, and the likelihood of a pore being completely blocked off is greatly reduced.

If Methyl Red is within a porous silica containing sufficient sodium and OH^-, it will not change its color, indicating that the molecule has not been adsorbed onto the hydroxyl sites and is not experiencing a very low pH. Without Na^+ ions, the bright red (low pH) color is found, and no FRS signal can be detected, indicating the molecules are bound at the azo bridge. If the porous silica is made with sodium incorporated into it (like in the HS-40 Ludox samples), no additional sodium ions are required to prevent adsorption.

A clear indication of this is the behavior of a piece of untreated silica placed in a solution of Methyl Red, glycerol, water, Na^+, and OH^-. The initially white surface turns red as the fluid diffuses into the pores and Methyl Red is bound to the surface. However, as time goes on, the Na^+ and OH^- ions diffuse into the pores--slower than the dye because they interact strongly with the pore walls. As they appear in the pores, the pH increases, and the Na^+ ions block the hydroxyl binding sites, freeing any Methyl Red bound to the surface and turning color back to the original orange color of the solution. If the silica had been made with Na already in the network, the color of the solution never turns red as it diffuses in.

To incorporate Na into the pores before the addition of Methyl Red, the Gelsil samples and the Vycor are first soaked in a solution of water and sodium hydroxide, with the pH kept below ~9 to avoid the dissolution of the silica. The sample must be left in the solution for many days, in order to allow the ions time to diffuse into the pores. The

time required depends upon the pore size of the sample, because the diffusion is slower through small pores. It may be necessary to periodically refresh the solution to add more ions. The sample is then removed from the liquid and placed in the solution of Methyl Red and glycerol. If the sample begins to turn red, it is removed, then rinsed and soaked in water and NaOH. Once in the Methyl Red fluid, the sample is allowed to sit for several days to equilibrate. It is sometimes heated to reduce the viscosity of the fluid and speed its infusion into the pores. It should be noted that in all these samples, the fluid is seen to enter the silica uniformly from all sides. This implies that the pores form a well connected network.

In conclusion, we use a hydrophilic fluid along with added Na^+ ions in order to block the adsorption of our Methyl Red tracer molecule to the surface. By simply monitoring the color of the fluid solution in the silica, we can determine if the tracer is bound to the surface. With this system, we can probe only the effect of the pore geometry on the diffusive behavior of the fluid, not the effect of the chemical interactions between the tracer and the walls.

References

[1] D.W. Breck, *Zeolite Molecular Sieves: Structure, Chemistry and Use* (John Wiley and Sons, New York, 1974).

[2] R.M. Barrer, *Zeolites and Clay Minerals as Sorbent and Molecular Sieves* (Academic Press, New York, 1978).

[3] C.T. Kresge *et al*, Nature **359**, 710 (1992).

[4] R.K. Iler, *The Chemistry of Silica* (John Wiley and Sons, NY 1979), p. 551.

[5] R.K. Iler, ibid., Chapter 4.

[6] E.M. Rabinovich, in *Sol-Gel Optics: Processing and Applications,* edited by L.C. Klein (Kluwer Academic, Boston, 1994), p. 1.

[7] R. Zallen, *The Physics of Amorphous Solids* (John Wiley and Sons, Inc., New York, 1983) Chap. 4.; D. Stauffer, A. Coniglio, and M. Adam, Adv. Polym. Sci. **44**, 103 (1982).

[8] S.R. Chaudhuri and A. Sarker, in *Sol-Gel Optics: Processing and Applications,* edited by L.C. Klein (Kluwer Academic, Boston, 1994), p. 83.

[9] L.L. Hench and R. Orefice, *Encyclopedia of Chemical Technology*, 4th ed., vol. 22, p. 497.

[10] J. Fricke, Sci. Amer. 258, 92 (1988).

[11] K.K. Unger, *Porous Silica* (Elsevier, Amsterdam, 1979), p. 52.

[12] L.C. Klein, ed. *Sol-Gel Optics: Processing and Applications* (Kluwer Academic, Boston, 1994).

[13] R.K. Iler, ibid., p. 548.

[14] N.A. Seaton, Chem. Eng. Sci. **46**, 1895 (1991).

[15] F.A.L. Dullien, *Porous Media: Fluid Transport and Pore Structure* (Academic Press, New York, 1979), p. 88.

[16] B.P. Flannery *et al*, Science **237**, 1439 (1987).

[17] P.W. Schmidt *et al*, J. Chem. Phys. **90**, 5016 (1989); R. Vacher *et al*, Phys. Rev. B. **37**, 6500 (1988).

[18] O. Lamrous *et al*, Revue de Physique Applique **24**, 607 (1989).

[19] M.D. Shattuck *et al*, Phys. Rev. Lett. **75**, 1934 (1995).

[20] Dullien, ibid., p. 97-99.

[21] S.J. Gregg and K.S.W. Sing, *Adsorption, Surface Area, and Porosity* (Academic Press, New York, 1967), p. 182-3.

[22] Dullien, ibid., p. 98.

[23] S.J. Gregg and K.S.W. Sing, ibid.

[24] S.J. Gregg and K.S.W. Sing, ibid., p. 310-312.

[25] S. Brunauer, P.H. Emmett, and E. Teller, J. Amer. Chem. Soc. **60**, 309 (1938).

[26] S.J. Gregg and K.S.W. Sing, ibid., p. 137-8.

[27] E.P. Barrett, L.G. Joyner, and P.H. Halenda, J. Amer. Chem. Soc. **73**, 373 (1951).

[28] Dullien, ibid., p. 106.

[29] J.H. DeBoer and B.C. Lippens, J. Catalysis **3**, 38 (1964); K.W. Powers, private communication.

[30] A. Wheeler, in *Catalysis*, vol. 2, edited by P.H. Emmett (Reinhold, New York, 1955), p. 116; Dullien, ibid., p. 170.

[31] K.K. Unger, ibid., p. 37-40.

[32] K.W. Powers, private communication.

[33] Geltech, Inc., One Progress Blvd., Box 8, Alachua, FL 32615.

[34] L.L. Hench and J.L. Nogues in *Sol-Gel Optics: Processing and Applications,* edited by L.C. Klein (Kluwer Academic, Boston, 1994), p. 59.

[35] L.L. Hench in *Science of Ceramic Chemical Processing*, edited by L.L. Hench and D.R. Ulrich (Wiley, New York, 1986), p. 52.; S.R. Chaudhuri and A. Sarker, ibid., p. 83.

[36] Porous Materials, Inc., 83 Brown Rd., Bldg. 4, Ithaca, NY 14850.

[37] L.L. Hench and J.K. West, Chem. Rev. **90**, 33 (1990); L.L. Hench in *Science of Ceramic Chemical Processing*, edited by L.L. Hench and D.R. Ulrich (Wiley, New York, 1986), p. 52.

[38] DuPont Speciality Chemicals, 1007 Market Street, Wilmington, DE 19898.

[39] R.K. Iler, ibid., p. 548.

[40] R.S. Darling, I.-M. Chou, and R.J. Bodnar, Science **276**, 91 (1997); S.R. Elliott, *Physics of Amorphous Materials*, 2nd ed. (Wiley, New York, 1990), p.166.

[41] Porous Materials, Inc., 83 Brown Rd., Bldg. 4, Ithaca, NY 14850.

[42] Corning, Inc., Corning, NY 14831

[43] P. Levitz *et al*, J. Chem. Phys. **95**, 6151 (1991).

[44] H. Hervet, W. Urbach, and F. Rondelez, J. Chem. Phys. **68**, 2725 (1978).

[45] J.A. Wesson *et al*, J. Appl. Phys. **53**, 6513 (1982); A. Barish, M.S. Bradley, and C.S. Johnson, Jr., Rev. Sci. Instrum. **57**, 904 (1986); J.L. Xia and C.H. Wang, J. Chem. Phys. **88**, 5211 (1988); H.S. Park, J. Sung, and T. Chang, Macromolecules **29**, 3216 (1996).

[46] Éva Bányai, in *Indicators*, edited by E. Bishop (Pergammon, 1972).

[47] H. Rau, in *Photochromism: Molecules and Systems*, edited by H. Dürr and H. Bouas-Laurent (Elsevier, Amsterdam, 1990), p. 178.

[48] H. Zollinger, *Azo and Diazo Chemistry* (Interscience, New York, 1990), p. 59; M. Irie, in *Applied Photochromic Polymer Systems*, edited by C.B. McArdle (Chapman and Hall, New York, 1992), p. 177.

[49] M. Terazima, K. Okamoto, and N. Hirota, J. Phys. Chem. **97**, 5188 (1993).

[50] A. Sanchez and R.H. de Rossi, J Org. Chem. **58**, 2094 (1993).

[51] M. Ueda *et al* J. Non-Cryst. Sol. **163**, 125 (1993); M.Ueda *et al*, Chem. Mater. **4**, 1229 (1992); M.Ueda *et al*, Chem. Mater. **6**, 1771 (1994);B.C. Dave, B. Dunn, and J.I. Zink, in *Access in Nanoporous Materials*, edited by T.J. Pinnavaia and M.F. Thorpe (Plenum Press, New York, 1995), p. 141.

[52] R.K. Iler, ibid., p. 182.

[53] R.K. Iler, ibid., p. 661,663.

[54] I. Shapiro and I.M. Kolthoff, J. Amer. Chem. Soc. **72**, 776 (1950); W.K. Lowen and E.C. Broge, J. Phys. Chem. **65**, 16 (1961).

[55] I. Shapiro and I.M. Kolthoff, ibid.

[56] I. Shapiro and I.M. Kolthoff, ibid; K.K. Unger, ibid., p. 210.

[57] K.K. Unger, ibid., p.130.

[58] W.K. Lowen and E.C. Broge, ibid.

[59] R.K. Iler, ibid., p. 689.

[60] Cabot Corp., P.O. Box 188, Tuscola, IL 61953. Technical data sheets TSD-121,130,131.

[61] W.D. Dozier, J.M. Drake, and J. Klafter, Phys. Rev. Lett. **56**, 197 (1986).

[62] R. Messager *et al*, Europhys. Lett. **10**, 61 (1989).

[63] C.K. Colton, C.N. Satterfield, and C.-J. Lai, Amer. Inst. Chem. Eng. J. **21**, 289 (1975); Y. Guo et al , Phys. Rev. A **46**, 3335 (1992).

[64] R.K. Iler, ibid., p. 657-8.

Chapter 5

DIFFUSION IN GELSIL POROUS SILICA

I. Forced Rayleigh scattering decay curves

Gelsil samples that were infused with Methyl Red, glycerol, and water were transferred along with some of the fluid to the temperature controlled sample cell and allowed to equilibrate for at least 12 hours before any data were taken. In order to press the windows against the sample on both sides, the sample cell was screwed closed to compress the viton o-ring between the windows. The distance between the windows varied from sample to sample because of the different sizes of each cylindrical sample (5 - 6 mm in diameter and 2 - 3 mm thick). This was done to prevent a layer of free fluid between the sample and the window from producing an additional diffracted signal. FRS signals were then acquired over a range of temperatures of 10 - 38.8 °C and grating periods of $\Lambda \approx 1.2$ - 7.5 μm. These grating wavelengths are several orders of magnitude larger than the sizes of the pores in the silica samples. In this fluid, maximum diffraction efficiencies (see Chapter 3) of $\eta \approx 1 \times 10^{-6}$ to 5×10^{-4} were found, which correspond to modulations of the index of refraction of $\Delta n \approx 1 \times 10^{-7}$ to 2×10^{-6}. These values of η were calculated from the largest diffracted signal during an excitation pulse and are therefore not steady-state values of the diffraction efficiency.

The decay signals behaved as single exponentials both in the free fluid and the Gelsil, with only a few exceptions. The top plot in Figure 5.1 shows the decays in the five Gelsil samples at $\Lambda = 1.225$ μm and 10.0 °C on a log scale to demonstrate the single exponential behavior. In this plot, the steepest slope corresponds to the largest pore

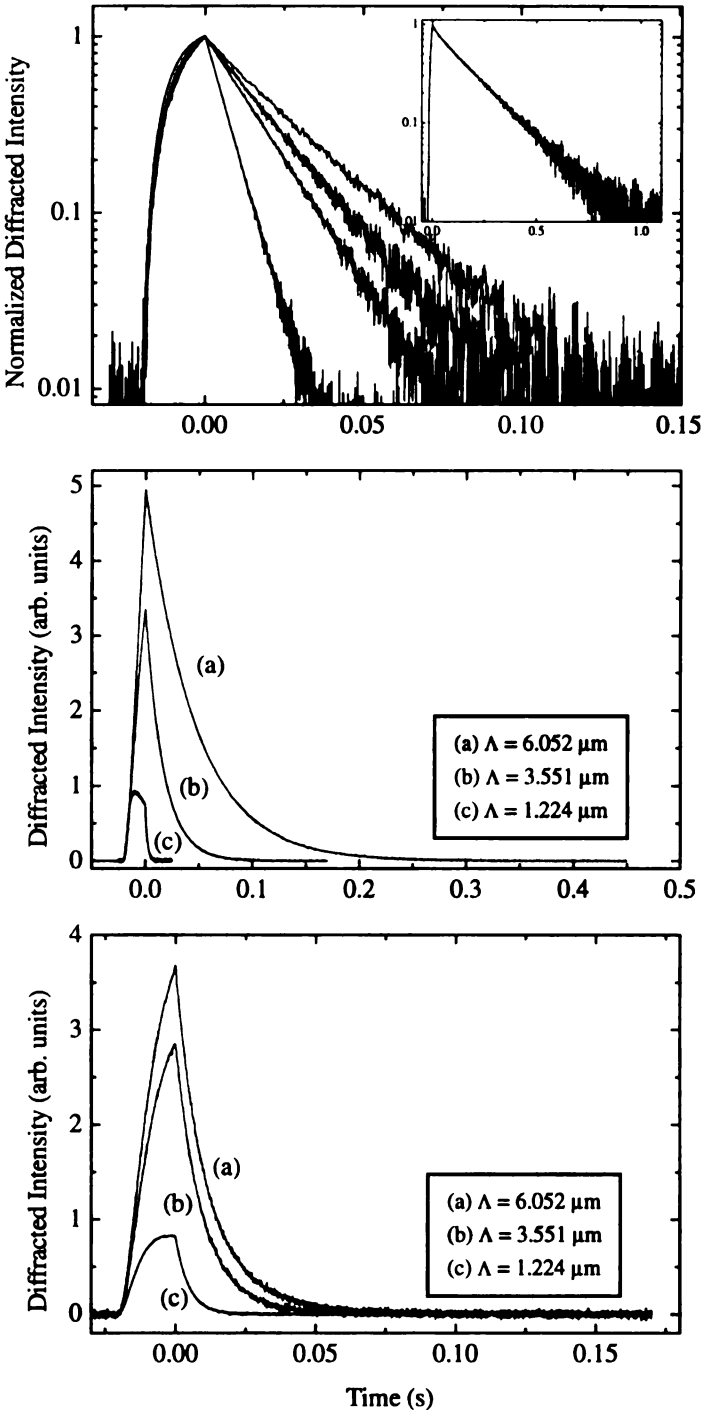

Figure 5.1: (Top): Normalized FRS decays of Methyl Red within the five Gelsil samples (r_p = 14.0, 16.4, 27.7, 35.5 and 91.5 Å) at Λ = 1.225 μm and 10.0 °C plotted on a log scale. The slope decreases with decreasing pore size. (Middle and Bottom): FRS decays of Methyl Red in the free fluid (middle) and within the 35.5 Å pore radius Gelsil sample (bottom) for three different values of Λ at 27.8 °C, plotted on a linear scale.

radius sample, and the slope of the decay curves decreases as the pore size decreases. The inset plot is the data from the smallest pore size sample, shown separately because its slope is much less than the others. Shown in the lower two plots of Figure 5.1 are examples of the decay curves found in both the fluid and the 35 Å sample for three different values of Λ, demonstrating how the decays change with Λ. In two of the samples, the data taken at the largest values of Λ deviated from single exponential behavior. As discussed previously, these deviations may occur if the cis and trans states of the Methyl Red molecule diffuse at different rates, if some of the Methyl Red diffuses slower than the rest because it is interacting with the surface, or if another species is diffusing as well. For the 27.7 Å pore radius sample, the non-exponential behavior was attributed to the sample cracking under the pressure of the windows and the thermal cycling of the sample cell. In previous samples that had broken apart, the slow movement of pieces containing a population grating of Methyl Red was seen to produce an additional slow decay similar to that found in the 27.7 Å sample. Knowing this, the signals were fit to a double exponential decay equation of the form of Equation 3.18:

$$(5.1) \quad I = \left(Ae^{-bt} + Ce^{-dt} + F\right)^2 + G$$

in order to extract the relatively fast decay due to the diffusion of fluid from the additional, relatively slow decay from the motion of the silica pieces. These results were then combined with the single exponential decays found at smaller Λ to determine the diffusion coefficient.

The 14.0 Å pore radius sample showed non-single exponential behavior at the very largest values of Λ, but did not deviate enough to reliably fit to Equation 5.1. In this

case, the three points showing this behavior were discarded. In some of the gelled Ludox and Vycor samples discussed in the next chapter, the same behavior was seen. In those cases, resoaking the samples in NaOH and water to supply more Na^+ in the pores resulted in decays showing single exponential behavior, but with a normalized diffusion coefficient that was unchanged from what was found before the samples were resoaked. This shows that it is possible to analyze non-single exponential decays to determine meaningful diffusion coefficients.

II. Determination of the diffusion coefficient

Once the decay rates were found, they were plotted against the square of the grating wavevector (q^2). If a straight line results, then it verifies that normal, Fickian diffusion is occurring, with $\langle r^2 \rangle \propto$ time. The lines are fit to Equation 3.16:

$$\frac{1}{\tau} = Dq^2 + \frac{1}{\tau_1} \tag{5.2}$$

to determine the associated diffusion coefficient and dye lifetime. All the samples in this study show this normal diffusive behavior. Figure 5.2 is a plot of $\frac{1}{\tau}$ vs. q^2 for both the free fluid and the fluid within the 16.4 Å pore radius sample at four temperatures. There are several things to note in these plots. First, the difference in the slope between the fluid and the silica data, which indicates the difference in the diffusion coefficient in the two environments. Second, the slope increases dramatically as the temperature rises. This is due to the decreased viscosity of the fluid mixture (causing a corresponding increase in the diffusion coefficient) at higher temperatures. Third, there is a change in the y-intercept of the data as the temperature changes. The intercept corresponds to the

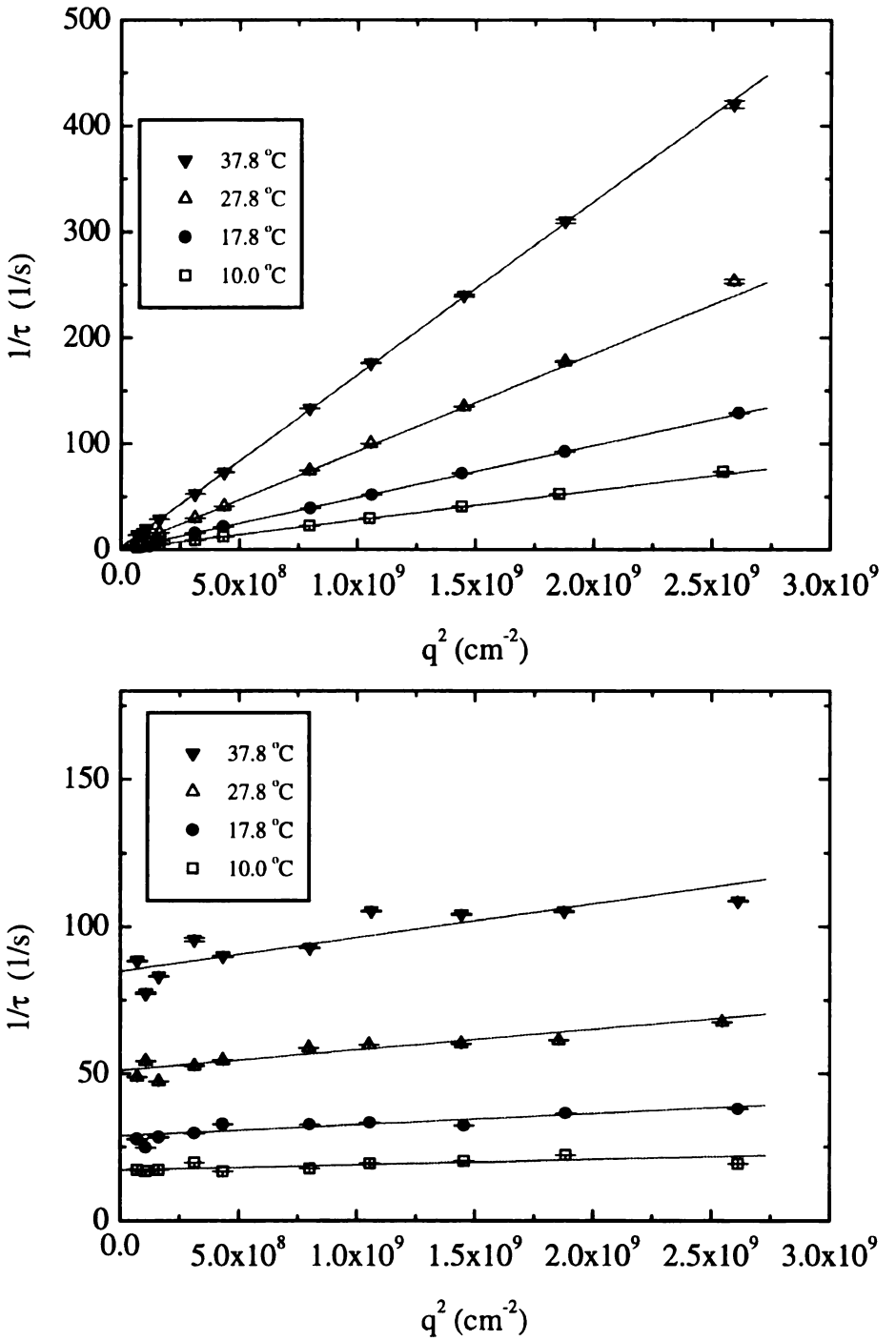

Figure 5.2: The FRS decay rate ($1/\tau$) vs. q^2 in the free fluid (top) and within the 16.4 Å radius Gelsil sample (bottom) at four different temperatures. Also shown as solid lines are the fits to Equation 5.2.

decay rate of the dye back to the ground state, so an increasing intercept implies a decreasing lifetime of the excited state of the dye. Therefore, as the temperature increases, the dye lifetime decreases, as expected for a thermally activated process. Fourth, the dye lifetime is much shorter in the silica than in the free fluid. This will be discussed in the next section.

Having very slow diffusion and short dye lifetimes means that the molecules may not diffuse very far before they decay to the ground state. That distance can be estimated from $\langle r^2 \rangle = 6Dt$, where t is set equal to τ_{life}, which (along with D) is determined from the $\frac{1}{\tau}$ vs. q^2 data. This distance can then be compared to $\Lambda/2$, the distance between the peak and the valley of the transient concentration grating created in the fluid. The smallest ratio of $\sqrt{\langle r^2 \rangle}$ to $\Lambda/2$ found in these data is ~5%, which occurred in the 14.0 Å sample at the highest temperature, 38.8°C, and the largest grating spacing Λ = 7.42 μm, which means that an average particle traveled approximately 1800 Å, or the length of over 60 pores. Even in this extreme case, the diffusive behavior is easily measured (and is seen to be normal diffusion), because the grating decay rate depends quadratically on q. This points out the need to measure the decay rate at several values of Λ in order to prove the existence of normal diffusive behavior and to separate D from τ_{life}. The temptation to save a great deal of time and only measure the decay rate at one value of Λ will almost certainly lead to an incorrect conclusion about the diffusive behavior. Note that even when $\sqrt{\langle r^2 \rangle} < \Lambda/2$, the grating modulation is still reduced by diffusion because the

grating has a sinusoidal profile, and a diffuser does not have to travel the entire $\Lambda/2$ distance to change the concentration profile.

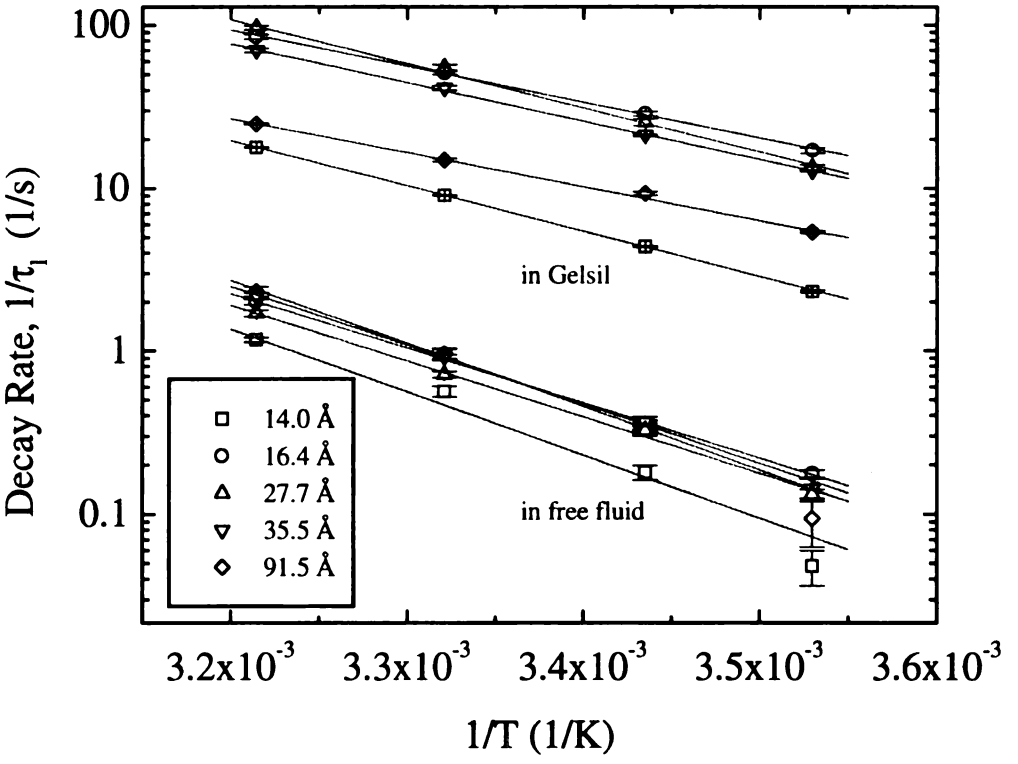

Figure 5.3: The decay rate of the thermal isomerization of cis Methyl Red back to trans Methyl Red ($1/\tau_1$) in the fluid and within all the Gelsil samples vs. 1/T. Each data set is fit to Equation 5.3 to determine an activation energy for the process.

III. Temperature dependence of the Methyl Red lifetime

Since the decay rate of cis Methyl Red back to trans Methyl Red may carry some information regarding the environment the molecule is in (Chapter 4), the activation energy of this process is of interest. Figure 5.3 plots the log of the decay rate $\frac{1}{\tau_1}$ against $\frac{1}{T}$ for the data taken in every Gelsil sample and the free fluid just outside each sample. Each data set is fit with:

$$\frac{1}{\tau_1} = A \exp\left(-\frac{E_a}{k_B T}\right), \tag{5.3}$$

where A is a constant, E_a is the activation energy, and k_B is the Boltzmann constant. The most striking aspect of this plot is the clear separation between the data in the Gelsil and the data in the free fluid, showing an order of magnitude difference in the decay rate between the two locations.

Table 5.1 lists the activation energies determined from the fits in Figure 5.3. While there is no believable correlation between the pore size and the activation energy, there is a real reduction in the activation energy when the Methyl Red is in the pores, from the value in the free fluid. These two results, that the Methyl Red has a higher decay rate and a lower activation energy in the pores may be due to two effects: the pH of the fluid in the pores, and the small volume of the pores themselves. As discussed in Chapter 4 (VII), the lifetime of Methyl Red is dependent upon the concentration of the OH^- ion. Because OH^- ions react with surface hydroxyl groups on silica (producing H_2O and $Si\text{-}O^-$, which attracts the Na^+ ions), the region near the silica surface has a pH less

Table 5.1: Activation energies of the thermal cis to trans isomerization of Methyl Red in the free fluid and within the Gelsil samples.

Gelsil pore radius (Å)	Activation energy in free fluid (eV)	Activation energy in Gelsil (eV)
14.0	0.77 ± 0.08	0.552 ± 0.006
16.4	0.67 ± 0.02	0.44 ± 0.01
27.7	0.68 ± 0.03	0.54 ± 0.02
35.5	0.72 ± 0.02	0.467 ± 0.007
91.5	0.77 ± 0.05	0.42 ± 0.01

than the bulk fluid. As the pores get smaller, the Methyl Red in the pores is always close to a wall, and is therefore always in an environment with a lower pH level. Also, other work has shown (Chapter 4 VI) that the decay rate of the cis state of azobenzenes increases if the molecules are located in regions where the cis state can only form in a strained configuration.[1] The same work indicates that the decay rate will decrease if the molecule is bound to the surface through hydrogen bonds. These results for the decay rate and the activation energy of Methyl Red in the Gelsil imply that the molecule is not bound to the surface of the silica, but is in a region of lower pH.

IV. Temperature dependence of the diffusion coefficient

As we saw in Figure 5.2, the diffusion coefficient varies with temperature both in the free fluid, D_o, and in fluid within the sample, D. Figure 5.4 plots the log of D and D_o as a function of $\frac{1}{T}$ for one of the Gelsil samples. Over this small range of temperatures, the data can be fit to an exponential

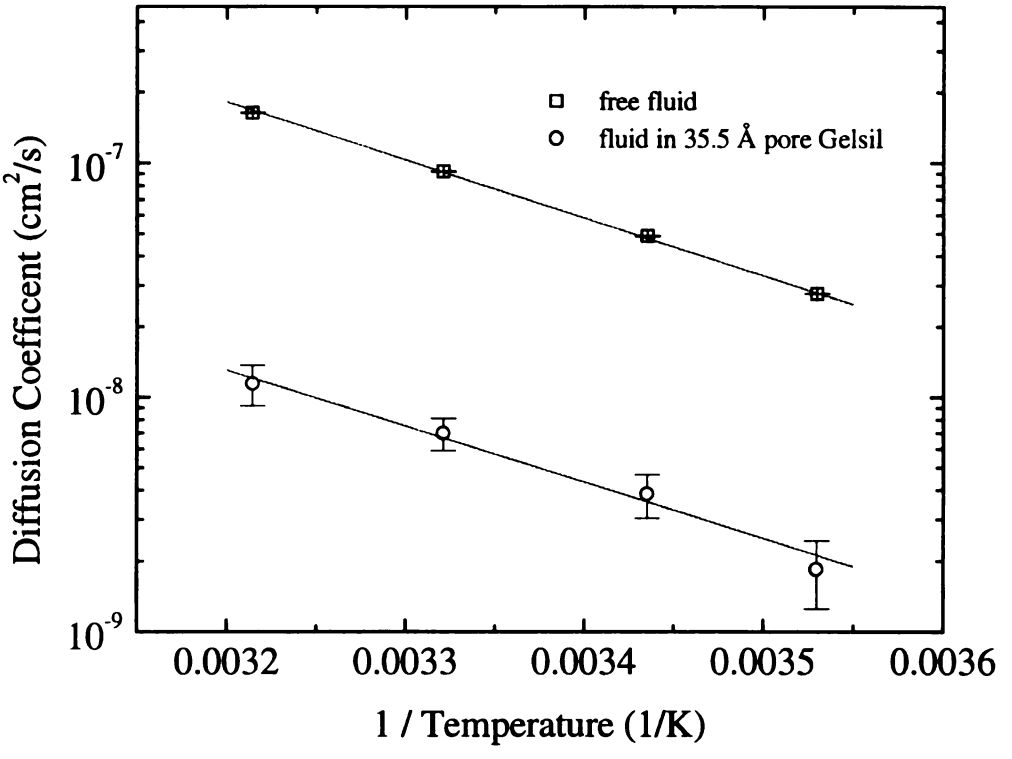

Figure 5.4: The diffusion coefficient in the free fluid and within the 35.5 Å pore radius Gelsil sample plotted vs. 1/T. Both data sets are fit to Equation 5.4 to determine an activation energy.

$$D = A \exp\left(-\frac{E_a}{k_B T}\right) \tag{5.4}$$

to determine an activation energy (E_a) for the diffusive process. Table 5.2 gives the results of these fits which show no clear trend. The small range and small number of temperatures examined make it difficult to draw any conclusion about these results. We do see, however, that the diffusion coefficient is highly temperature dependent.

Table 5.2: Activation energies of D and D_o in the free fluid and within the Gelsil samples.

Gelsil pore radius (Å)	Activation energy in free fluid E_a (eV)	Activation energy in Gelsil E_a (eV)
14.0	0.491 ± 0.007	0.501 ± 0.117
16.4	0.489 ± 0.008	0.475 ± 0.045
27.7	0.515 ± 0.008	0.449 ± 0.033
35.5	0.493 ± 0.010	0.551 ± 0.033
91.0	0.448 ± 0.009	0.457 ± 0.009

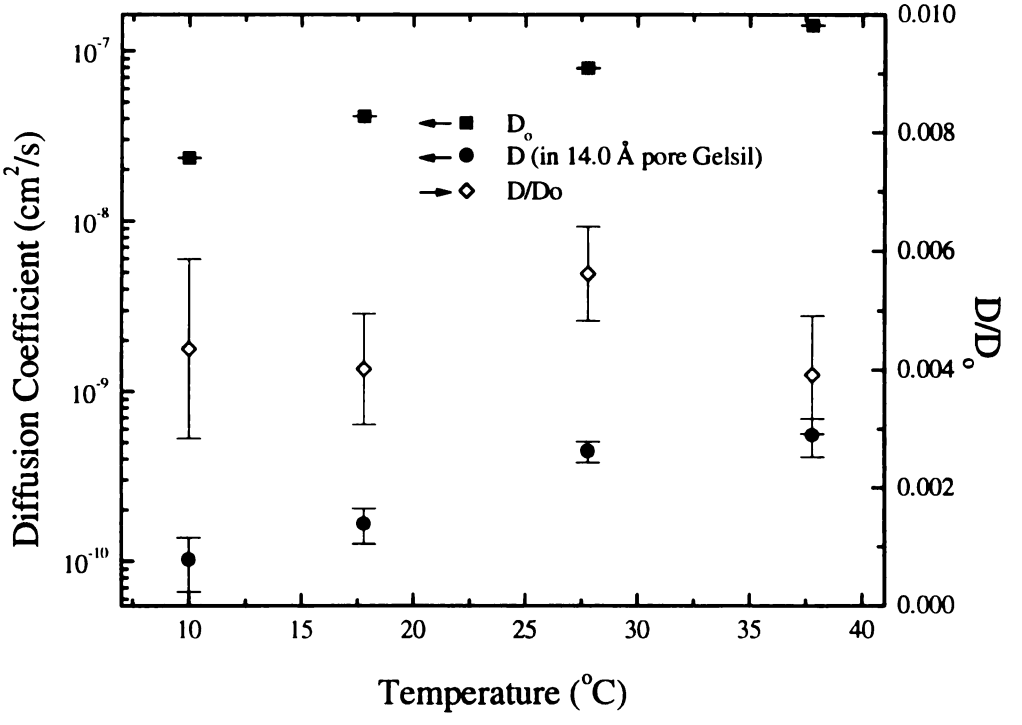

Figure 5.5: D, D_o, and D/D_o for the 14.0 Å pore radius Gelsil sample as a function of the temperature. D and D_o change by nearly and order of magnitude, while D/D_o is essentially constant.

Figure 5.5 plots the diffusion coefficients in both the free fluid and in the silica against temperature for one of the Gelsil samples. Also plotted is the normalized diffusion coefficient D/D_o. Even though D and D_o vary considerably over this range, their ratio does not. Figure 5.6 demonstrates that this normalized diffusion coefficient is temperature independent for all the Gelsil samples. This indicates that D/D_o is insensitive to changes in the properties of the fluid, but is highly sensitive to the pore structure of the silica. This is important, because it means that the normalized diffusion coefficient is

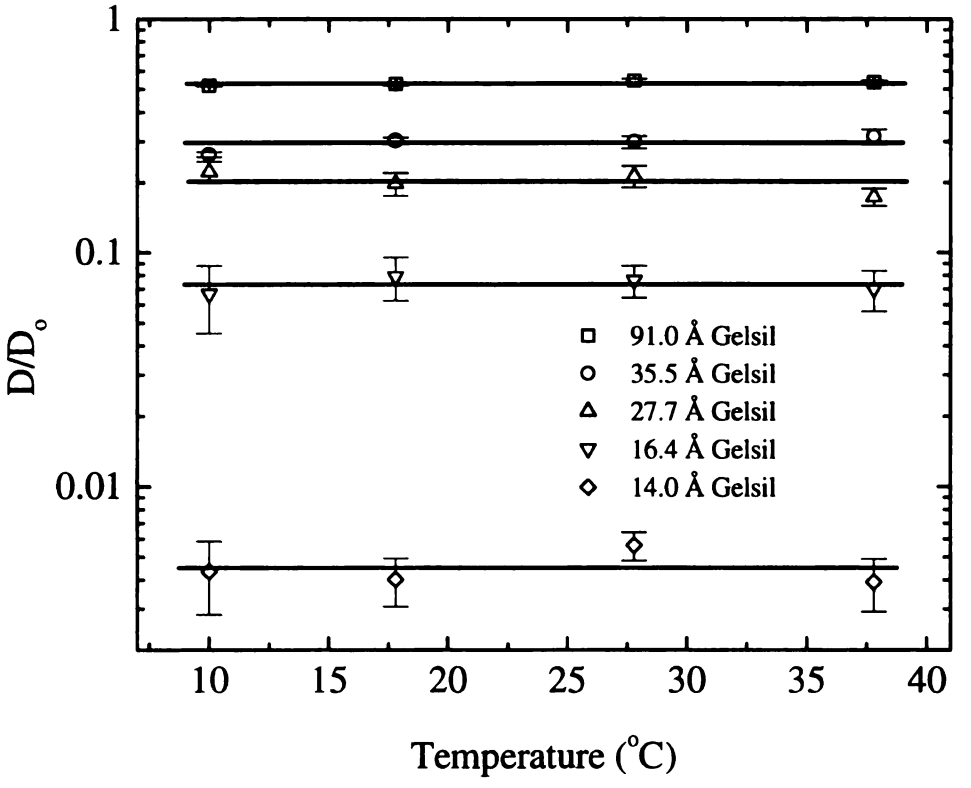

Figure 5.6: The normalized diffusion coefficient, D/D_o, for all the Gelsil samples plotted against the temperature. The straight lines are the average values of D/D_o.

Table 5.3: Average normalized diffusion coefficients, D/D_o, within the Gelsil samples.

Gelsil pore radius (Å)	D/D_o
14.0	0.0045 ± 0.0008
16.4	0.073 ± 0.006
27.7	0.20 ± 0.02
35.5	0.29 ± 0.02
91.0	0.53 ± 0.01

unaffected by temperature dependent factors such as the dye lifetime. For the rest of the analysis, *the average value of D/D_o is used with its uncertainty representing the standard deviation over the entire temperature range.* (See Table 5.3) The average value of D/D_o for each Gelsil sample is shown in Figure 5.6 as a straight line.

V. Dependence of the diffusion coefficient on the porosity

Figure 5.7a shows D/D_o as a function of the porosity of the Gelsil silica. The first thing to notice about this figure is that D/D_o decreases in a nonlinear fashion as the porosity decreases to a finite value, just as expected for a percolation system. The values for porosity used here are those determined by the nitrogen adsorption experiments.

Because the behavior appears to be percolation-like, a power-law is fit to the data with the form

$$\frac{D}{D_o} = A(\phi - \phi_c)^m, \tag{5.5}$$

with each point weighted by the uncertainty in the value of D/D_o. The uncertainty in ϕ is difficult to determine and its absolute value is assumed to be the same for all values of ϕ.

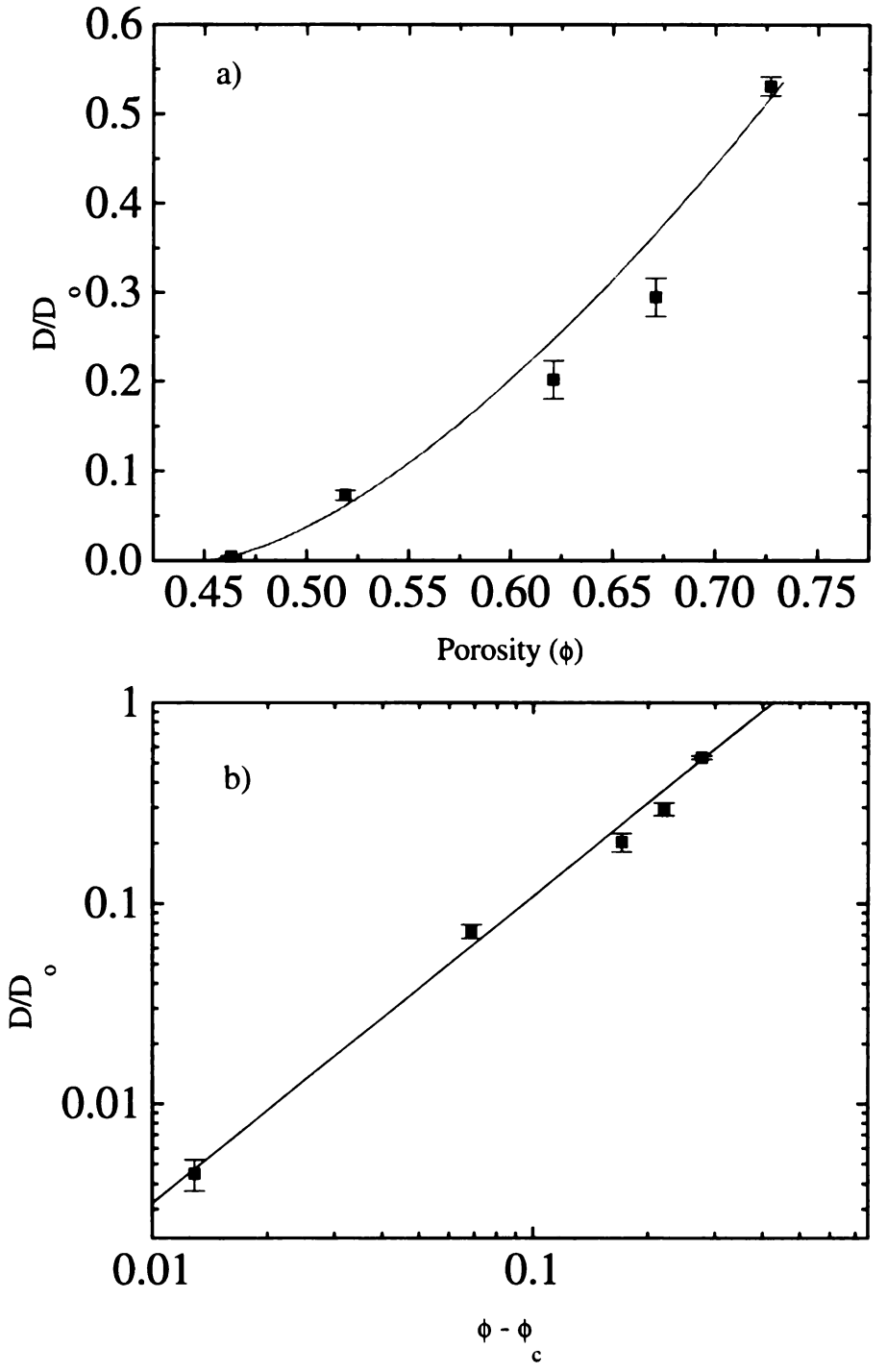

Figure 5.7: (a) D/D_o plotted against the porosity, ϕ, of the Gelsil samples on a linear scale. (b) D/D_o plotted against $\phi - \phi_c$ on a log-log scale. The lines shown are the fit to Equation 5.5. The value for ϕ_c used in (b) is that determined from the fit.

The results of the fit are m = 1.53 ± 0.32, ϕ_c = 0.45 ± 0.01, and A = 3.7 ± 1.4. To view this behavior more clearly, Figure 5.7b plots D/D_o against ϕ - ϕ_c on a log scale along with the power law fit. The range of the data is such that $\frac{\phi - \phi_c}{\phi_c} < 0.3$, suggesting that the data may lie within an asymptotic region near ϕ_c where percolation exponents might apply.[2] It also suggests that the mean field results of the Effective Medium Approximation may not apply in this region.[3]

VI. Dependence of the diffusion coefficient on the pore size

Figure 5.8 plots D/D_o against the average pore radius of the Gelsil silica samples. The striking aspect of the plot is the sharp cutoff seen as the pore size approaches the size of the Methyl Red molecule. Also shown in the figure are two fits to the data, one is a power law (solid line),

(5.6) $D/D_o = B(r_p - R_c)^n$

(with n = 0.49 ± 0.06, R_c = 15.0 ± 0.7 Å, and B = 0.06 ± 0.02), the other is the Renkin equation (Equation 2.10, dashed line),

(5.7) $$\frac{D}{D_o} = F\left(1 - \frac{r_H}{r_p}\right)^2\left(1 - 2.1044\frac{r_H}{r_p} + 2.089\left(\frac{r_H}{r_p}\right)^3 - 0.948\left(\frac{r_H}{r_p}\right)^5\right).$$

Both are fit by weighting each point with the uncertainty in D/D_o, and the Renkin equation has an additional free parameter (F) to adjust the amplitude. As with ϕ, the uncertainty in the average pore radius is difficult to estimate, in part because the value depends upon the model used to determine it. Therefore, while the uncertainty in r_p is significant, it is assumed to be the same for all values of r_p. The fit of the Renkin

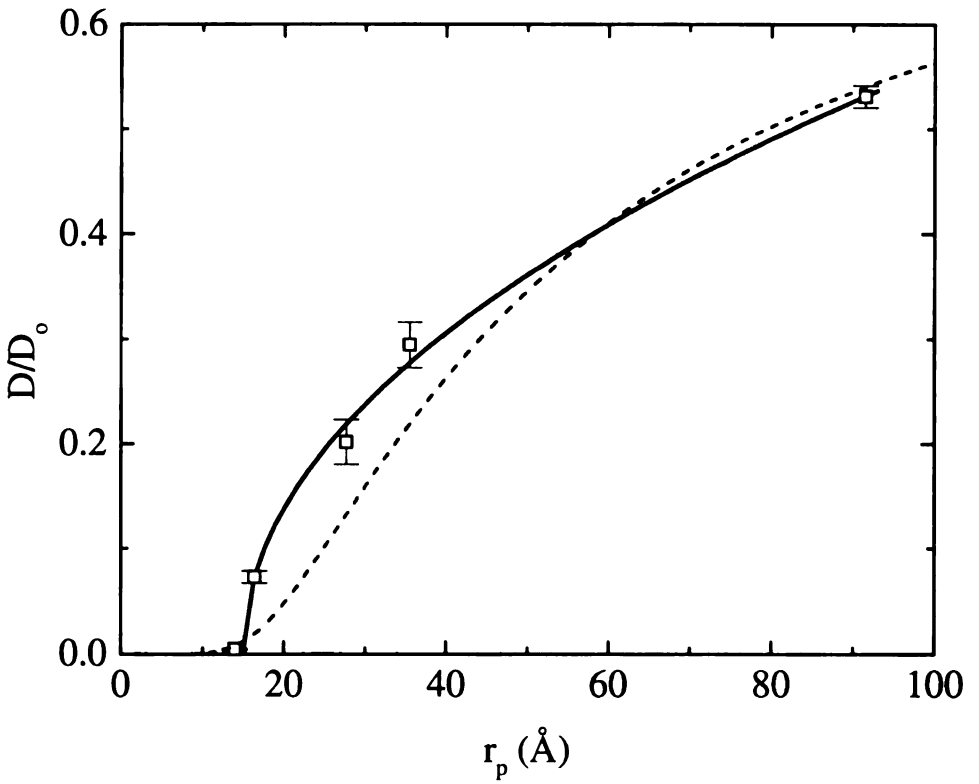

Figure 5.8: D/D_o plotted against the average pore radius of the Gelsil samples. The solid line is the fit to Equation 5.6 and the dotted line is the fit to the Renkin model, Equation 5.7.

equation gives: $r_H = 9.5 \pm 1.1$ Å and $F = 0.9 \pm 0.1$, where r_H should be the effective radius of the solute molecule (here Methyl Red).

The one previous study that can be compared to these results is that of Mitzithras *et al*[4] (discussed in Chapter 2 and shown in Figure 5.9). Their data show remarkably similar behavior with a power law fit of the form of Equation 5.6 over the same range as the Gelsil data ($n_m = 0.54 \pm 0.08$, $R_{cm} = 2.9 \pm 8.1$ Å, and $B_m = 0.06 \pm 0.03$). The only

significant difference is in the critical pore size R_{cm}, which should be smaller in their data, because they measured the diffusion of cyclohexane, a smaller molecule than Methyl Red. This agreement is somewhat surprising, given the very different behavior the Mitzithras data show as a function of porosity (Figure 2.14b). It may be that the structure of the glasses is quite different, but that the average pore size is a very good measure of the diffusive properties of sol-gel glasses.

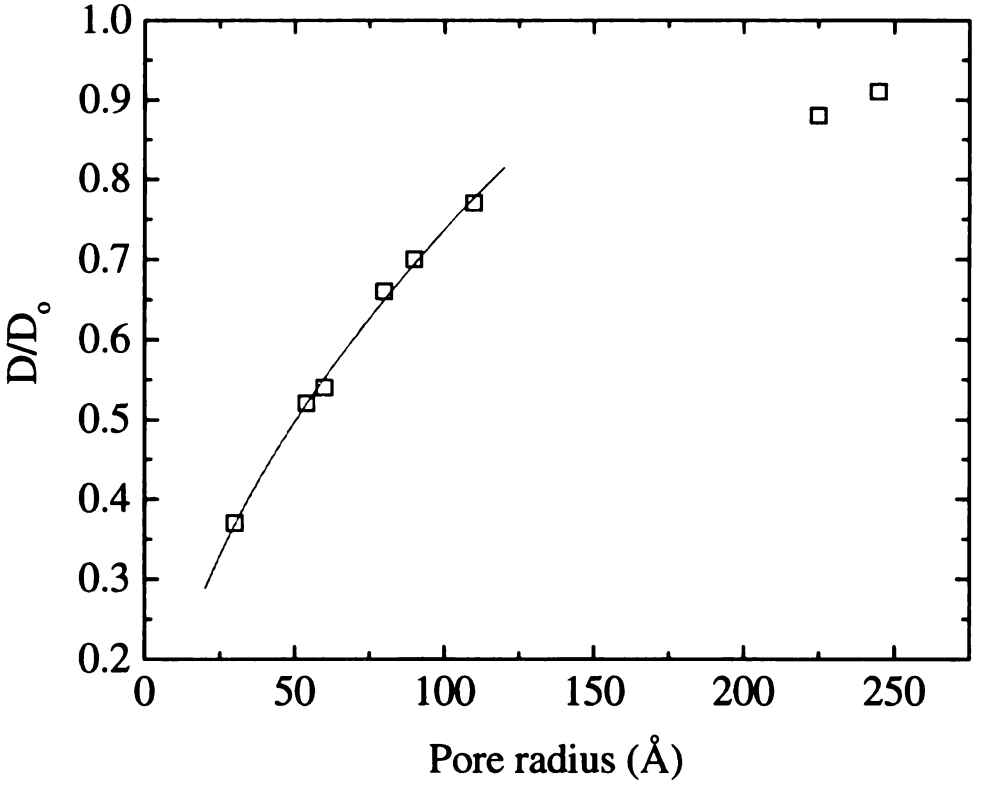

Figure 5.9: D/D_o plotted against the pore radius for the data from Mitzithras *et al*, for cyclohexane diffusing in sol-gel glasses. The line is a fit to Equation 5.6 all but the top two data points. (Data from: A. Mitzithras *et al*, J. Mol. Liq. **54**, 273 (1992).).

VII. Conclusions

There are several different regimes that might be relevant to these measurements. First, we might have expected to find behavior similar to that of Archie's Law ($\sigma \propto \phi^M$) found in rocks, where the percolation threshold is very near $\phi = 0$. This does not describe the behavior in these glasses at all. We might also have expected that the reduced diffusion coefficient is due simply to the narrowing pores, and not necessarily related to some pores becoming inaccessible. In this case, we might expect hydrodynamic models, which are based on this idea, to be appropriate.

The Renkin equation, which is based on the hydrodynamic drag on a large solute molecule flowing down the center of a long cylindrical pore, does not reproduce the behavior found in these glasses (Figure 5.8). This is not surprising, given the disordered structure of the glasses and the fact that the Methyl Red molecule is only slightly larger than the solvent molecules--violating one of the basic assumptions of the model. The effective radius it predicts is consistent with Methyl Red, but given the poor description of the data by the Renkin Equation, should be viewed with caution. This fit shows behavior that is consistent with all the hydrodynamic models, where $\frac{D}{D_o} \rightarrow \left(1 - \frac{r_H}{r_p}\right)^v$, as $r_H \rightarrow r_p$, with $v > 1$. This leads to a gradual decrease in D/D_o as $r_H \rightarrow r_p$, which qualitatively disagrees with this data at small values of r_p. It may be that this model is appropriate for comparison to the data at large r_p only.

As mentioned earlier, the data in Figure 5.7 suggest that a percolation model might be appropriate to describe its behavior. However, it is important to realize how this

system is approaching the percolation threshold. For a network of uniform bonds, the threshold is approached by removing bonds to reduce ϕ (or p). In this case, the bonds that remain are unchanged. The situation is different in the Gelsil materials, where a reduction in ϕ is accompanied by a corresponding reduction in the pore size. How, then, does this type of system approach a percolation threshold? First, consider the case of a material with a distribution of pore sizes about some large average pore radius. If the diffusing molecule is small relative to that average pore size, it will have access to nearly all the interconnected pores and will only be slowed by the hydrodynamic interactions of the fluid and the finite pore size. If the average pore radius is reduced, the lower end of the pore size distribution will begin to overlap significantly with the size of the diffuser. At this point, the smallest pores will become inaccessible to the molecule--effectively removing them from the network. Therefore, in a real material, it is the finite size of the diffusing particle and the distribution of pore sizes which cause the system to approach a percolation threshold as r_p and ϕ are reduced. In contrast, a network of identical pores will either be completely accessible or totally inaccessible to a molecule, depending upon the relative sizes of the molecule and the pores, or if adsorbed molecules block some pores. In that case, there will be no percolation threshold, as the reduction in the diffusion coefficient will be due entirely to the hydrodynamic interactions of the fluid in the pores.

Although we cannot show with certainty that these materials are within the asymptotic region of a percolation threshold, we expect that this system must approach a percolation threshold due to the reasons given above. The behavior of the diffusion

coefficient in this range of ϕ appears to agree with this assumption and so we will assume these systems are near the threshold in order to compare our results with percolation models.

Although uniform bond percolation models describe systems very different from these glasses, continuum percolation models are based on materials with nontrivial relationships between the porosity and the pore radii, and we might expect them to describe the behavior we find. As discussed in Chapter 2 (IIIc), continuum percolation models assign each bond in the network a conductance based upon the size of the pore associated with it. In these models, it is shown that the smallest pores are responsible for the overall transport through the network near the percolation threshold. The continuum model described in Chapter 2, where the bonds on a random, discrete network have a distribution of conductances g given by $P(g) \propto g^{-\alpha}$ (for $g \to 0$), gives rise to the following limits on the continuum conductivity exponent ($\bar{\mu}$) near the percolation threshold (Equation 2.31):

(5.8) $\max(\mu_1 + y, \mu) \leq \bar{\mu} \leq \mu + y$, when $y > 0$ (or $0 < \alpha \leq 1$)

$\bar{\mu} = \mu$, when $y \leq 0$ (or $\alpha \leq 0$)

where $y = \frac{\alpha}{1-\alpha}$, $g = \delta^{y+1}$, δ is the pore width, and $\mu_1 \equiv 1 + (d-2)\nu$ which becomes $\mu_1 = 1.88$ in three dimensions (d = 3, ν = 0.88). Also, recall that μ is the conductivity exponent found in networks with uniform bonds, with an uncertain value ranging from approximately 1.85[5] to 2.0.[6]

We also note that the exponent recovered in a diffusion measurement depends upon how the fluid is distributed in the pores. If the measurement is made with fluid in every cluster of the network, the conductivity exponent, $\bar{\mu}$, should be found. If the measurement only probes fluid on the infinite cluster, the exponent should be $\bar{\mu}$ - β. Because the fluid is placed into these porous silicas after it is manufactured (therefore, after the pore network is formed), it can only reach pores which are connected to the outside surface of the silica. This means that only those pores on the sample spanning cluster are filled with fluid. Any isolated pores cannot be filled. The only exceptions are the negligible volume of pores which make contact to the outside surface but do not connect to any other pores. Therefore, in these glasses percolation theory predicts the diffusion exponent to be $\bar{\mu}$ - β.

In the context of this continuum model, our result of $m = 1.53 \pm 0.32$, implies that a diffusion measurement on the infinite cluster will produce $\bar{\mu} - \beta = 1.53 \pm 0.32$, or $\bar{\mu} = 1.94 \pm 0.32$ (recall that $\beta = 0.41$). Comparing this to Equation 5.8, and assuming that μ = 2.0, we would say that $\alpha \leq 0$ $(y \leq 0)$ in these silicas. This suggests that the distribution of the conductances of the smallest pores does not have a singularity at g = 0.

We should also compare these results to the exponent expected from the "Swiss-cheese" model discussed in Chapter 2. In this specific continuum model, where the solid phase of the porous network is made of overlapping solid spherical particles, Feng *et al.* showed that the distribution of the conductances of the smallest pores obey Equation 5.8 with $\alpha = \frac{1}{3}$ $\left(y = \frac{1}{2}\right)$. This implies that the conductivity exponent, $\bar{\mu}$, should fall

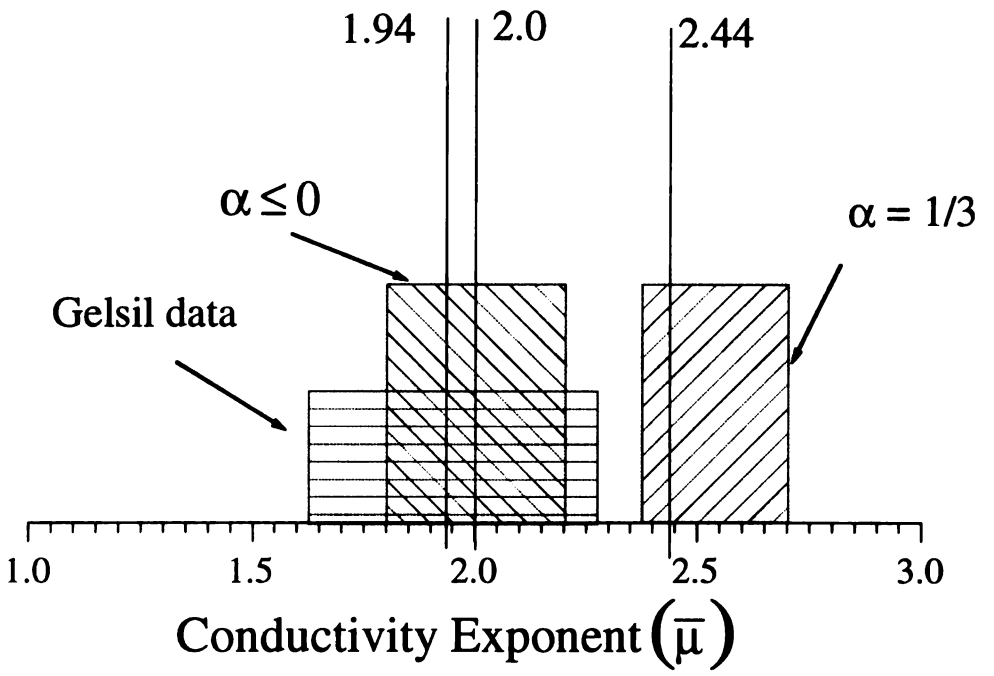

Figure 5.10: Plot showing the range of the uncertainty of the continuum conductivity exponent ($\bar{\mu}$) from the fit to the Gelsil data and for two predictions of the continuum percolation model. ▤: Gelsil data, with $\bar{\mu} = 1.94 \pm 0.32$. ▧: Continuum model with $\alpha \leq 0$, $\bar{\mu} = 2.0 \pm 0.2$. ▨: Continuum model with $\alpha = \frac{1}{3}$, $\bar{\mu} = 2.44\ ^{+0.26}_{-0.06}$.

between the values 2.38 and 2.5. Figure 5.10 illustrates the value and uncertainty of the continuum conductivity exponent ($\bar{\mu}$) found from our data and compares it to the values and estimated uncertainties of the predictions of the continuum models for the cases: $\alpha \leq 0$ and $\alpha = \frac{1}{3}$ (the "Swiss-cheese" result). In this figure, the width of each box signifies the area within the uncertainty of the value of $\bar{\mu}$. The "nominal" value of each is shown as a vertical line. The box corresponding to our data illustrates $\bar{\mu} = 1.94 \pm 0.32$. For these boxes, the value of μ is assumed to be 2.0 ± 0.2, which is an arbitrary

uncertainty based on the range of values found in the literature. Therefore, the $\alpha = 1/3$ box (the "Swiss-cheese" result) has a lower limit of $\mu_1 + y = 2.38$ (because it is larger than the value of μ, see Equation 5.8), and an upper limit of $\mu + y + 0.2 = 2.7$, with 0.2 added to account for the uncertainty in μ. This plot illustrates how our experimental result compares to these two realizations of the continuum model. It appears that our result is more consistent with continuum models with $\alpha \leq 0$ than with the "Swiss-cheese" model. Given the uncertainties, though, we cannot say that the "Swiss-cheese" model is inconsistent with our data (particularly if the "two-sigma" errors are considered, which would show a large overlap between the model and the data). However, the difference between our conductivity exponent and that expected for $\alpha = 1/3$ suggests that these glasses may not have a pore structure like that described by this model, where the pores exist in the gaps between the particles making up the network.

As seen in Chapter 4, the sol-gel process that creates these glasses does appear to form a network of colloidal particles. However, the large porosities found in these glasses suggest that the particles themselves are porous, and a network of porous particles with gaps between the particles would have a bimodal pore size distribution corresponding to the inter- and intra-particle pores, whereas the pore size distributions for the Gelsil glasses have only a single peak. This suggests that as the particles formed a continuous network during gelation, the gaps between the particles filled in with porous silica. All of this strengthens the conclusion that the Gelsil pore network is not like that of the "Swiss-cheese" model.

Finally, if the diffusion coefficient is viewed as simply a function of the average pore radius of this silica we find that, as expected, the diffusion coefficient drops to zero as the pore size approaches the size of the diffusing molecule. But it does so as a power law with an exponent of $\approx \frac{1}{2}$ which has not been previously predicted. The comparison of these results in Gelsil with the results found by Mitzithras suggests that this power law behavior may be common to other sol-gel glasses.

References

[1] M. Ueda *et al*, Chem. Mater. **6**, 1771 (1994).

[2] S. Feng, B.I. Halperin, and P.N. Sen, Phys. Rev. B **35**, 197 (1987).

[3] M. Sahimi *et al*, Phys. Rev. B **28**, 307 (1983), Figure 3.

[4] A. Mitzithras, F.M. Coveney, and J.H. Strange, J. Mol. Liq. **54**, 273 (1992).

[5] A.B. Harris, Phys. Rev. B **28**, 2614 (1983).

[6] D. Stauffer and A. Aharony, *Introduction to Percolation Theory*, (Taylor and Francis, London, 1994), p. 52.

Chapter 6

DIFFUSION IN OTHER POROUS SILICAS

I. Vycor

Following procedures similar to those used for Gelsil glasses, Vycor 7930 porous glass was first soaked in water and NaOH before placing it in the Methyl Red/glycerol/water mixture. If the glass was not soaked in NaOH long enough, a red stain could be seen in the glass and a double exponential decay was found for all values of Λ. The signal became a single exponential decay by simply allowing the glass to soak in the solution of NaOH and water for a longer period of time to place more Na^+ ions in the pores and remove the red color. The FRS decay rates from the sample, plotted against q^2, are shown in Figure 6.1.

The normalized diffusion coefficient at 22.2 °C in this glass is $D/D_o = 0.10 \pm 0.01$, where $D = 4.4 \pm 0.5 \times 10^{-9}$ cm^2/s and $D_o = 4.37 \pm 0.02 \times 10^{-8}$ cm^2/s. Table 6.1 compares this to the results of other diffusion measurements in the same glass.

Table 6.1: The normalized diffusion coefficient in Vycor 7930 porous glass compared to previous measurements. The study by Guo *et al.*[1] was made with DLS using polystyrene (molecular weight 2500) as the tracer and fluorobenzene as the fluid. Dozier *et al.*[2] made their measurements using FRS with azobenzene as the tracer and (1) methanol/toluene or (2) 1-propanol/toluene as the fluid.

	Porosity	Pore Radius (Å)	D/D_o
This study	0.36	24.5 Å	0.10 ± 0.01
Guo *et al*	0.28	20 Å	0.105 ± 0.006
Dozier *et al* (fluid 1)	0.28	30 Å	0.010 ± 0.003
Dozier *et al* (fluid 2)	0.28	30 Å	0.026 ± 0.007

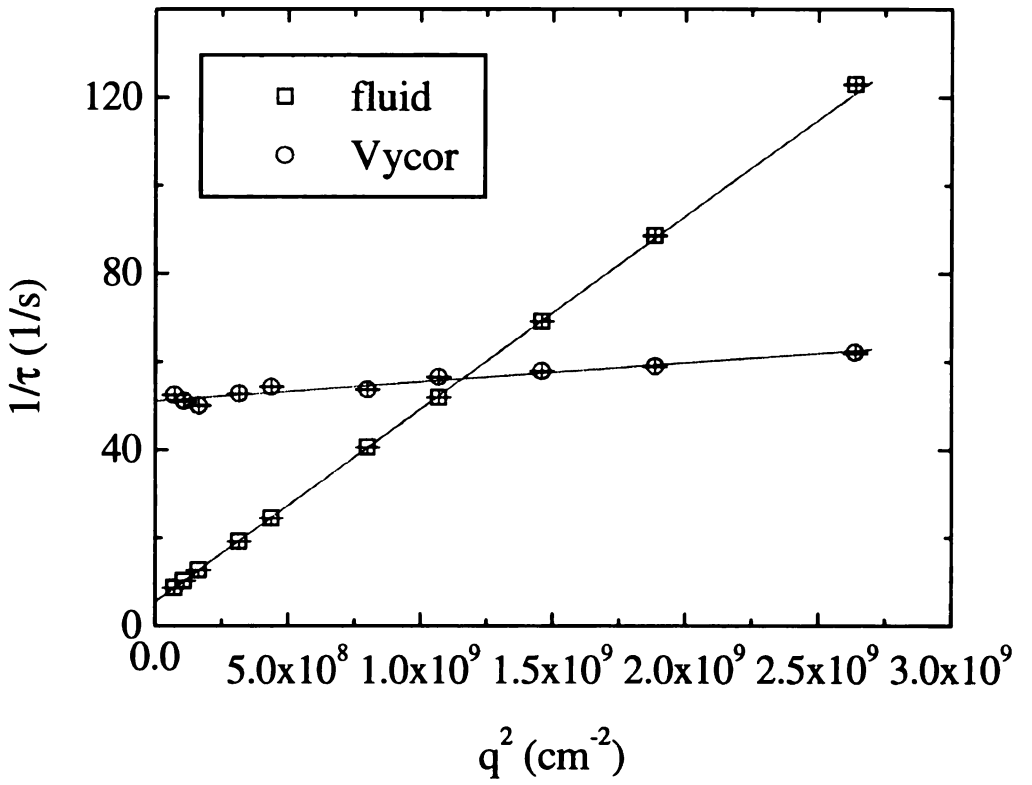

Figure 6.1: The FRS decay rate ($1/\tau$) vs. q^2 in the free fluid and within the Vycor porous glass at 22.2 °C. Also shown as solid lines are the fits using Equation 5.2. Here $D_o = 4.37 \pm 0.01 \times 10^{-8}$ cm^2/s and $D = 4.4 \pm 0.5 \times 10^{-9}$ cm^2/s.

Our results are very similar to those of Guo *et al.*, but differ considerably from that found by Dozier *et al.* Given that Methyl Red has a molecular weight of 270, and is similar in size and shape to azobenzene (molecular weight 182), these results are rather surprising. The polystyrene used in the DLS study has a hydrodynamic radius (calculated from Equation 2.9) of 13 Å while Methyl Red in the glycerol/water solution used in this study has a calculated radius of roughly 4 Å (assuming a viscosity of ~200 centipoise, T =

295.5 K, and $D_o = 2.4 \times 10^{-8}$ cm^2/s in the free fluid). By comparison, azobenzene in the alcohol/toluene fluids used by Dozier *et al.*, has a hydrodynamic radius of approximately 3 Å.[3]

Guo *et al.* speculated that the difference between their results and those of Dozier *et al.* may have been due to residual binding sites that remained on the surface of the Vycor that Dozier *et al.* treated in boiling 1-propanol. These remaining sites would then reduce the observed diffusion coefficient, resulting in the surprising low values found in that experiment. Guo *et al.* also state that they briefly examined the diffusion of azobenzene in their hexamethyldisilazane treated Vycor glass, and found that the diffusion was occurring faster than they could measure. This is very surprising, because the diffusion coefficient of azobenzene and Methyl Red in solvents such as methanol/toluene, 1-propanol/toluene, benzene, ethanol, and 2-propanol is in the range of 1×10^{-6} to 1×10^{-5} cm^2/s, which is easily measurable.[4] It is hard to explain why azobenzene in Vycor would diffuse faster than that.

II. Ludox glasses

As a result of the heat treatment of the AS-40 glasses to remove most of the hydroxyl sites on the surface and the "native" Na in the HS-40 glasses, it was unnecessary to presoak these samples in the NaOH/water solution. When placed in the Methyl Red/glycerol/water mixture, the fluid entering the pores did not turn red in the HS-40 glasses, while in the AS-40 glasses the fluid turned faintly red before sufficient Na^+ ions entered the pores from the bulk fluid and blocked the remaining binding sites on the surface to return the fluid to its original color.

Non-single exponential decays of the diffracted intensity found in the 0.088M NH_4Cl gel appeared to be due to free fluid trapped between the curved surface of the sample and the window because simply translating the beams to a region closer to the sample edge (where the sample had to touch the window) produced single exponential behavior. The non-single exponential signal in the 0.149M NH_4Cl sample disappeared after the sample was soaked in the Methyl Red/glycerol/water solution for several more days, to allow time for more Na^+ to enter the pores. However, in both samples, the normalized diffusion coefficient, D/D_o, found from the single exponential decays was the same as that found from the non-single exponential decays. (The values of D/D_o in the double exponential and single exponential cases were, respectively, 0.259 and 0.258 ± 0.004 in the 0.088M sample and 0.26 and 0.265 ± 0.011 in the 0.149M sample.) This is a strong verification that the correct diffusive behavior can be recovered even when an additional signal is present in the FRS experiment.

Figures 6.2 and 6.3 show the FRS decay rates vs. q^2 in the free fluid and within the seven Ludox samples taken at 22.2°C. Table 6.2 lists the values of D/D_o derived from this data. D/D_o appears to depend strongly on the salt concentration used in the

Table 6.2: Values of D/D_o in the seven gelled Ludox samples. All the data was taken at 22.2 °C.

Molarity of salt when gelled	AS-40 Ludox D/D_o	HS-40 Ludox D/D_o
0.290 M	0.46 ± 0.01	0.457 ± 0.003
0.149 M	0.265 ± 0.011	0.537 ± 0.007
0.088 M	0.258 ± 0.004	0.318 ± 0.002
0 M	----	0.197 ± 0.003

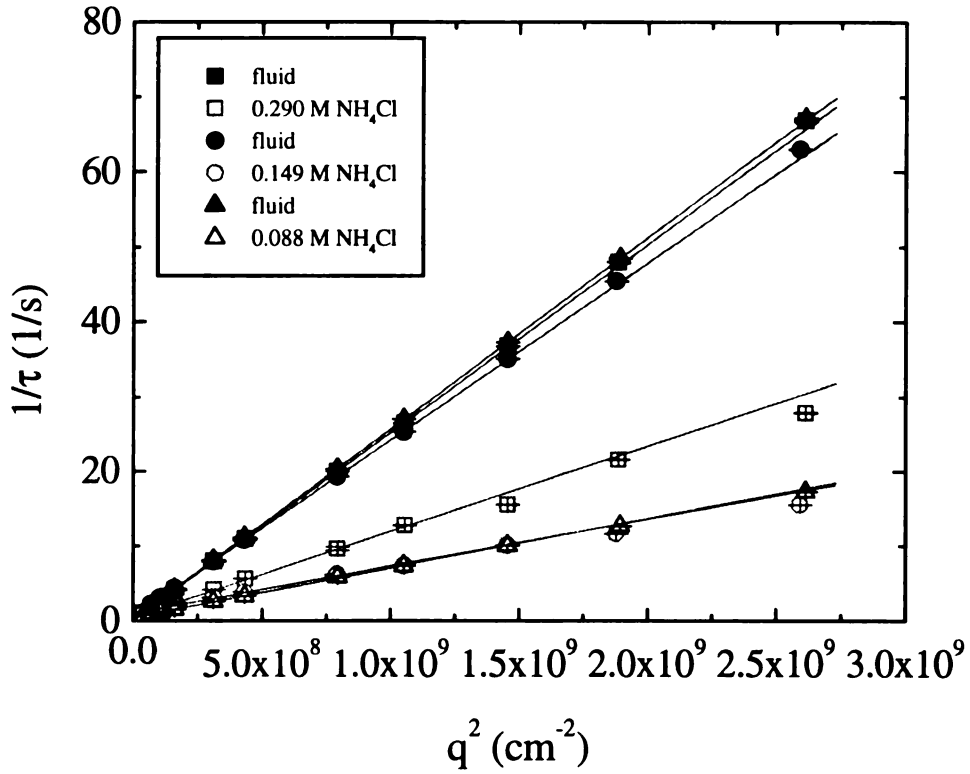

Figure 6.2: The FRS decay rate ($1/\tau$) vs. q^2 in the free fluid and within the three AS-40 Ludox porous glasses at 22.2 °C. Also shown as solid lines are the fits to Equation 5.2.

liquid to make the initial gel, which also determined the time it took to gel the silica. However, the 0.149 M NaCl HS-40 sample does not follow this trend, just as it showed very different behavior in the nitrogen adsorption results in Chapter 4. In the following section we will examine how these data depend upon the porosity and pore size of these glasses and how they compare to the Gelsil samples discussed in the previous chapter.

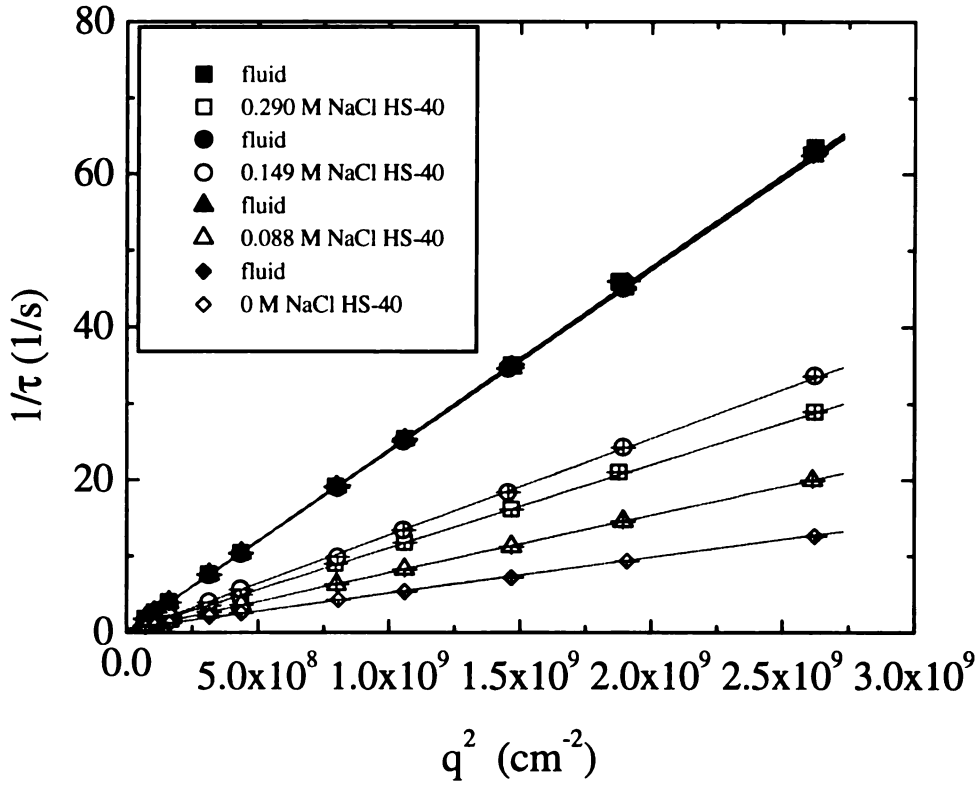

Figure 6.3: The FRS decay rate ($1/\tau$) vs. q^2 in the free fluid and within the four HS-40 Ludox porous glasses at 22.2 °C. Also shown as solid lines are the fits to Equation 5.2.

III. Comparison with the Gelsil data

Figure 6.4 plots D/D_o vs. porosity and pore radius for the Gelsil data along with the Vycor and Ludox samples. These plots graphically illustrate the difference between the sol-gel grown Gelsil glasses and the others. Gelsil has a much higher porosity than the other glasses, even though the average pore radius is the same or less. This indicates that the geometry of the pore networks must be very different.

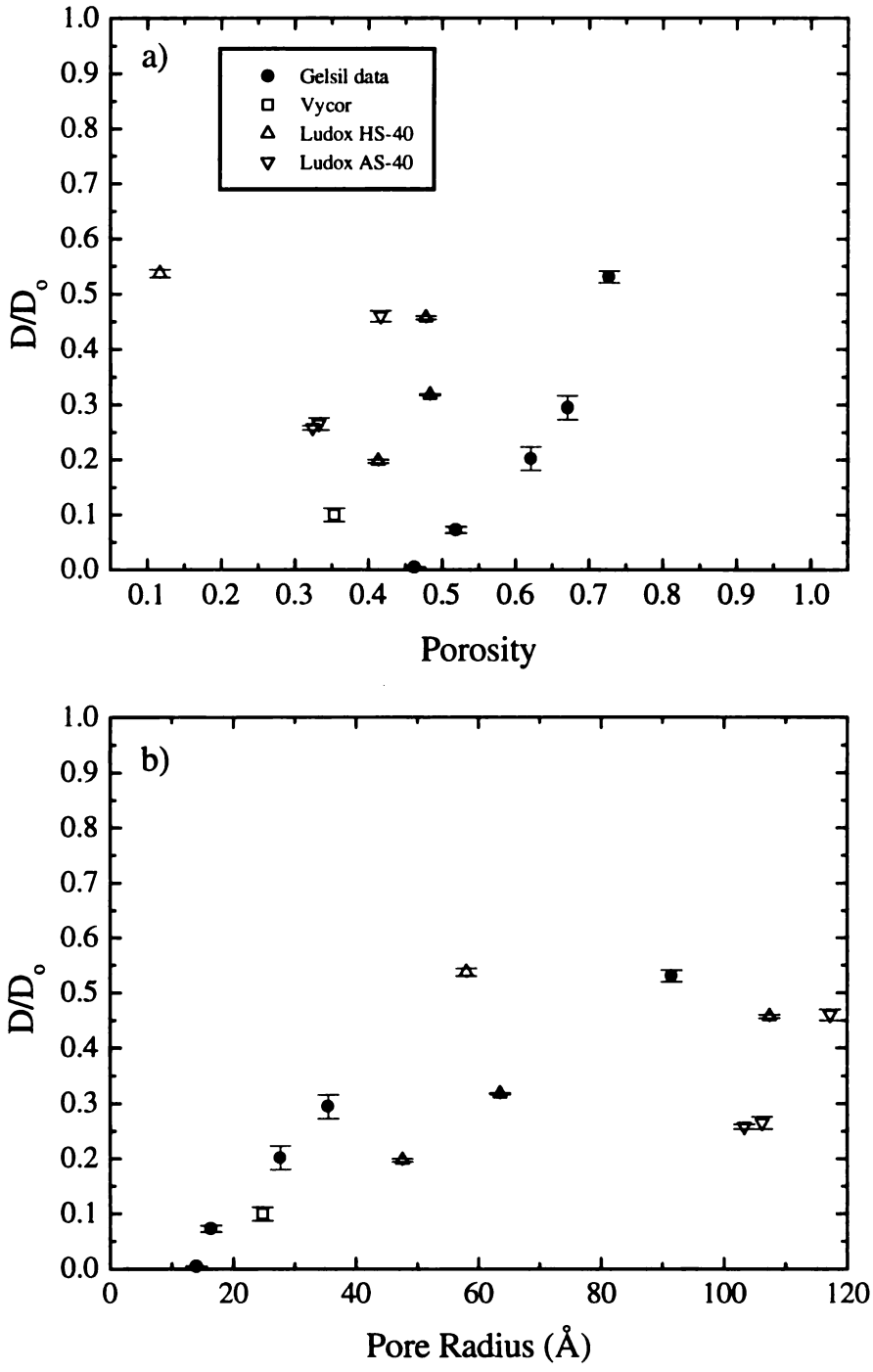

Figure 6.4: D/D_o in all the samples of this study as a function of (a) the porosity and (b) the pore radius.

First comparing Vycor to the Gelsil, we see from Figure 6.4a that the Vycor point does not fall along the curve formed by the Gelsil data as a function of porosity, but that in Figure 6.4b, the point is close to the Gelsil curve as a function of pore radius. Taken by itself, this might indicate that for two different pore geometries (both with narrow pore size distributions), the pore radius is a better predictor of the diffusion coefficient than the porosity. However, with only one point, that is purely speculation.

Looking at the Ludox data, we see that the 0.149 M NaCl HS-40 ($D/D_o = 0.54$, $\phi = 0.12$, and $R_p = 58$ Å) sample does not behave like any of the other samples, most likely for the reasons discussed in Chapter 4. That data point will be ignored for the rest of this discussion. The Ludox samples group themselves with respect to the Gelsil data in a fashion that seems to follow the relative sizes of the particles that make up the glass. The progression of the data is $\phi_{AS\text{-}40} < \phi_{HS\text{-}40} < \phi_{Gelsil}$, and $R_{p\ AS\text{-}40} > R_{p\ HS\text{-}40} > R_{p\ Gelsil}$. From Table 4.3, we know that HS-40 is made of 12 nm diameter silica particles and AS-40 is made from 22 nm particles, while the Gelsil is made from initially molecular-sized silica particles, though they grow to larger sizes before the continuous network forms (Figure 4.7). It is no surprise, then, that the AS-40 glasses have the lowest porosities and the largest pore sizes of these glasses, since they are made from larger particles. Also, the AS-40 glasses were subjected to a higher temperature than the other glasses, so some of the small pores may have been closed off, which would lead to an increase in the average pore size and a decrease in the porosity. This also indicates that the particles making up the Gelsil glasses are likely to be porous in order for those samples to have such large porosities.

The normalized diffusion coefficient in the AS-40 glasses decreases with porosity and pore radius, but the range of the data is too small to determine if it behaves with the same functionality as the Gelsil data. The porosity dependence of the diffusion coefficient in the HS-40 samples is similar to the AS-40 data, but again covers too small a range and has too much scatter to quantitatively compare it with the Gelsil. The pore size dependence, however, appears to follow the shape of the Gelsil data quite closely. If the data are fit to a curve of the form of Equation 5.7:

(5.7) $D/D_o = 0.06*(r_p - R_c)^n$

where the prefactor is arbitrarily set to 0.06, because that was the value found with the fits to the Gelsil and Mitzithras data (Chapter 5), the result is $n = 0.48 \pm 0.02$ and $R_c = 33 \pm 5$ Å. This larger value of R_c might be due to the apparently wider pore size distributions of the Ludox glasses. As discussed previously, the percolation threshold is approached because pores smaller than the diffuser's size are effectively removed from the network. For a given diffuser and average pore radius, a network with a wide distribution will have more pores excluded than a network with a narrow distribution. Therefore, a network with a wider distribution will be "closer" to the percolation threshold and the "critical" average pore radius (R_c) will then be larger. However, this result from the Ludox data is based on too few data points to be considered anything but qualitative.

IV. Conclusions

These comparisons between the four different types of glasses show that while the normalized diffusion coefficient depends upon both the porosity and the pore size, neither of these parameters alone can be used to predict the diffusive behavior of a fluid in a pore

network. These glasses seem to group themselves in the following manner. Vycor , with its small porosity, small pore size, and narrow pore size distribution must have a pore structure unlike the others. The Ludox glasses, with small porosities, large pore sizes, and relatively large pore size distributions may be good candidates for comparison to "Swiss-cheese"-like models because they are made from presumably solid colloidal particles. The sol-gel Gelsil glasses have large porosities, easily varied pore sizes, but with relatively narrow pore size distributions which make them distinctly different from the Ludox glasses, even though both are made from colloidal silica particles. The large porosities of the Gelsil indicate that the particles in those glasses are actually porous, which would also help explain why the pore distribution in so narrow.

The results in these different glasses make it clear that the details of the pore structure affect the diffusive behavior of fluids in the pores. Because the pore size distribution appears to be responsible for the percolation behavior in these systems, it seems likely that a detailed knowledge of the pore size distribution of a glass, along with its porosity and average pore size, is necessary to describe the diffusion of a fluid whose molecular size is close to the size of the pores.

References

[1] Y. Guo, K.H. Langley, and F.E. Karasz, Phys. Rev. B **50**, 3400 (1994).

[2] W.D. Dozier, J.M. Drake, and J. Klafter, Phys. Rev. Lett. **56**, 197 (1986).

[3] Y. Guo, K.H. Langley, and F.E. Karasz, ibid.

[4] M. Terzima, K. Okamoto, and N. Hirota, J. Phys. Chem. **97**, 5188 (1993).

Chapter 7

SUMMARY AND FUTURE DIRECTIONS

In this work, fluid diffusion within porous silica has been studied to determine how parameters such as the porosity and average pore size affect the diffusion. We have used a holographic optical technique to measure diffusion on length scales much larger that the size of the pores in order to examine the "normal" diffusion through the entire network rather than the anomalous diffusion found on the length scale of the pore size.

In one particular set of porous glasses, we have found that the normalized diffusion coefficient varies with the porosity of the glass as: $\frac{D}{D_o} \propto (\phi - \phi_c)^{1.5}$ and with the average pore radius as $\frac{D}{D_o} \propto (R_p - R_c)^{0.49}$. As expected, these results do not agree with hydrodynamic models of media with uniform nonintersecting pores, but we have shown that these results are consistent with the prediction of continuum models of percolation for diffusion on the percolating cluster of a network. This is the first time this power-law behavior has been found in an experimental study of fluid diffusion. These glasses appear not to behave in accordance with the "Swiss-cheese" model, where the distribution of conductances for the smallest pores contains a singularity at zero conductance, although our data cannot exclude this model completely. The difference between these sol-gel glasses and the "Swiss-cheese" model can be seen by their relatively large porosities, which indicate that the particles making up the network are porous, unlike the solid particles that are assumed in the model.

Comparisons with porous silicas made through different processes verifies the importance of the pore size distribution on the fluid diffusion. These systems approach the percolation threshold because the diffusing molecule cannot pass through pores that are smaller than it is. By comparing glasses with relatively narrow pore distributions to glasses with wider pore distributions we find that, as expected, the latter are closer to the percolation threshold and therefore have smaller diffusion coefficients than glasses with narrower distributions--leading to a larger value for R_c.

The importance of the width of the pore size distribution on the transport properties in porous materials makes this a ripe area for further investigation. The creation of materials with controlled pore size distributions should make it possible to probe the crossover from "Swiss-cheese" behavior to that found in this work. Such a study may also provide insight into whether knowledge of the width of the pore distribution, along with the porosity and the average pore size, can provide a prediction of the diffusive behavior in pore networks. Also, a study of the conductivity and permeability of the Gelsil glasses should be carried out in order to compare those results with the diffusion measurements in this study.

An additional line of research could systematically vary the size and shape of the probe molecule to determine how that parameter affects the percolation thresholds ϕ_c and R_c. This may be somewhat difficult to achieve, given the restrictions on the properties of a probe molecule in these experiments. A related study could use molecules of different size to modify the surface structure of the pores. This can provide a way to vary the pore

size and porosity in a controlled fashion, although it will also alter the connectivity of the pore network.

Finally, the color change of Methyl Red could be used to perform a very simple measurement of the diffusion of the Na^+ ion through a porous material. As seen in this study, Methyl Red turns red in the pores of an untreated silica, so if a sample were filled with Methyl Red in water, and then a known quantity of Na^+ were added to the surrounding fluid, the boundary of the color change could be monitored to measure the diffusion of the ions into the pores. In fact, with this dye and two immiscible fluids, it would be possible to monitor the phenomenon of "viscous fingering" as one fluid containing the dye displaces the other in the pore network.[1]

References

[1] U. Oxaal *et al*, Nature **329**, 32 (1987).

Appendices

Appendix A

Appendix A

ABSORPTION MEASUREMENTS

The absorbance measurements made in this study were carried out with an Acton Research Corporation SpectraPro 300i 300mm focal length scanning monochromator with an attached SC-447 sample chamber. Figure A.1 is a schematic drawing of the sample chamber showing how it is set up for a transient absorption measurement. An absorbance spectra is made by illuminating the sample (in a 0.2 or 0.5 mm path length cell) with light from a 30W tungsten halogen light. The transmitted light is imaged onto the entrance slit of the monochromator which is scanned over the wavelength range of interest. The light is detected by a photomultiplier tube (PMT) attached to the exit slit of the monochromator, and the data is collected on a computer which is interfaced to both the detector and the monochromator. The spectral output of the lamp, the response of the monochromator, and the reflection off the sample cell faces are corrected for by taking a spectra of the same sample cell filled with only glycerol. The absorbance (A) is calculated from Lambert-Beer's Law: $A(\lambda) = \log(I_o(\lambda)/I_d(\lambda))$ where $I_o(\lambda)$ is the incident light intensity at wavelength λ and $I_d(\lambda)$ is the transmitted light intensity at λ. Here, $I_o(\lambda)$ is the intensity through the glycerol-filled cell.

For the transient absorption measurements, an excitation source is needed to excite the dye in the cell. This is accomplished with the 488nm line of an Ar^+ laser. In addition to passing through a shutter to control the length of the excitation pulse, the beam is expanded with a lens to assure that it illuminates all of the sample that is probed by the white light plus the surrounding region. This is necessary to prevent molecules not

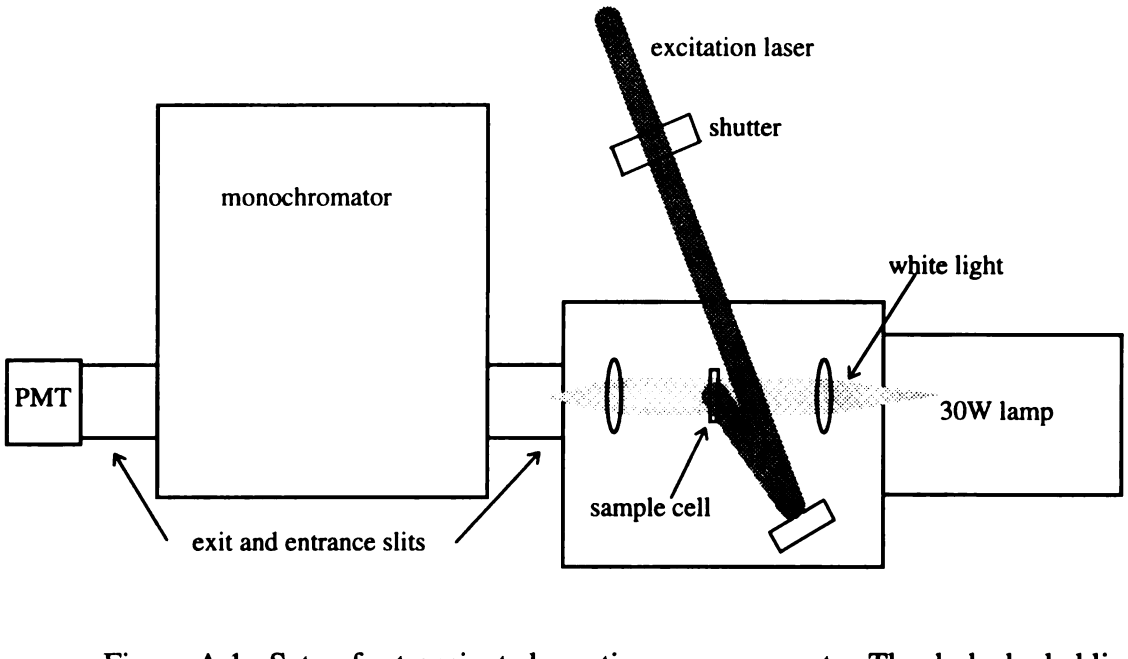

Figure A.1: Setup for transient absorption measurements. The dark shaded line is the excitation laser, the light shaded line is the white light from the lamp, and the PMT is the photomultiplier tube attached to the exit slit of the monochromator.

excited by the laser from entering the probed region and affecting the lifetime measurement. In practice, the beam is expanded to cover the entire sample. For these measurements, the monochromator remains set at one wavelength and the intensity of the transmitted light is monitored over time. After the excitation pulse ends, the time dependence of the transmitted intensity can be used to determine the dye lifetime.

Appendix B

Appendix B

DATA ACQUISITION AND ANALYSIS PROGRAMS

The program used to control the shutter controller, the Stanford Research Systems preamplifier, and the digital oscilloscope is listed on the following pages. It was written in C++ in Borland C++, v. 4.5.

The format of the data files is as follows (shown on the following page). An ASCII header containing the equipment settings occupies the first 24 lines. The next five lines contain the values needed to convert the raw data (in integer form) to the real number values in the form of x(t), y(V). The rest of the values are integers corresponding to the voltage level of the oscilloscope at each point. The header itself describes the conversion in detail. One irregularity is the value of the "# of averages" field. Because the LeCroy 9400A oscilloscope does not output this value, the value entered is the maximum number of averages allowed during that data acquisition.

If the data is analyzed with Microcal Origin, the following script file can be used to convert the data file into an Origin worksheet:

```
offsetall=%H_a[1];                  {*These 5 lines copy the first five*}
prefix=%H_a[2];                     {*values used to convert the remaining*}
tpoint=%H_a[3];                     {*integer data to useful numbers.*}
delay=%H_a[4];
numpoints=%H_a[5];

mark-d %H_a -b 1 -e 5;              {*deletes the just copied 5 values*}

%H_b= prefix*( (%H_a-32768)/8192 -offsetall);     {*creates the voltage*}
                                                  {*data in column B*}
%H_a=data(0,numpoints-1,1);         {*Creates column A, then converts*}
%H_a=(%H_a*tpoint)-delay;           {*it into the correct time values.*}
```

Data file header:

Data taken with LeCroy 9400A, and SR560 preamp.
c:\users\lowell\data\gelsil\gsn21607.txt
Data taken on: November 21, 1996
Number of points saved: 2500
scopetimebase: .05 s/DIV
# of averages: 200
trigger level: 0.08 V
scope delay: 10 % fullscale
scopevertscale: .9 V/DIV
scopeoffset: -2.8 V
trigchannel: EX
preampgain: 20000
preampfilter mode: 2
High pass freq: 300 Hz
low pass freq: 30000 Hz
To convert data to volts:
y(V) = prefix*{ (data[i]-32768)/8192 -offsetall}
To convert x=0,1,2,3... to time scale:
x(t) = (x*tpoint)-delay
(1st data value:) y scale offset (offsetall):
(2nd data value:)y scale multiplier (prefix):
(3rd data value:)time per point (tpoint):
(4th data value:)trigger time delay (delay):
(5th data value:)number of points (numpoints):
-2.8
0.900901
0.0002
0.05
2500
4198
3864
4134
4108
4326
3992
4210
4070
.
.
.
.

```
////////////////////////////////////////////////////////////////////////
//
//              LeCroy94.cpp
//              For the control of LeCroy 9400A oscilloscope, SRS 560 Low Noise
//                      preamplifier and Uniblitz T132 shutter driver.
////////////////////////////////////////////////////////////////////////
//              9/6/97  Added lines to correctly import scope delay time when the
//                      ScopeDelayTime value is set <0.
//              12/12/96  Removed Dual grid display.  Fix (again) the saving routine
//                      so that the origin script in lec94tmp.otw will work.
//              10/21/96  "Totally" working:  save only integer values of data--must
//                      must convert externally.
//              10/19/96  Created from LeCroy2.cpp
//                      Change to control LeCroy 9400A scope
//              9/19/96  Modified:  don't save last point (buff-1)
//                      label all saved parameters
//                      only save y, not x,y pair
//              9/7/96  Modified:  change x[],y[], to x,y in savedata()
//                      change "abort" message box in getdata()
//                      change max memory to 2500000, but only can seem
//                      to get 25000 without a GPF
//              8/26/96 Modified from scope02, Now controls 9310AM scope.
//              7/13/96 Modified--got the SR560 command (and sr560.h) working.
//              7/11/96 Modified from scope2.  Add functions for HP54600b and
//                      SR560 Low Noise preamp.  Remove SR850 functions.
///             4/22/96: add dialog box for changing filename before saving
//                      Needs no .def, .rc, or any special library (besides gpib)
//              Modified:4/20/96:reliable preamble extraction
//                      add .ini support
//              Modified: 4/18/96-4/19/96:  Add SR850 controls.
//
////////////////////////////////////////////////////////////////////////
//              Modified from scope1.cpp, Now use Edit boxes.
//              Control of HP54600b Oscope
//              Opening and closing the shutter using buttons in main window.
//              written:4/11/96
////////////////////////////////////////////////////////////////////////

//includes for windows stuff
#include <owl\applicat.h>
#include <owl/framewin.h>
#include <owl\edit.h>
#include <owl\inputdia.h>  //For input dialog boxes
//              Also need ...bc45\include\owl\inputdia.rh  ?
//                      ...bc45\include\owl\inputdia.rc  ?
```

```
//                      IDD_INPUTDIALOG          ?
//              added to the scope1.rc in the project
//              4/18/95-removed all input dialog boxes in favor of Edit boxes.
#include <owl/button.h>
#include <owl/static.h>
#include <string.h>
#include <stdio.h>    //need for sprintf function ?
#include <iostream.h>
#include <fstream.h>
//#include <math.h>
//#include <ctype.h>
#include "c:\bc45\include\classlib\date.h"

#include "shutter.h"          //include function for sending commands to shutter
#include <windecl.h>          //include GPIB commands
#include "SR560.h"            //include function for sending COM2 commands to
                              //              SR560 Low Noise preamp

//definitions for whole program
#define IDB_OPEN 64
#define IDB_CLOSE 65
#define IDB_TRIGGER 66
#define IDB_RESET 67

#define IDB_SCOPERUN 101
#define IDB_SCOPECLEAR 102
#define IDB_SCOPESTOP 103
#define IDB_SCOPEDELAY 104
#define IDB_SCOPEGETDATA 105
#define IDB_SCOPERESET 106
#define IDB_SCOPEUPDATE 107
#define IDB_SR560UPDATE 108

#define IDE_FILENAME 201
#define IDE_SCOPETIMEBASE 202
#define IDE_SCOPEAVER 203
#define IDE_SCOPETRIG 204
#define IDE_SCOPEDELAYTIME 205
#define IDE_SCOPEVERTSCALE 206
#define IDE_ERRORBOX 207
#define IDE_SCOPEOFFSET 208
#define IDE_SCOPETRIGCHAN 209
#define IDE_SCOPENUMPOINTS 210

#define IDE_SR560GAIN 301
```

```
#define IDE_SR560FILTERMODE 302
#define IDE_SR560HIFREQFILTER 303
#define IDE_SR560LOFREQFILTER 304


int shutter(const int&);
void sr560 (const char*);
int lec9400a=0;

class TShutWin        : public TWindow
{
        public:
                TShutWin(TWindow* parent=0);
                virtual BOOL CanClose();
                int savedata(int*,long int,unsigned int*,char* );
                void send(char *cmd);


        protected:
                void CmOpen();
                void CmClose();
                void CmTrigger();
                void CmReset();
                void CmScopeGetData();
                void CmScopeReset();
                void CmScopeStop();
                void CmScopeClear();
                void CmScopeRun();
                void CmScopeUpdate();
                void CmSr560Update();

        private:
                TEdit *filename;
                TEdit *ScopeTimeBase;
                TEdit *ScopeAver;
                TEdit *ScopeTrig;
                TEdit *ScopeDelayTime;
                TEdit *ScopeVertScale;
                TEdit *ErrorBox;
                TEdit *ScopeOffset;
                TEdit *ScopeTrigChan;
                TEdit *ScopeNumPoints;
                TEdit *Sr560Gain;
                TEdit *Sr560FilterMode;
                TEdit *Sr560HiFreqFilter;
```

```
        TEdit *Sr560LoFreqFilter;


        char*  get_info(TEdit* edit);


        DECLARE_RESPONSE_TABLE(TShutWin);
};


DEFINE_RESPONSE_TABLE1(TShutWin,TWindow)
    EV_BN_CLICKED(IDB_OPEN,CmOpen),
    EV_BN_CLICKED(IDB_CLOSE,CmClose),
    EV_BN_CLICKED(IDB_TRIGGER,CmTrigger),
    EV_BN_CLICKED(IDB_RESET,CmReset),
    EV_BN_CLICKED(IDB_SCOPEGETDATA,CmScopeGetData),
    EV_BN_CLICKED(IDB_SCOPERESET,CmScopeReset),
    EV_BN_CLICKED(IDB_SCOPESTOP,CmScopeStop),
    EV_BN_CLICKED(IDB_SCOPECLEAR,CmScopeClear),
    EV_BN_CLICKED(IDB_SCOPERUN,CmScopeRun),
    EV_BN_CLICKED(IDB_SCOPEUPDATE,CmScopeUpdate),
    EV_BN_CLICKED(IDB_SR560UPDATE,CmSr560Update),


END_RESPONSE_TABLE;


TShutWin::TShutWin(TWindow* parent)
{//Constructor
    Init(parent,0,0);

//Uniblitz text and buttons

        int x=600,y=650, space=90, w=80,h=40;
    new TStatic(this,-1,"Uniblitz T132 Shutter Driver/Timer Controller",
                                                    x,y-20,400,20);
        new TButton(this,IDB_OPEN,"Open",x,y,w,h);
        new TButton(this,IDB_CLOSE,"Close",x+space,y,w,h);
        new TButton(this,IDB_TRIGGER,"Trigger",x+2*space,y,w,h);
        new TButton(this,IDB_RESET,"Reset",x+3*space,y,w,h);

//lec9400a scope text, buttons and edit boxes

    new TStatic(this,-1,"LeCroy 9400A Oscilloscope",140,20,400,20);
```

```
        x=70,y=70, space=50, w=100,h=40;

        new TButton(this,IDB_SCOPERESET,"Reset",x,y,w,h);
        new TButton(this,IDB_SCOPESTOP,"Stop",x,y+1*space,w,h);
        new TButton(this,IDB_SCOPECLEAR,"Clear",x,y+2*space,w,h);
        new TButton(this,IDB_SCOPERUN,"Run",x,y+3*space,w,h);
        new TButton(this,IDB_SCOPEGETDATA,"Get Data",20,305,120,120);

        x=220,y=65,w=200,h=20,space=50;
new TStatic(this,-1,"Filename for data:",x,y,w,h);
new TStatic(this,-1,"Time Base
                        (s/DIV):(50,100,200,500ns...100s)",x,y+space,w+300,h);
new TStatic(this,-1,"#of Averages (10,20,50,..1M):",x,y+2*space,w,h);
new TStatic(this,-1,"Trigger level (V):",x,y+3*space,w,h);
new TStatic(this,-1,"Delay time (% >0, s <0):",x,y+4*space,w,h);
new TStatic(this,-1,"Channel 1 (V/DIV):",x,y+5*space,w,h);
new TStatic(this,-1,"Vertical Offset (V):",x,y+6*space,w,h);
new TStatic(this,-1,"Trigger channel (C1,C2,EX,LINE):",x,y+7*space,w+300,h);
new TStatic(this,-1,"# of points:
                        (50,100,250,500...25000)",x,y+8*space,w+300,h);

        y+=20,h=30;
        if (NULL != (filename = new TEdit(this,IDE_FILENAME,"",
                x,y,w+200,h)));
        if (NULL != (ScopeTimeBase = new
        TEdit(this,IDE_SCOPETIMEBASE,"",x,y+space,w,h)));
        if (NULL != (ScopeAver = new TEdit(this,IDE_SCOPEAVER,"",
                x,y+2*space,w,h)));
        if (NULL != (ScopeTrig = new TEdit(this,IDE_SCOPETRIG,"",
                x,y+3*space,w,h)));
        if (NULL != (ScopeDelayTime = new
                TEdit(this,IDE_SCOPEDELAYTIME,"",x,y+4*space,w,h)));
        if (NULL != (ScopeVertScale = new
                TEdit(this,IDE_SCOPEVERTSCALE,"",x,y+5*space,w,h)));
        if (NULL != (ScopeOffset = new TEdit(this,IDE_SCOPEOFFSET,"",
                x,y+6*space,w,h)));
        if (NULL != (ScopeTrigChan = new
                TEdit(this,IDE_SCOPETRIGCHAN,"",x,y+7*space,w,h)));
        if (NULL != (ScopeNumPoints = new
                TEdit(this,IDE_SCOPENUMPOINTS,"",x,y+8*space,w,h)));

        new TButton(this,IDB_SCOPEUPDATE,"Update
                Scope",x,y+9*space,150,40);
```

```
//SR560 text and edit boxes

        new TStatic(this,-1,"SR560 Low-Noise Preamp",690,20,200,20);

        x=690,y=65,w=200,h=20,space=50;
        new TStatic(this,-1,"Gain (1,2,5,10,..,50000):",x,y,w,h);
        new TStatic(this,-1,"Filter mode (0:bypass,1:lowpass(6dB),",x,y+space,w+200,h);
        new TStatic(this,-1,"2:low(12dB),3:hi(6dB),4:hi(12dB),5:band )",
                                                        x,y+20+space,w+200,h);
        new TStatic(this,-1,"High pass
                freq.(0.03,0.1,0.3,..,10000):",x,y+20+2*space,w+200,h);
        new TStatic(this,-1,"Low Pass
                req.(0.03,0.1,0.3,...,1000000):",x,y+20+3*space,w+200,h);

        y+=20,h=30;
        if (NULL != (Sr560Gain = new TEdit(this,IDE_SR560GAIN,"",x,y,w,h)));
        if (NULL != (Sr560FilterMode = new TEdit(this,IDE_SR560FILTERMODE,"",
                x,y+20+space,w,h)));
        if (NULL != (Sr560HiFreqFilter = new
                TEdit(this,IDE_SR560HIFREQFILTER,"",x,y+20+2*space,w,h)));
        if (NULL != (Sr560LoFreqFilter = new
                TEdit(this,IDE_SR560LOFREQFILTER,"",x,y+20+3*space,w,h)));


        new TButton(this,IDB_SR560UPDATE,"Update Sr560",x,y+5*space,150,40);

//Message text box

        new TStatic(this,-1,"Messages:",50,670,200,30);

                if (NULL != (ErrorBox = new
                        TEdit(this,IDE_ERRORBOX,"",50,700,600,30)));


        lec9400a=ibdev(0,4,0,T10s,1,0);


//Input .ini parameters
                ifstream inFile;
                inFile.open("c:\\users\\lowell\\programs\\lecroy94.ini",ios::in);
                if (!inFile)
                        {       ErrorBox->SetCaption("Error opening lecroy94.ini file.");
                         }
                char tempword[40]=" ";
                inFile>>tempword;
```

```
                filename->SetCaption(tempword);
                inFile>>tempword;
                ScopeTimeBase->SetCaption(tempword);
                inFile>>tempword;
                ScopeAver->SetCaption(tempword);
                inFile>>tempword;
                ScopeTrig->SetCaption(tempword);
                inFile>>tempword;
                ScopeDelayTime->SetCaption(tempword);
                inFile>>tempword;
                ScopeVertScale->SetCaption(tempword);
                inFile>>tempword;
                ScopeOffset->SetCaption(tempword);
                inFile>>tempword;
                ScopeTrigChan->SetCaption(tempword);
                inFile>>tempword;
                Sr560Gain->SetCaption(tempword);
                inFile>>tempword;
                Sr560FilterMode->SetCaption(tempword);
                inFile>>tempword;
                Sr560HiFreqFilter->SetCaption(tempword);
                inFile>>tempword;
                Sr560LoFreqFilter->SetCaption(tempword);
                inFile>>tempword;
                ScopeNumPoints->SetCaption(tempword);

                inFile.close();

        MessageBox("Must update instrument parameters before starting!",
                                                "Warning!");

}

 char*
TShutWin::get_info(TEdit* edit)
{       char *str,*str2;
        int size;
        if (edit)
        {  str = new char[size=edit->GetWindowTextLength()+1];
                if (str)
                { edit->GetWindowText(str,size);
                        str2=str;
                }
                delete str;
        }
```

```
        return str2;
}

 void
TShutWin::CmOpen()
{       shutter(IDB_OPEN);
}

 void
TShutWin::CmClose()
{       shutter(IDB_CLOSE);
}

 void
TShutWin::CmTrigger()
{       shutter(IDB_TRIGGER);
}

 void
TShutWin::CmReset()
{       shutter(IDB_RESET);
}

 void
TShutWin::CmSr560Update()
{  // Must use "\n" before and after every command!!!
        sr560("\nLALL\n*RST\nCPLG1\nDYNR0\nINVT0\nSRCE0\nUCAL0\n");

        char temp[20],updateinfo[200];
        strcpy(temp," ");
        strcpy(updateinfo," ");

        strcpy(temp,get_info(Sr560Gain));
        switch (atoi(temp))
        {
         case 1:strcpy(temp,"\nGAIN 0\n");break;
         case 2:strcpy(temp,"\nGAIN 1\n");break;
         case 5:strcpy(temp,"\nGAIN 2\n");break;
         case 10:strcpy(temp,"\nGAIN 3\n");break;
         case 20:strcpy(temp,"\nGAIN 4\n");break;
         case 50:strcpy(temp,"\nGAIN 5\n");break;
         case 100:strcpy(temp,"\nGAIN 6\n");break;
         case 200:strcpy(temp,"\nGAIN 7\n");break;
         case 500:strcpy(temp,"\nGAIN 8\n");break;
         case 1000:strcpy(temp,"\nGAIN 9\n");break;
```

```
 case 2000:strcpy(temp,"\nGAIN 10\n");break;
 case 5000:strcpy(temp,"\nGAIN 11\n");break;
 case 10000:strcpy(temp,"\nGAIN 12\n");break;
 case 20000:strcpy(temp,"\nGAIN 13\n");break;
 case 50000:strcpy(temp,"\nGAIN 14\n");break;
 default:
                ErrorBox->SetCaption("Gain must be 1,2,5,10,...,50000!");
                return;
} //end switch
strcat(updateinfo,temp);

strcpy(temp,get_info(Sr560FilterMode));
strcat(updateinfo,"\nFLTM ");
strcat(updateinfo,temp);
strcat(updateinfo,"\n");

strcpy(temp,get_info(Sr560HiFreqFilter));
double hi=atof(temp);
if(hi==(double)0.03){strcpy(temp,"\nHFRQ 0\n");}
else if (hi==(double)0.1){strcpy(temp,"\nHFRQ 1\n");}
else if (hi==(double)0.3){strcpy(temp,"\nHFRQ 2\n");}
else if (hi==(double)1){strcpy(temp,"\nHFRQ 3\n");}
else if (hi==(double)3){strcpy(temp,"\nHFRQ 4\n");}
else if (hi==(double)10){strcpy(temp,"\nHFRQ 5\n");}
else if (hi==(double)30){strcpy(temp,"\nHFRQ 6\n");}
else if (hi==(double)100){strcpy(temp,"\nHFRQ 7\n");}
else if (hi==(double)300){strcpy(temp,"\nHFRQ 8\n");}
else if (hi==(double)1000){strcpy(temp,"\nHFRQ 9\n");}
else if (hi==(double)3000){strcpy(temp,"\nHFRQ 10\n");}
else if (hi==(double)10000){strcpy(temp,"\nHFRQ 11\n");}
else { ErrorBox->SetCaption("High freq. filter must be: 0.03,0.1,0.3,...,10000");
                return;}
strcat(updateinfo,temp);

strcpy(temp,get_info(Sr560LoFreqFilter));
double lo=atof(temp);
if(lo==(double)0.03){strcpy(temp,"\nLFRQ 0\n");}
else if (lo==(double)0.1){strcpy(temp,"\nLFRQ 1\n");}
else if (lo==(double)0.3){strcpy(temp,"\nLFRQ 2\n");}
else if (lo==(double)1){strcpy(temp,"\nLFRQ 3\n");}
else if (lo==(double)3){strcpy(temp,"\nLFRQ 4\n");}
else if (lo==(double)10){strcpy(temp,"\nLFRQ 5\n");}
else if (lo==(double)30){strcpy(temp,"\nLFRQ 6\n");}
else if (lo==(double)100){strcpy(temp,"\nLFRQ 7\n");}
else if (lo==(double)300){strcpy(temp,"\nLFRQ 8\n");}
```

```
        else if (lo==(double)1000){strcpy(temp,"\nLFRQ 9\n");}
        else if (lo==(double)3000){strcpy(temp,"\nLFRQ 10\n");}
        else if (lo==(double)10000){strcpy(temp,"\nLFRQ 11\n");}
        else if (lo==(double)30000){strcpy(temp,"\nLFRQ 12\n");}
        else if (lo==(double)100000.0){strcpy(temp,"\nLFRQ 13\n");}
        else if (lo==(double)300000.0){strcpy(temp,"\nLFRQ 14\n");}
        else if (lo==(double)1000000.0){strcpy(temp,"\nLFRQ 15\n");}
        else { ErrorBox->SetCaption("Low freq. filter must be: 0.03,0.1,0.3,...,1000000");
                return;}
        strcat(updateinfo,temp);

        sr560(updateinfo);

} //end Sr560Update


 void
TShutWin::CmScopeRun()
{       send("TRIG_MODE NORM\n");
}

 void
TShutWin::CmScopeClear()
{       send("CLEAR_SWEEPS\n");
}

 void
TShutWin::CmScopeStop()
{       send("STOP\n");
}

 void
TShutWin::CmScopeReset()
{       send("*RST\n");
}

 void
TShutWin::CmScopeUpdate()
{  ErrorBox->SetCaption(" ");
//      ibclr(lec9400a);
//      send("*rst;\n");
//      send("*rst;INE 256;*SRE 1;\n");
        send("TRACE_CHANNEL_1 ON;TRACE_CHANNEL_2 OFF;\n");
        send("TRACE_FUNCTION_E ON;\n");
        send("SELECT FUNCTION_E;VERT_POSITION 0;\N");
```

```
                    //removed VERT_POSITION -9 when no longer dual grid
        send("TRIG_COUPLING DC;TRIG_MODE NORM;TRIG_SLOPE NEG;\n");
        send("CHANNEL_1_COUPLING D1M;\n");
//      send("DUAL_GRID ON;\n");
        send("AVERAGE_RESET;\n");

         ErrorBox->SetCaption("here");
        char temp[20]="\0",temp2[20]="\0",updateinfo[400]="\0";
        strcpy(temp," ");
        strcpy(updateinfo," ");


        strcpy(temp,get_info(ScopeTrigChan));
        strcpy(temp2,get_info(ScopeTrig));
        strcat(updateinfo,"TRIG_SOURCE ");
        strcat(updateinfo,temp);
        strcat(updateinfo,";");
        strcat(updateinfo,"TRIG_LEVEL ");
        strcat(updateinfo,temp2);
        strcat(updateinfo,";");

        strcpy(temp,get_info(ScopeTimeBase));
        strcat(updateinfo,"TIME/DIV ");
        strcat(updateinfo,temp);
        strcat(updateinfo,";");

        strcpy(temp,get_info(ScopeAver));
//      strcpy(temp2,get_info(ScopeNumPoints));
        strcat(updateinfo,"REDEFINE, AVERAGE, SUMMED, 25000, ");
//      strcat(updateinfo,temp2);  //MAXPTS
        strcat(updateinfo,"CHANNEL_1, ");
        strcat(updateinfo,temp);   //MAXSWEEPS
        strcat(updateinfo,";");

        strcpy(temp,get_info(ScopeDelayTime));
        strcat(updateinfo,"TRIG_DELAY ");
        strcat(updateinfo,temp);
        strcat(updateinfo,";");

        strcpy(temp,get_info(ScopeVertScale));
        strcat(updateinfo,"CHANNEL_1_VOLT/DIV ");
        strcat(updateinfo,temp);
        strcat(updateinfo,";");

        strcpy(temp,get_info(ScopeOffset));
```

```
        strcat(updateinfo,"CHANNEL_1_OFFSET ");
        strcat(updateinfo,temp);

        strcat(updateinfo,";\n");
        send(updateinfo);

}


 void
TShutWin::CmScopeGetData()
{ //      This block of code is useful for seeing double variables
//                      char text[20];
//                      sprintf(text,"%g",preamble[5]);
//                      if(IDCANCEL==MessageBox(text,"like it?",1))
//                              return;

//      char text[30];     //general text variable

        ErrorBox->SetCaption("BEFORE CRASH? ");

        ibclr(lec9400a);

        CmScopeUpdate();
        CmSr560Update();
        if (IDNO==MessageBox("Do you want to start an acquisition?"," ",4))
                {ibclr(lec9400a);
                 return;
                }


//      Start shutter
        CmTrigger();
////////////////

        if(IDNO==MessageBox("Do you want to retrieve the current data?\nNo will
                                        Abort and end the acquisition.","Accept Data",4))
                { CmReset(); //Stop Shutter
                  //      ibclr(lec9400a);
                        return;
                }
 //     else {
 //                     ibwait(lec9400a,2048);
 //                     }
```

```
char pre[200];

strcpy(pre," ");
        ErrorBox->SetCaption("here 2");
        send("COMM_FORMAT,L,WORD,UNSIGNED_SHORT;\N");
        send("READ FUNCTION_E.DESC;\N");
        ibrd(lec9400a,pre,154);



        char * token=",";
        char *ptr=pre;
        int preamble[25];
        ptr=strtok(pre,token);
        int x=0;
        char *temp;
        while (ptr)
                {       temp=ptr;
                        preamble[x]=atoi(temp);
                        x++;
                        if (x>24) break;
                        strcpy(temp," ");
                        ptr=strtok(NULL,token);
                }
//  Added to correctly retrieve the scope delay time when it is
//              negative.
         double signdelay;
         signdelay = atof(get_info(ScopeDelayTime));
         if(signdelay<0.0)
                {preamble[20]=abs(preamble[20]-255);
                preamble[21]=abs(preamble[21]-255);
                preamble[22]=abs(preamble[22]-255);
                preamble[23]=abs(preamble[23]-256);
                }


// Stop Shutter
        CmReset();
////////////////



//      Pull out the data
```

```
long int buffer = 25000;
 unsigned int stf1,stf2;
 stf1=0;
 stf2=0;
 int unsigned *data = new unsigned  int[buffer];

send("COMM_FORMAT,A,WORD;\N");
send("READ FUNCTION_E.DATA;\N");
//read out the first four (useless) bytes

ibrd(lec9400a,&stf1,1);
ibrd(lec9400a,&stf1,1);
ibrd(lec9400a,&stf1,1);
ibrd(lec9400a,&stf1,1);
stf1=0;

for (int qq=0;qq<buffer;qq++)
        {ibrd(lec9400a,&stf1,1);
         ibrd(lec9400a,&stf2,1);
         data[qq]=stf1*256+stf2;
//       sprintf(text,"%u",data[qq]);
//       MessageBox(text,"data",1);
         }

ErrorBox->SetCaption("Data retrieved.");

char file1[60];

BOOL goodfile=FALSE;
while (!goodfile)
{       strcpy(file1,get_info(filename));
        if(IDYES==MessageBox(file1,"Save to this file?",4))
        {  savedata(preamble,buffer,data,file1);
                char text[50];
                strcpy(text," ");
                strcat(text,"Data saved to file: ");
                ErrorBox->SetCaption(strcat(text,file1));
                goodfile=TRUE;
        }
        else    if(IDYES==MessageBox("Use a different filename?",
                                        "choosing No will abandon data",4))
        {       char t[60];
                strcpy(t," ");
                TInputDialog *filechangeDlg;
                filechangeDlg=new TInputDialog(this,"Change File",
```

```
                                        "New Filename--give full path:",
                                        t,sizeof(t));
                        if (filechangeDlg->Execute()==IDOK)
                        {  filename->SetCaption(t);
                        }
                }
                else
                        {break;
                        }
        } //end while


 delete [] data;

} //end ScopeGetData


class TWinShutApp : public TApplication
{
        public:
                TWinShutApp():TApplication()
                {       nCmdShow=SW_SHOWMAXIMIZED;
                }

                void InitMainWindow();

};

BOOL TShutWin::CanClose()
{ int result=MessageBox("Update .ini file?","Close lecroy94",3);
 if(result==IDCANCEL)
                {return FALSE;}
        else if(result==IDYES)
        {  ibonl(lec9400a,0);

                ofstream outFile;
                outFile.open("c:\\users\\lowell\\programs\\lecroy94.ini",ios::out);
                if (!outFile)
                        {       ErrorBox->SetCaption("Error opening lecroy94.ini file.");
                         }
                outFile<<get_info(filename)<<"\n";
                outFile<<get_info(ScopeTimeBase)<<"\n";
                outFile<<get_info(ScopeAver)<<"\n";
                outFile<<get_info(ScopeTrig)<<"\n";
                outFile<<get_info(ScopeDelayTime)<<"\n";
```

```
                outFile<<get_info(ScopeVertScale)<<"\n";
                outFile<<get_info(ScopeOffset)<<"\n";
                outFile<<get_info(ScopeTrigChan)<<"\n";
                outFile<<get_info(Sr560Gain)<<"\n";
                outFile<<get_info(Sr560FilterMode)<<"\n";
                outFile<<get_info(Sr560HiFreqFilter)<<"\n";
                outFile<<get_info(Sr560LoFreqFilter)<<"\n";
                outFile<<get_info(ScopeNumPoints)<<"\n";
                outFile.close();
        }
        else
        {       ibonl(lec9400a,0);

        }
        return TRUE;
}

void
TWinShutApp::InitMainWindow()
{
 // Set the main window and its menu
 SetMainWindow(new TFrameWindow(0,"LeCroy94",new TShutWin));
 GetMainWindow()->AssignMenu("start");

};

int
OwlMain(int/*argc */,char*/*argv*/ [])
{
        return TWinShutApp().Run();
};


void
TShutWin::send(char *cmd)
{       ibwrt(lec9400a,cmd,strlen(cmd));
}

int TShutWin::savedata(int *header,long int buff, unsigned int *data, char* file )
{  //I think that this only passes a pointer--not something the size of
        //      the array.

//      double x,y;

//      Put in a MessageBox to ask if want to change the number of data points here?
```

```
long int npoints;
int step;
npoints = atoi(get_info(ScopeNumPoints));
step = 25000/npoints;

TDate today=TDate();
ofstream outFile;
outFile.open(file,ios::out);
if (!outFile)
 {      ErrorBox->SetCaption("Error opening output file.");
              return 1;
 }
outFile<<"Data taken with LeCroy 9400A, and SR560 preamp."<<"\n";
outFile<<file<<"\n"<<"Data taken on: "<<today<<"\n"<<
              "Number of points saved: "<<get_info(ScopeNumPoints)<<"\n";


//      save state of instruments
outFile<<"scopetimebase:  "<<get_info(ScopeTimeBase)<<" s/DIV\n";
outFile<<"# of averages:  "<<get_info(ScopeAver)<<"\n";
outFile<<"trigger level:  "<<get_info(ScopeTrig)<<" V\n";
outFile<<"scope delay:  "<<get_info(ScopeDelayTime)<<" % fullscale if >0,
                              seconds if <0\n";
outFile<<"scopevertscale:  "<<get_info(ScopeVertScale)<<" V/DIV\n";
outFile<<"scopeoffset:  "<<get_info(ScopeOffset)<<" V\n";
outFile<<"trigchannel:  "<<get_info(ScopeTrigChan)<<"\n";
outFile<<"preampgain:  "<<get_info(Sr560Gain)<<"\n";
outFile<<"preampfilter mode:  "<<get_info(Sr560FilterMode)<<"\n";
outFile<<"High pass freq:  "<<get_info(Sr560HiFreqFilter)<<" Hz\n";
outFile<<"low pass freq:  "<<get_info(Sr560LoFreqFilter)<<" Hz\n";

double gain;
 switch (header[2])
{
 case 22:gain=.005;break;
 case 23:gain=.010;break;
 case 24:gain=.020;break;
 case 25:gain=.050;break;
 case 26:gain=.1;break;
 case 27:gain=.2;break;
 case 28:gain=.5;break;
 case 29:gain=1.;break;
 case 30:gain=2.;break;
 case 31:gain=5.;break;
```

```
        default:
                        ErrorBox->SetCaption("switching error gain");
//                      return;
        } //end switch

        //   so convert data by:  if in WORD format (2-byte, unsigned int):
        //        offset = 256.0*preamble[6] + preamble[7]
        //        gain = gain from above
        //        vgain = preamble[3]
        //        V(t) = (gain*200/(vgain+80))*((data-32768)/8192 - (offset-200)/25)

        double offsetall = (256.0*header[6] + header[7]-200.0)/25.0;
        double prefix= (gain*200.0/((float)(header[3] +80.0)));

        //        Figure out time per point:

//      char text[30];

        float tpoint=0.0;
        switch (header[12])
        {
                case 16:tpoint=0.00000001;break;
                case 17:tpoint=0.00000002;break;
                case 18:tpoint=0.00000004;break;
                case 19:tpoint=0.00000008;break;
                case 20:tpoint=0.0000002;break;
                case 21:tpoint=0.0000004;break;
                case 22:tpoint=0.0000008;break;
                case 23:tpoint=0.000002;break;
                case 24:tpoint=0.000004;break;
                case 25:tpoint=0.000008;break;
                case 26:tpoint=0.00002;break;
                case 27:tpoint=0.00004;break;
                case 28:tpoint=0.00008;break;
                case 29:tpoint=0.0002;break;
                case 30:tpoint=0.0004;break;
                case 31:tpoint=0.0008;break;
                case 32:tpoint=0.002;break;
                case 33:tpoint=0.004;break;
                case 34:tpoint=0.008;break;
                case 35:tpoint=0.02;break;
                case 36:tpoint=0.04;break;
         default:
                        ErrorBox->SetCaption("switching error tpoint");
//                      return;
```

```
        } //end switch

        tpoint = tpoint*step;

        float tbase=0.0;
        switch (header[11])
        {
                case 8:tbase=0.00000005;break;
                case 9:tbase=0.0000001;break;
                case 10:tbase=0.0000002;break;
                case 11:tbase=0.0000005;break;
                case 12:tbase=0.000001;break;
                case 13:tbase=0.000002;break;
                case 14:tbase=0.000005;break;
                case 15:tbase=0.00001;break;
                case 16:tbase=0.00002;break;
                case 17:tbase=0.00005;break;
                case 18:tbase=0.0001;break;
                case 19:tbase=0.0002;break;
                case 20:tbase=0.0005;break;
                case 21:tbase=0.001;break;
                case 22:tbase=0.002;break;
                case 23:tbase=0.005;break;
                case 24:tbase=0.01;break;
                case 25:tbase=0.02;break;
                case 26:tbase=0.05;break;
                case 27:tbase=0.1;break;
                case 28:tbase=0.2;break;
                case 29:tbase=0.5;break;
                case 30:tbase=1.;break;
                case 31:tbase=2.;break;
                case 32:tbase=5.;break;
                case 33:tbase=10.;break;
                case 34:tbase=20.;break;
                case 35:tbase=50.;break;
                case 36:tbase=100.;break;
         default:
                        ErrorBox->SetCaption("switching error tbase");
//                      return;
        } //end switch


        // calculate the delay, first combine the 4 bytes, then convert to time
  double signdelay;
        signdelay = atof(get_info(ScopeDelayTime));
```

```
int sign=1;
if(signdelay<0.0)
        {sign=-1;}
float delay;
delay = 1.*header[23] +256.*header[22] + 65536.*header[21] +
                        16777216.*header[20];
delay = sign*delay*0.02*tbase;

//              So, to calc the x values, x=(x*tpoint) -delay

outFile<<"To convert data to volts:\n  y(V) = prefix*{ (data[i]-32768)/8192 -
                offsetall}\n";
outFile<<"To convert x=0,1,2,3... to time scale:\n  x(t) = (x*tpoint)-delay\n";

outFile<<"(1st data value): y scale offset (offsetall):\n";
outFile<<"(2nd data value): y scale multiplier (prefix):\n";
outFile<<"(3rd data value): time per point (tpoint):\n";
outFile<<"(4th data value): trigger time delay (delay):\n";
outFile<<"(5th data value): number of points (npoints):\n";

outFile<<offsetall<<"\n"<<prefix<<"\n"<<tpoint<<"\n"<<delay<<"\n"<<npoints<
        <"\n";

for ( int i=0;i<(buff-1);i=i+step)
{ //x=(i*tpoint)-delay;
 //     y= prefix*( ((double)data[i]-32768.)/8192. - offsetall);
 //     outFile<<x<<","<<y<<"\n";
        outFile<<data[i]<<"\n";

}
outFile.close();
return 0;
}
```